7-31-2014

# In Vivo 2-Photon Microscopy and Collagen-Hydroxyapatite Scaffolds for Bone Tissue Engineering

Max M. Villa
*University of Connecticut - Storrs*, max.villa.m@gmail.com

# *In Vivo* 2-Photon Microscopy and Collagen-Hydroxyapatite Scaffolds for Bone Tissue Engineering

Max M. Villa, Ph.D.

University of Connecticut 2014

## Abstract

Cell-based bone tissue engineering has shown encouraging results in animal models and even a few human patients. This method could supplement or replace autologous (patient-derived) bone as a bone grafting material, with less damage to existing bone. However the factors that lead to the successful healing of bone injuries by cell-based tissue engineering are poorly understood and the optimal biomaterial for this task has not yet been identified. This dissertation will present: (i) the development of a live animal imaging model to visualize the healing process in a tissue engineered implant for bone regeneration and the novel observations found therein, (ii) the development of a sterile collagen-hydroxyapatite scaffold for consistent bone formation *in vivo*, (iii) the comparison of different methods of cell delivery to collagen-HA scaffolds in the context of bone formation *in vivo*, and (iv) the development of a novel porogen method to enhance the permeability of collagen-HA scaffolds and the usefulness of permeability as a scaffold design metric indicative of success or failure *in vivo*. These results have deepened our understanding of cell-based bone tissue engineering, biomaterial fabrication, and biomaterial design, and should improve the efficacy and consistency of cell-based bone tissue engineering.

# *In Vivo* 2-Photon Microscopy and Collagen-Hydroxyapatite Scaffolds for Bone Tissue Engineering

Max Villa

B.S., Mechanical Engineering, University of Connecticut, 2007

M.S., Mechanical Engineering, University of Connecticut, 2009

A Dissertation

Submitted in Partial Fulfillment of the

Requirements for the Degree of

Doctor of Philosophy

at the

University of Connecticut

2014

APPROVAL PAGE

Doctor of Philosophy Dissertation

***In Vivo* 2-Photon Microscopy and Collagen-Hydroxyapatite Scaffolds for Bone Tissue Engineering**

Presented by:

Max M. Villa, B.S., M.S.

Major Advisor_____

Mei Wei, Ph.D.

Associate Advisor_____

David W. Rowe, M.D.

Associate Advisor_____

Yusuf Khan, Ph.D.

**University of Connecticut**

**2014**

**Acknowledgements**

This dissertation would never have been possible without the great contributions and support of so many people. First and foremost, I would like to express my deepest gratitude to my advisor Dr. Mei Wei for her tireless commitment to my doctoral study. Her patience, support, and generosity have made this endeavor very rewarding.

I would also like to thank the members of my advisory committee for contributing their time, careful review, and helpful suggestions throughout the general exam, dissertation proposal, and dissertation defense: Co-advisor Dr. David Rowe, Dr. Yusuf Khan, Dr. George Rossetti, Dr. Puxian Gao, and Dr. Harris Marcus.

I would like to thank all the members of the Wei Laboratory, past and present, Dr. Xiaohua Yu, Dr. Zengmin Xia, Dr. Fei Peng, Dr. Erica Kramer, Michael Zilm, Drew Clearfield, Stephanie Bendtsen, Changmin Hu, and the numerous others for making my time in the lab such an enjoyable experience. I wish to thank the members of the Institute of Materials Science scientific and technical staff Matthew Beebe, Bob Bouchard, Dr. Jack Gromek, Gary Lavigne, Dr. Laura Pinatti, Dr. Roger Ristau, Dr. Lichun Zhang, and Rick George for their technical expertise and help with the fabrication of experimental equipment.

I owe a great deal to our collaborators at the Uconn Health Center, Dr. David Rowe for his tremendous contribution to the research effort, including animals, instrumentation, and interpretation of biological data. I must thank the members of the Rowe Laboratory for their help performing and troubleshooting technical experiments, Dr. Xi Jiang, Dr. Liping Wang, Mrs. Jianping Huang, Mrs. Li Chen and Dr. Mark Kronenberg. I am also indebted to Dr. Nat Dyment, Dr. Brya Matthews, Dr. Peter Maye, Dr. Sara Strecker, Dr. Ivo Kalajzic, Dr. Yusuke Hagiwara, Dr. I-Ping Chen, Dr. Kamal Khanna, Dr. Yusuf Khan, Dr. Alex Benechet, Dr. Bill Mohler, Dr. Sean Hong, Dr. Douglas Adams, Dr. Xiaonan Xin, Dr. Alex Lichtler, Dr. Radmilla Filipovic, Dr. Brady Maher, Dr. Sina Shahbazmohamadi, Alex Cocco, Kevin Zhou, Dr. Michael Levene, Dr. Timothy Ragan, Peter Kamelin, Dr. Ignacio Arganda-Carreras and the many other researchers and staff for their very helpful technical discussions and/or willingness to lend an instrument. Dr. Peter Maye also kindly provided research animals for the studies presented in Chapter 2 and 3. Zana Kalajzic, Teresa Samuels, and Fan Zhang generously provided tissue for collagen extraction, enabling all scaffold experiments. Vincent Adams and Dr. Chanel Tissot kindly performed irradiation of scaffolds at the University of Maryland Radiation Facility. I would also like to thank Betty Howard of Steris and Christine Thomas of Anprolene for their help with scaffold sterilization.

Without the research support provided by the Department of Education Graduate Assistantships in Areas of National Need and National Institutes of Health, this work would not be possible.

Last, but certainly not least, I would like to thank my loving wife, parents, sisters, brothers, and the many friends and colleagues who have provided their unconditional support and good humor throughout the degree process.

# Table of Contents

# 1 Introduction

## 1.1 The Structure of Bone

Bone is an extraordinary biological composite composed of stiff ceramic and flexible protein filled with vasculature, nerves, and a variety of specialized cells. Hydroxyapatite nanocrystals are organized hierarchically within collagen fibers and other proteins, which provide bone with excellent mechanical properties compared with its constituents alone. On the macroscale, dense cortical bone forms the diaphysis while more porous cancellous bone is present at the distal and proximal ends (Figure 1-1). The trabecular architecture of cancellous bone is aligned with lines of compression and tension, noted as early as 1870 by Wolff, to further enhance to the mechanical integrity of bone.[1] Human cortical bone contains longitudinal cylinders of layered mineralized collagen arrays known as osteons, each with a central void known as a haversian canal, which contains nerves and blood vessels (Figure1-2). The dense cortical bone also contains cells (osteocytes) embedded in void spaces called lacunae, which are interconnected by smaller canals know as canaliculi. Osteocytes are thought to act as a sensor network in cortical bone, regulating bone remodeling through mechanotransduction.[2] The collagen fiber arrays that form the osteon are aligned at different angles from layer to layer. This is thought to introduce isotropy which improves the compressive strength along many directions.[3] Macromolecular collagen fibers contain arrays of individual triple helical collagen molecules (fibrils) joined by hydroxyapatite nanocrystals at their terminal ends. The

mineralized collagen fiber is one of the most abundant biomineralization templates found in nature (teeth, bone, and antlers) and is highly conserved throughout the animal kingdom.

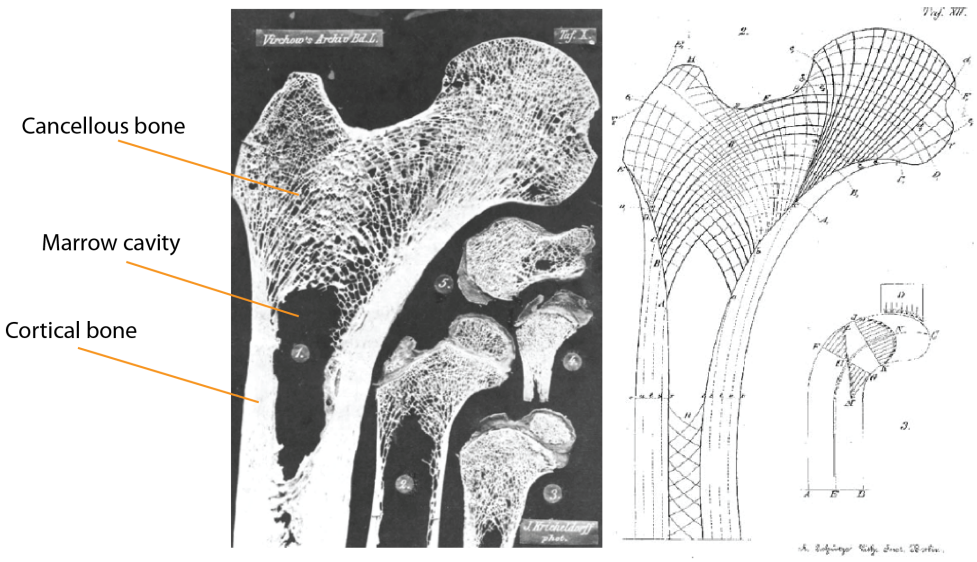


**Figure 1-1 | Cortical and cancellous bone architecture as seen by Wolff.** Line drawing at right indicates trabecular alignment with directions of compressive and tensile forces. Photographs from [**1**].

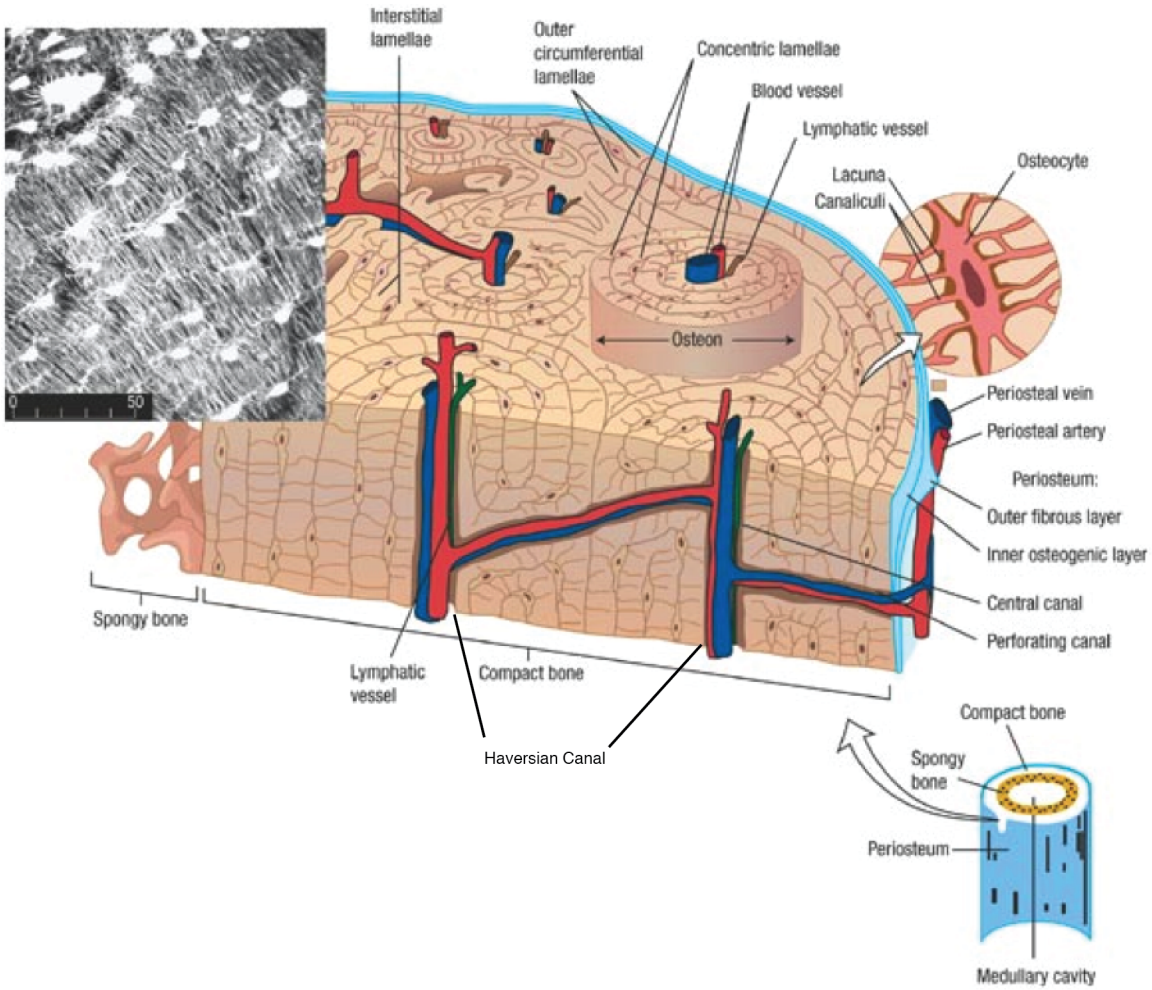


**Figure 1-2 | The osteon, haversian sytem, and osteocyte network of cortical bone.** Inset at top right shows the osteocyte network of lacunae and canalculi within cortical bone. Cylidrical template of the osteon is shown with haversian canals filled with blood and lymphatic vessels. Bottom right highlights the periosteal layer of cells that surrounds the exterior of the bone. From Taylor *et al*.[4]

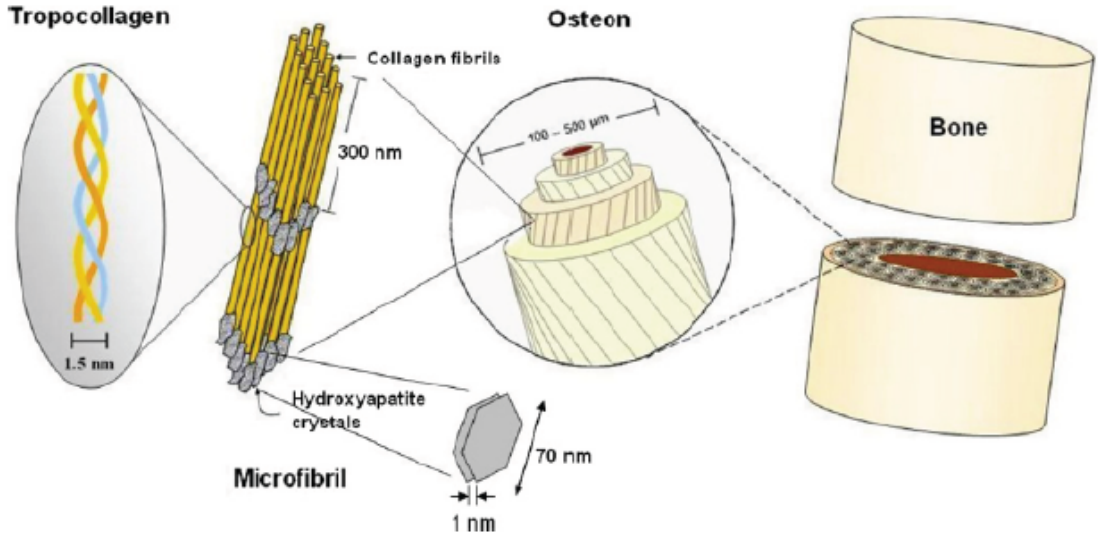


**Figure 1-3 | The hierarchal structure of mineralized collagen fibers in bone.** From left to right: the collagen triple helix, mineralized collagen fibrils, layered plywood-like structure with alternating direction of the osteon, and cross section of the cortical bone showing osteons. From Meyers et al.[5]

## 1.2 The Composition of Bone

The bone matrix is primarily composed of hydroxyapatite (~69% by weight) substituted with ions such as carbonate, fluoride, magnesium, and other trace elements depending on diet.[6,7] Type I collagen forms ~90% of the organic fraction of bone, with the remaining ~10% being proteins such as osteonectin, fibronectin, and osteopontin, among many others.[6] Bone also contains ~10% water by weight, primarily associated with collagen in the bone where it helps maintain its structure.

### 1.2.1 Hydroxyapatite - $Ca_5(PO_4)_3(OH)$

The crystal structure of hydroxyapatite (HA) is shown in Figure 1-4. HA crystallizes as either a monoclinic or hexagonal unit cell, with the hexagonal form being much more common.[8–11] The dimensions of the hexagonal unit cell are a = 9.43 Å and c = 6.88 Å. The crystal structure contains two distinguishing features. First, the hydroxyl groups are

stacked along the c-axis, forming columns of ions spanning the crystal. Oxygen, phosphorus, and calcium ions surround the hydroxyl groups to form a column along the c-axis (Figure 1-4B, grey circle). Secondly the four oxygen atoms adjacent to the phosphorus atoms form tetrahedrons (Figure 1-4A). The closest bond length (0.9 Å) is found in the hydroxyl groups on the c-axis. Shorter bonds are generally stronger as a result of more participating electrons. The hydroxyl group oxygen is bonded at distance of about 3 Å. The long bond length between the hydroxyl group and surrounding atoms is easily distinguished (Figure 1-4B, grey circle) by the amount of open space in the structure. As a result, the hydroxyl groups are more weakly bound to the structure.

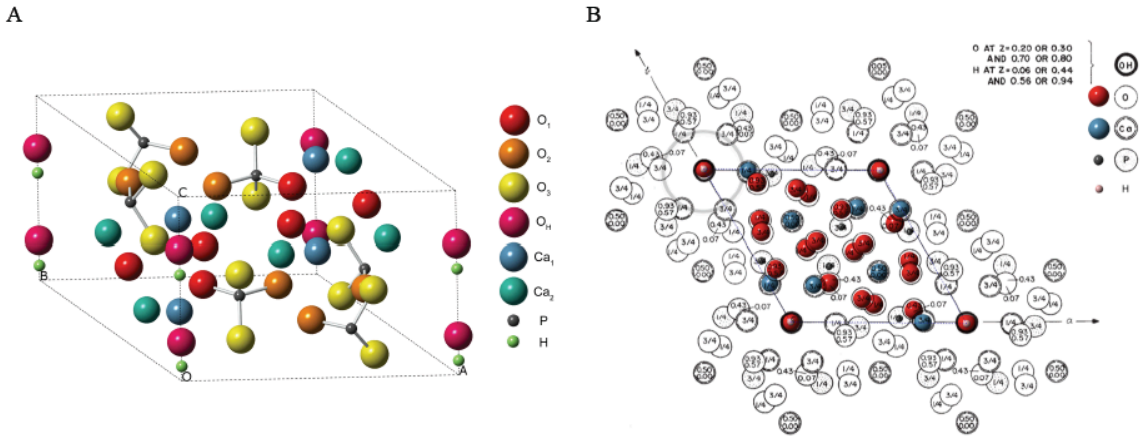


**Figure 1-4 | Crystal structure of hydroxyapatite.** (A) 3D structure of HA showing phosphate tetrahedrons and hydroxyl groups aligned along the c-axis projected in 2D along the c-axis. (B) Black and white drawing from Kay *et al*. superimposed by a 3D rendering in the same orientation to show the agreement with description by symmetry and atom positions. Columns (grey circle) of hydroxyl groups surrounded by oxygen and phosphate atoms are oriented in the c-direction.

### 1.2.2 Collagen

Collagens, of which there are twenty-eight types and many other proteins with collagen-like domains, are the most abundant protein found in the animal kingdom.[12] Type I

collagen, present in bone, tendon, and other connective tissues is the most abundant collagen protein. The primary structure of collagen consists of the amino acid triplet XaaYaaGly, where Glycine is repeated every third residue, and Xaa and Yaa can be any amino acid. Most frequently the Xaa and Yaa positions are occupied by Proline and Hydroxyproline, respectively (Figure 1-5A). The secondary structure of type I collagen is the α-helix, composed of repeating tripeptide units. The C- and N- terminus of the tripeptide chains contain telopeptide elements, which have a net negative and positive charge, respectively.[13] The COL1A1 and COL1A2 genes produces pro-collagen α-helix molecules that, following post-translational modification of the telopeptide ends, form the triple helical collagen monomer (tropocollagen) consisting of one $\alpha_2$ chain and two $\alpha_1$ chains (Figure 1-5B).[14] The triple helix is bound together by a single interstrand hydrogen bond between each amino acid triplet (Figure 1-6). Mutations in COL1A1 or COL1A2 that disrupt the triple helical structure can result in disease states such as Osteogenesis Imperfecta and Ehlers-Danlos syndrome, among others.[12]

Tropocollagen monomers can self-assemble into large, organized fibers with a so-called D-periodicity of 67 nm. This pattern is caused by the repeating gap between subsequent monomers (Figure 1-5C). To link collagen molecules within the fiber, the telopeptide regions of each tropocollagen molecule can be cross-linked via Lys side chains. Cross-linking of this kind is enzymatically formed by lysyl oxidase. Absence of telopeptide regions does not prevent fibril formation, however fibrils lacking these crosslinks are weaker and individuals with mutations interfering with tropocollagen crosslinking has been linked to disease states.[15] The macromolecular structure of collagen fibers,

composed of many collagen molecules, is a right-handed coil of interdigitated microfibers that has been compared to a nanoscale rope.[16,17] Due to the tightly bound superstructure, access to the cleavage site by collagenase is restricted.[17] This view of the collagen superstructure may explain why collagen fiber bundles are less sensitive to degradation by collagenase than collagen monomers. In summary, collagen is organized hierarchically on several length scales and can self-assemble into large superstructures that contribute to the bone matrix.

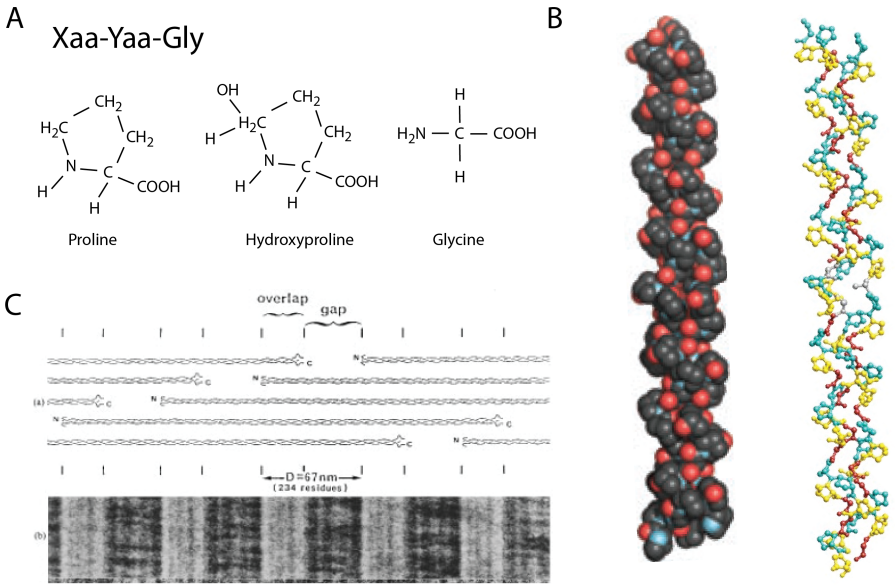


**Figure 1-5 | The collagen triple helix.** (a) Repeating tripeptide amino acid motif, where Xaa and Yaa can be any amino acid, most frequently proline and hydroxyproline, respectively. (b) Three-dimensional rendering of the collagen triple helix found in the protein database entry 1cag, described by Bella *et al*.[18] (c) Schematic of gap region between telopeptide ends of collagen monomers that leads to the characteristic D-banding pattern shown with electron microscopy below, from Kadler *et al.*[14]

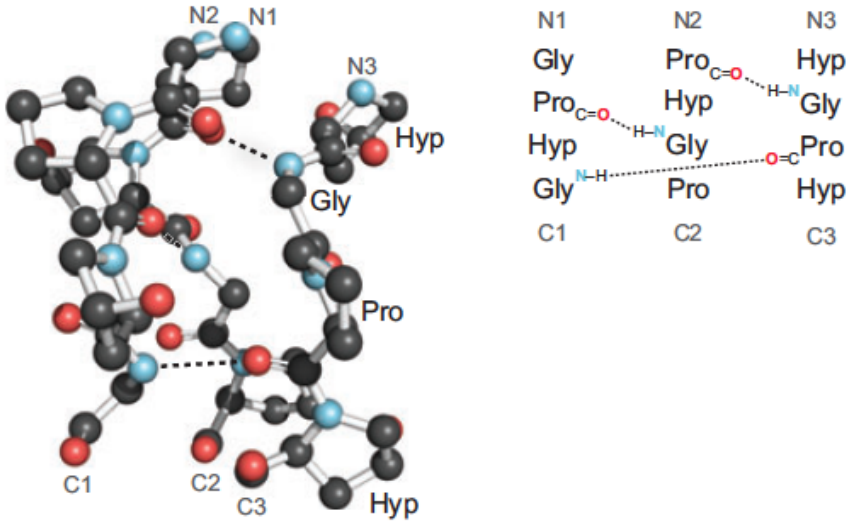


**Figure 1-1-6 | Interstrand hydrogen bonds stabilize the triple helix.** From Shoulders *et al*.[12]

### 1.2.3 Non-collagenous proteins

Non-collagenous proteins (NCPs) found in the bone matrix play multiple roles, including the regulation of collagen fiber mineralization, sequestration and presentation of growth factors, and matrix organization.[6] Many details of NCP function are still being elucidated, and what we know about NCP function to date is derived from gene deletion or overexpression studies, *in vitro* cell and biomineralization assays, and human disease phenotypes linked to mutations in NCP genes. NCPs can be grouped as follows into four general classes of molecules (i) Proteogylcans, (ii) Glycoproteins, (iii) Glycoproteins of the SIBLING family, and (iv) Gla-proteins.

Proteoglycans consist of one or a number of core proteins linked with long glycosaminoglycan (GAG) chains, with the exception of hyaluronan, which lacks a core protein. GAG chains are composed of repeating disaccaride units and are very hydrophilic, enabling the formation of strong hydrogels.[19] In the growth plate of the

developing skeleton, the heparin sulfate proteoglycan perlecan can be found localized in the extracellular space of chondrocytes.[20] Human mutations of the perlecan gene are associated with major skeletal abnormalities.[21] It is thought that perlecan regulates endochondral ossification through cell-matrix interactions. Other proteoglycans, classified as small leucine-rich proteoglycans (SLRPs), such as decorin, biglycan, and fibromodulin, bind to collagen and growth factors, such as TGF-β. In particular, deletion of biglycan leads to reduced trabecular bone, indicating it is a positive regulator of bone formation.[22] Furthermore, decorin has been shown to be a regulator of collagen fibrillogenesis. Mutations in the decorin gene lead to mice with fragile skin and abnormal collagen fibril formation.[23]

Glycoproteins contain oligosaccharide side chains that can be highly modified following translation. The enzyme alkaline phosphatase (AP) is a glycoprotein that is frequently used a histological marker of bone formation, since it is highly expressed during osteogenesis. AP can be found on the cell membrane and within the bone matrix. Mice lacking the gene for AP have a poorly mineralized skeleton with fewer trabaculae.[24] While the function of AP is still being elucidated, one hypothesis is that it regulates mineralization by reducing the pool of inorganic pyrophosphate.[24] Inorganic pyrophosphate has an inhibitory effect on bone formation, and a reduction of this molecule by AP would enable mineralization. Another glycoprotein, Osteonectin, is a so called “matricellular protein” since it is a primarily nonstructural matrix protein, but instead performs roles such as binding calcium, collagen, cells, and growth factors.[25,26]

Osteonectin has also been implicated in regulation of the cell cycle and cell adhesion.[26] Other matricellular proteins found in bone include tenascin, tetranectin, and periostin.[6]

Glyocosylated proteins known as small integrin-binding ligand, N-glycosylated (SIBLING) proteins play important roles in cell attachment and growth factor presentation. These include Osteopontin, Bone Salioprotein, Dentin Matrix Protein, and fibronectin. All of the SIBLING proteins contain the cell attachment motif RGD[27]. In particular, osteopontin and bone salioprotein, which both strongly bind $Ca^{2+}$, can bind osteoblasts to the mineral surface.[6] Furthermore, fibronectin has been shown to amplify growth factor signaling due to the close proximity of integrin and growth factor binding domains within this protein.[28] This synergy has been exploited to develop synthetic matrices containing fibronectin fragments for improved delivery of growth factors.[29]

Gla (γ-carboxylated) proteins contain glutamate domains that are post-translationally modified to form γ-carboxyglutamate. This modification bestows a protein with a formerly weak calcium-binding domain (glutamate), with a new and stronger calcium affinity (γ-carboxyglutamate).[30] The gla-protein Osteocalcin is expressed in osteoblasts and osteocytes[31] and is thought to negatively regulate bone formation[32]. Mice homozygous for the deletion of Osteocalcin initially did not have an apparent phenotype, however older mice (6-month old) had greater cortical bone thickness.[32] Another gla-protein found in the bone matrix is matrix gla protein (MGP), which is expressed in smooth muscle cells and chondrocytes. MGP null mice show mineralization of the arteries and growth plate cartilage, suggesting MGP is an important inhibitor of matrix mineralization.[33]

Notable NCPs involved in the regulation of bone formation, but not produced endogenously, are serum proteins Albumin and α2HS-glycoprotein (also known as Fetuin). Both of these proteins can bind to HA and inhibit crystal growth.[6,34] While found in the bone matrix, the precise role of Fetuin is not clear, however some evidence suggests that inhibition of crystal growth outside of the collagen fibers can make crystal growth inside the fibers more favorable.[35]

In summary, while NCPs are present in relatively smaller amounts than collagen and HA, they nonetheless play very important and often multiple roles in the regulation of mineralization and remodeling. Mutations in just a single NCP can lead to dramatic skeletal abnormalities.

## 1.1 Bone cell biology

The cell biology of bone involves a diverse set of players with functional implications both in and outside of bone[36]. One way of discussing the cells in bone is to divide them into two lineages, (i) the mesenchymal lineage leading to osteoblasts (bone forming cells) and the embedded osteocyte, and (ii) the hematopoietic lineage, which among others, leads to the multinucleated osteoclast (bone removing cell).

### 1.2.4 The mesenchymal lineage leading to the osteocyte

Mesenchymal stem cells represent roughly 0.001% to 0.01% of cells in the bone marrow and can differentiate to form osteoblasts, chondrocytes, adipocytes, and myoblasts.[37]

These cells occupy a perivascular niche in the bone marrow,[38] and have been shown to contribute to the patency of new vessels.[39] In response to the natural turnover of bone-forming osteoblasts, mesencyhmal stem cells can differentiate into osteoprogenitor cells, followed by osteoblasts, and later osteocytes (Figure 1-7). Defining unique markers for MSCs has been difficult to do, although a combination of surface markers such as STRO-1, CD90, CD71, CD29, and CD44 are often used.[37,40] Additionally, Grcevic *et al*.[41] and Liu *et al.*[42] have generated transgenic mice with fluorescent markers using promoter regions from the SMAA and TWIST genes, respectively, to define a population of multipotent progenitors in the bone marrow. Furthermore, marker genes based on portions of the COL1A1 promoter region have been used identify populations of early and mature osteoblast cells.[43]

Several proteins are involved in the regulation of osteoblast differentiation from MSCs, including PTH, TGF-β, BMPs, WNTs and Hedgehogs, however the transcription factor Runx2 (also Cbfa1) is thought to be the master regulator of osteoblast differentiation.[44] RUNX2 −/− mice show a complete lack of bone formation[45] and heterozygous mutations in RUNX2 share similar phenotypes to the rare human syndrome cleidocranial dysplasia[46]. Runx2 can both positively and negatively regulate a number of bone-related genes such as COL1A1, ALP, ON, OSTERIX and OC.[44] A model of the pathways that interact with Runx2 is pictured below (Figure 1-8).

Following differentiation into osteoblasts, part of this population becomes osteocytes embedded in cortical bone. Osteocytes form an interconnected network of long, dendritic

processes inside cavities in the cortical bone known as the lacunocanicular network (Figure 1-10). Osteocytes have long been thought to regulate bone turnover through mechanotransduction, yet this process is poorly understood.[47] Recent work has demonstrated that osteocyte projections are particularly sensitive to fluid shear stress, which in turn activates $Ca^{2+}$ signaling amongst the osteocyte network.[48] Osteocytes have also been shown to regulate osteoblast and osteoclast activation through secretion of soluble factors and direct cell-cell contact.[2]

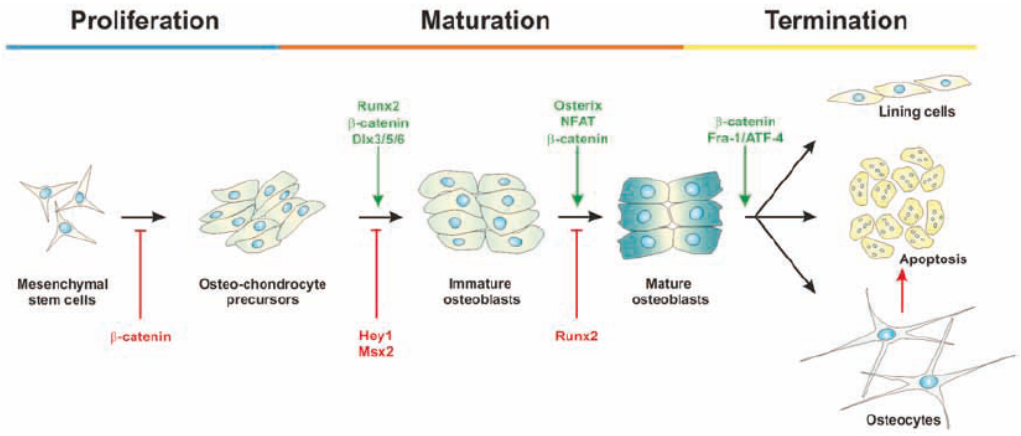


**Figure 1-7 | Differentation of MSCs toward osteoblasts and osteocytes.** From de Gorter and ten Dijke.[44]

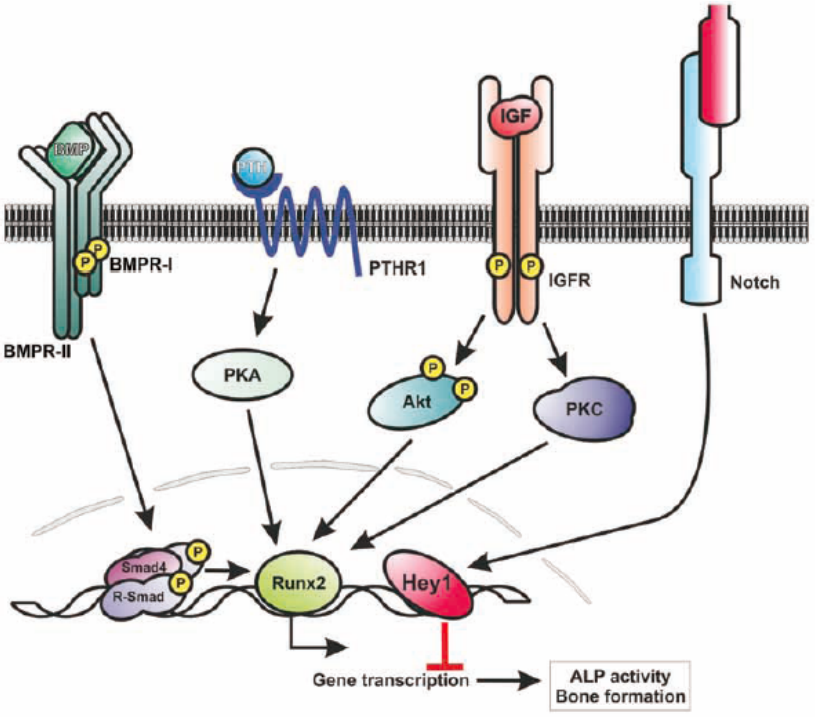


**Figure 1-8 | Pathways converging on Runx2, a master regulator of osteoblast differentiation.** From de Gorter and ten Dijke.[44]

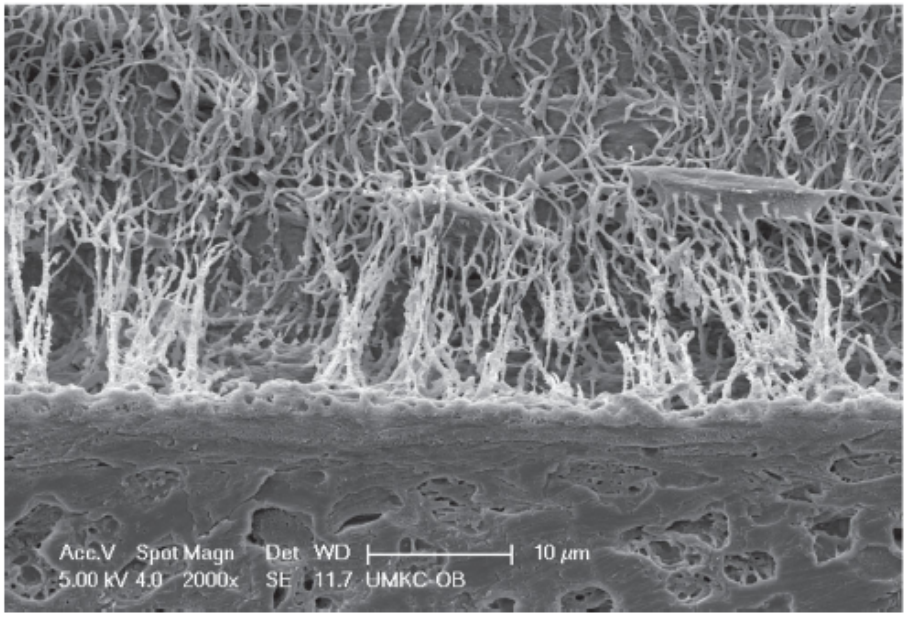


**Figure 1-9 | The lacunocanicular network.** Scanning electron micrograph of resin-embedded lacunocanicular network following acid etching. Image from Bonewald.[49]

### 1.2.5 The hematopoietic lineage leading to the osteoclast

The bone marrow supports the production of red blood cells (~1 billion RBCs/hour)[50], immune cells, and the bone-remodeling cells known as osteoclasts. Immune cells, platelets, RBCs, and osteoclasts are all derived from a single progenitor known as a hematopoietic stem cell (HSC) (Figure 1-10). The lineage progression from HSC to osteoclast, shown below (Figure 1-11), depends on receptor activator of nuclear factor-κB ligand (RANKL) and macrophage colony stimulating factor (M-CSF) to fuse multiple macrophage cells, which differentiate into a large multinucleated osteoclast.

Bone modeling and remodeling is regulated by interconnected signals from osteoblasts, osteocytes, osteoclasts, and even organs outside the bone. This balancing act between bone formation (modeling) and removal (remodeling) is regulated in part through RANKL signaling (Figure 1-12). In a bone-remodeling scenario, osteoblasts and osteocytes secrete RANKL and other factors that activate osteoclastogenesis and osteoclast-mediated bone remodeling. By contrast, considering a modeling scenario, osteoblasts and osteocytes produce osteoprotegerin (OPG), which binds to RANKL, and therefore inhibits RANKL mediated osteoclast activation.

Once activated, osteoclasts form a tight seal around the bone surface, mediated by αvβ3 integrins which bind to RGD motifs on proteins within the bone.[51] The osteoclast then creates an acidic microenvironment (pH ~4.5) by secretion of $H^+$ and $Cl^-$ ions through the combination of a proton pump ($H^+$-ATPase) and chloride ion channels.[52] The acidic microenvironment dissolves the hydroxyapatite mineral and exposes scaffolding proteins

such as type I collagen. Osteoclast secretion of Cathepsin K and matrix metalloproteinases (MMPs) cleave and digest the underlying collagen.

In summary, MSCs produce the bone forming osteoblast and HSCs produce the bone remodeling, multinucleated osteoclast. The delicate balance between bone formation and removal is orchestrated in part through RANKL signaling between osteoblasts, osteocytes, and osteoclasts.

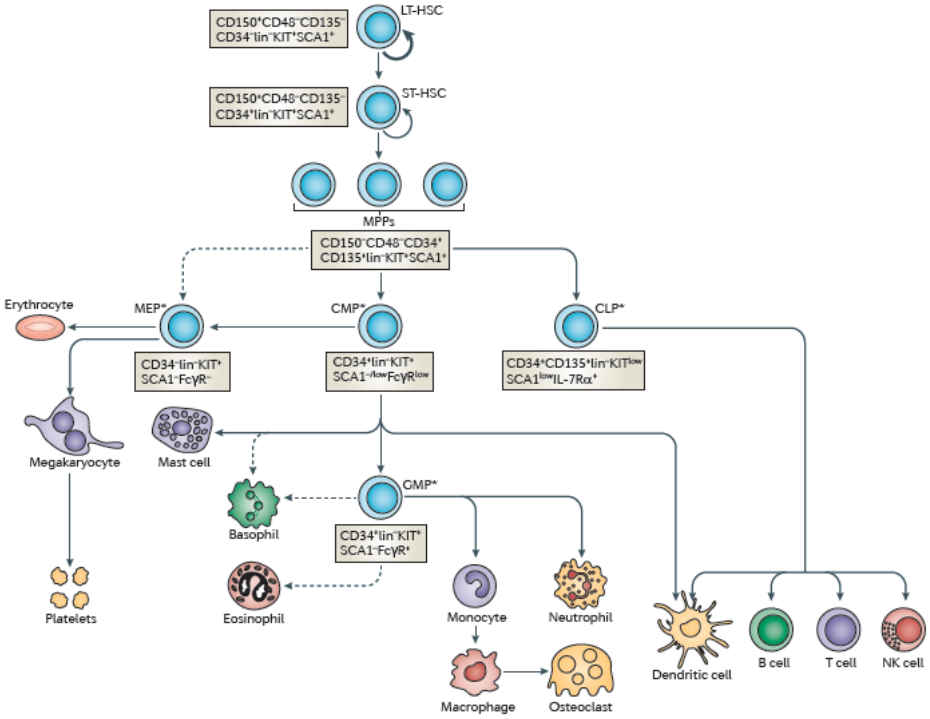


**Figure 1-10 | Hematopoietic lineage tree.** LT-HSC Long term reconstituting hematopoietic stem cell , ST-HSC Short term reconstituting hematopoietic stem cell, MPP – multipotent progenitors, CMP – common myeloid progenitor, MEP - megakaryocyte erythrocyte progenitor, CLP – Common lymphoid progenitor, GMP – Granulocyte monocyte progenitor. From Wang and Wagers.[50]

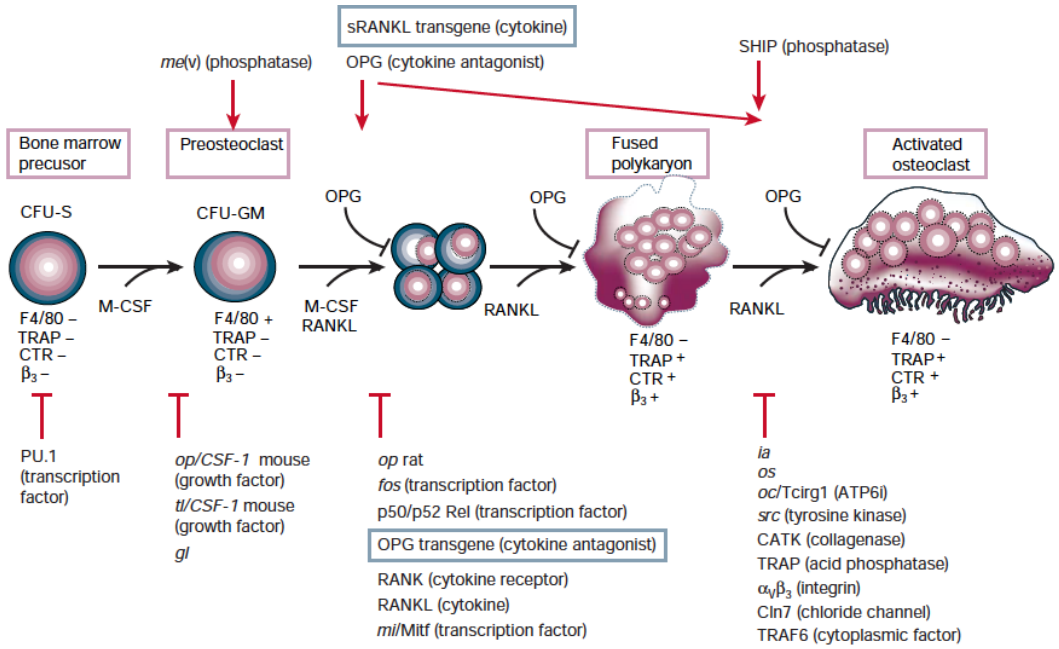


**Figure 1-11 | The formation of osteoclasts starting from hematopoietic stem cells.** From Boyle *et al*.[53]

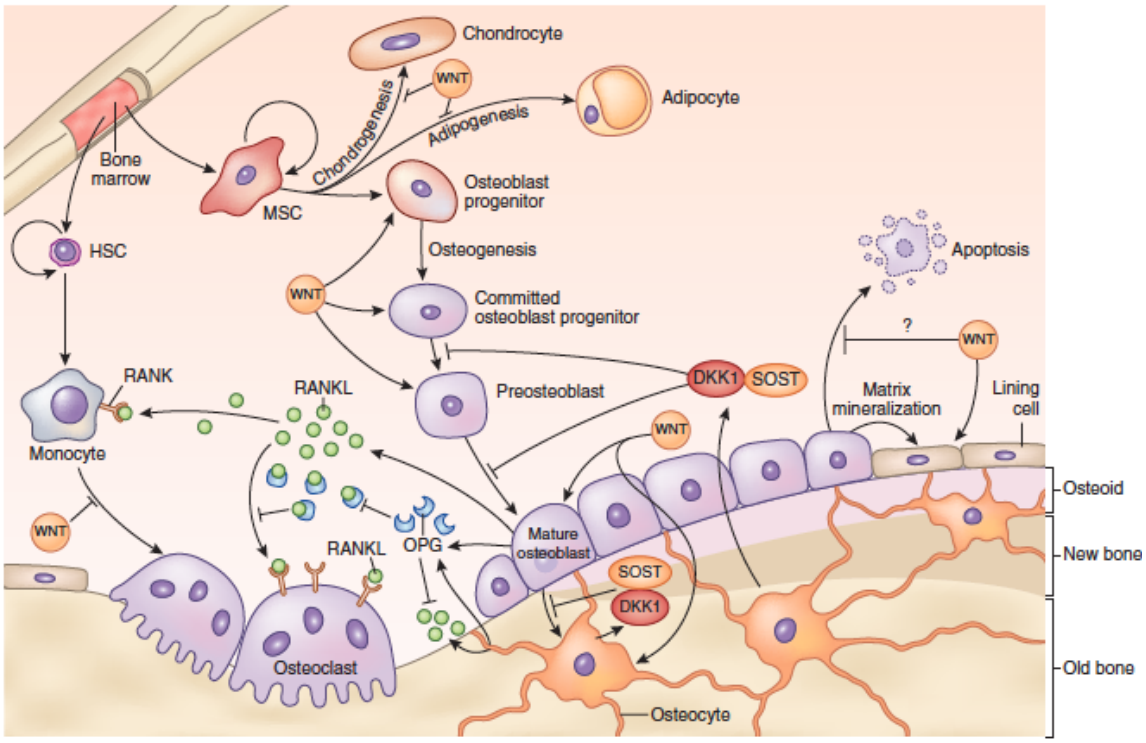


**Figure 1-12 | Interaction of osteoclasts, osteoblasts, and osteocytes controlling bone modeling and remodeling.** From Baron and Kneissel.[54]

## 1.3 Bone healing

Bone is one of the few human tissues endowed with the extraordinary ability to heal completely without the formation of scar tissue. However, roughly 10% of all bone fractures fail to heal due in part to aging, diabetes, or smoking.[55] Bone healing is a tightly orchestrated cascade that involves the expression of thousands of genes as cells migrate to a site of injury and differentiate, ultimately forming new tissue through a series of stages. The overlapping stages of gene expression can be broadly classified, in the order they occur following injury, as inflammatory, chondrogenic, and osteogenic (Figure 1-13). In humans, the stages to completion of healing require several months, whereas the mouse (used as a model herein) will heal significantly faster.

Immediately following bone injury, a hematoma forms (Figure 1-14A) consisting of platelets and red blood cells entangled in a fibrin matrix, which stems from the precursor fibrinogen found in the bloodstream. Macrophages and other immune cells from the bloodstream invade the hematoma and secrete pro-inflammatory cytokines TNF-α, IL-1, IL-6, IL-11, and IL-18 that recruit MSCs from the surrounding tissue and stimulate angiogenesis.[56] MSCs are found in a number of regions near the site of injury such as the marrow, periosteum, and adjacent muscle. Some evidence suggests that progenitors found in the periosteal layer may be the primary contributor to fracture repair.[55] Once activated by inflammatory cytokines, osteoprogenitors rapidly proliferate and migrate towards the site of injury (Figure 1-15). The periosteal layer thickens as cells proliferate and a cartilaginous callus is formed in the hypoxic core of the defect (Figure 1-14C through D). Hypoxia is a well-known inducer of cartilage formation.[57] Cartilage also

forms in areas of mechanical instability, to later undergo endochondral ossification. By contrast, in well-stabilized fractures, bone formation can occur by intramembranous ossification, completely forgoing the cartilage intermediate step.[58] As blood vessels invade a cartilaginous callus, bone formation proceeds by the endochondral mechanism (Figure 1-14E). Mineral formation also occurs on the perimeter of the callus, which bridges the two ends of the fracture. The oversize mineralized callus, consisting of loosely organized woven bone, is remodeled by osteoclasts to return to the anatomical shape and lamellar microstructure of the bone pre-injury (Figure 1-16 and Figure 1-14E).

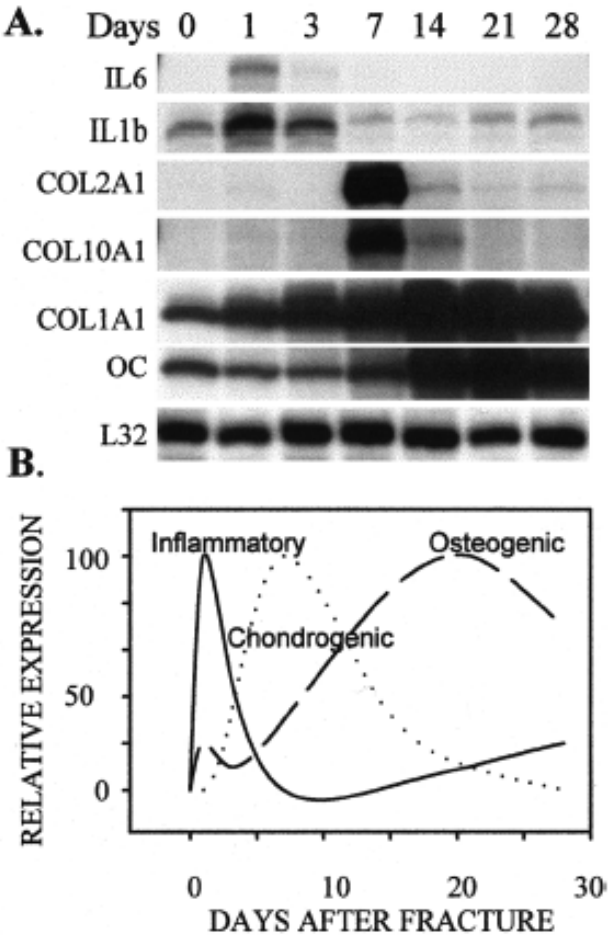


**Figure 1-13 | Expression of selected genes following fracture.** (A) Polyacrylimide gel showing products from a ribonuclease protection assay from fracture samples at different

times following injury. L32 is a housekeeping gene expected to be contast over the time period examined. (B) Schematic representation of the three general categories of gene expression following injury. From Cho *et al*.[59]

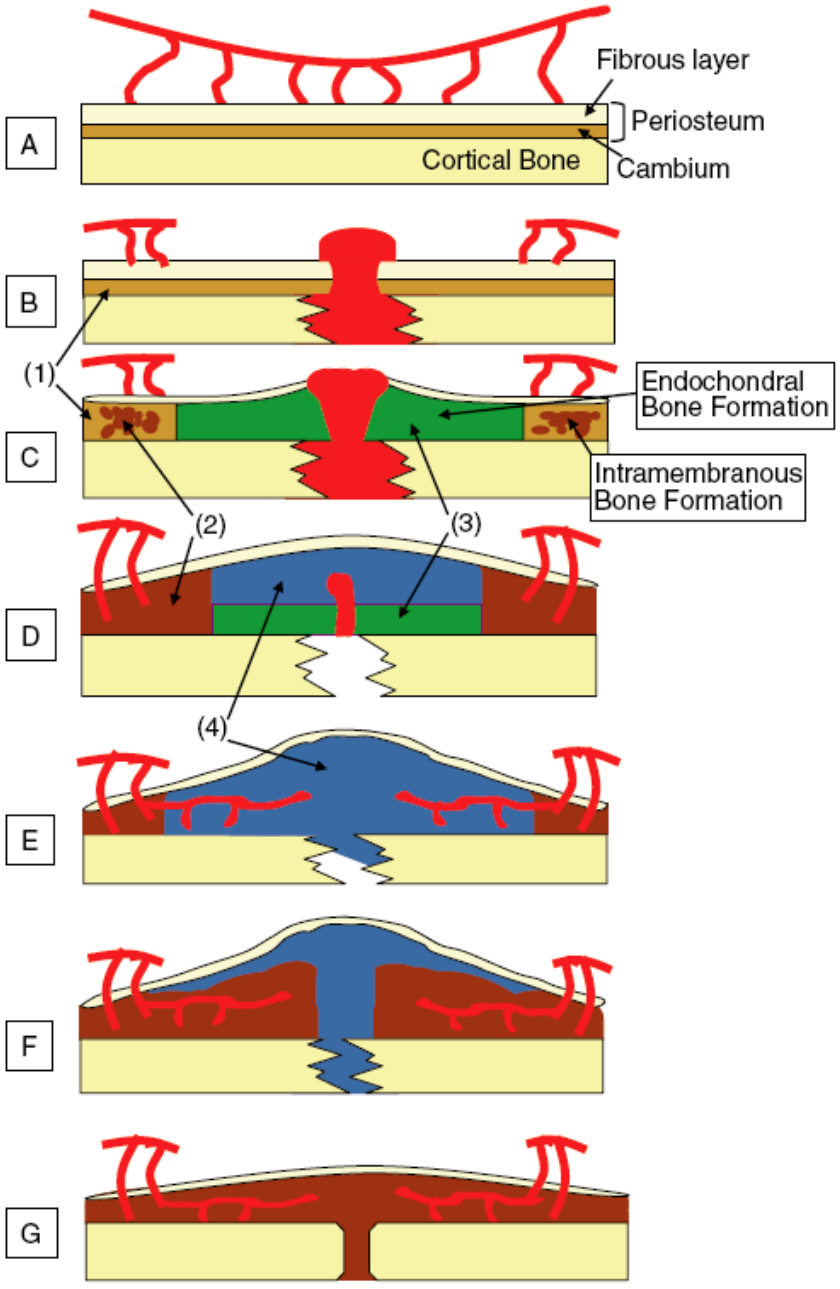


**Figure 1-14 | The progression of fracture repair.** (a) Organization of bone prior to injury. (b) Fracture occurs and hematoma forms at the site of injury. (c) Periosteum thickens and ossifies at the ends, while cartilage forms in the core of the defect. (d) Cartilage maturation. (e-f) Blood vessels invade the cartilage and begin endochondral ossification. (g) Loosely organized woven bone is slowly remodeled into the original anatomic structure pre-injury. Schematic from Zuscik.[55]

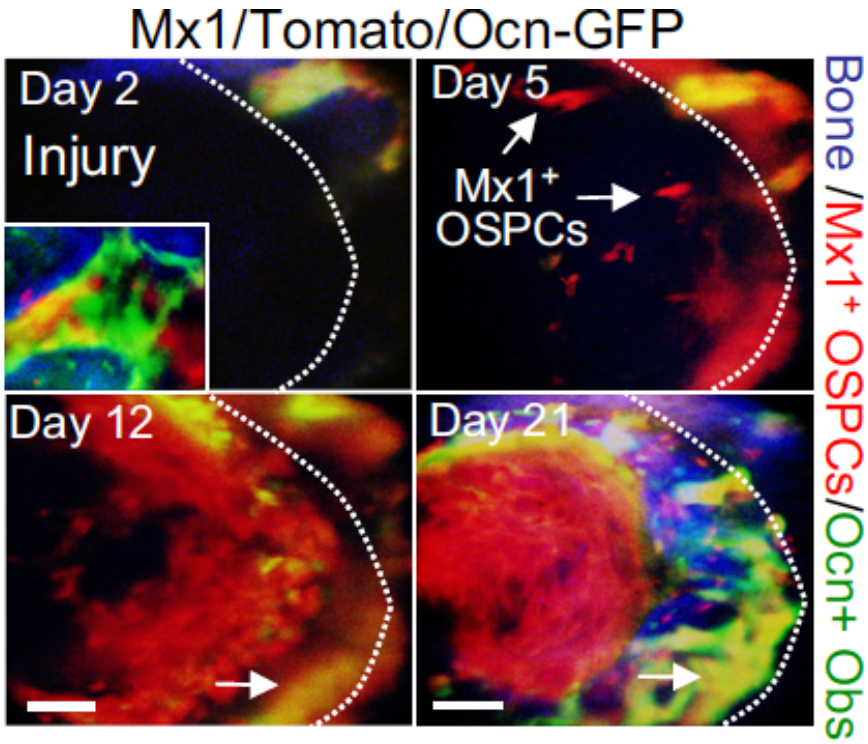


**Figure 1-15 | Invasion of osteoprogenitors following a bone defect.** Shown here is the temporal progression of osteprogenitors (red) invading a circular defect (border shown by dotted line) in a mouse calvarium. Once inside the defect, osteoprogenitors differentiate into osteoblasts (green, double positive appear yellow) and form new bone (blue) in the defect. Some cells can be seen embedded in the new bone matrix (blue) at Day 21. From Park *et al*.[60]

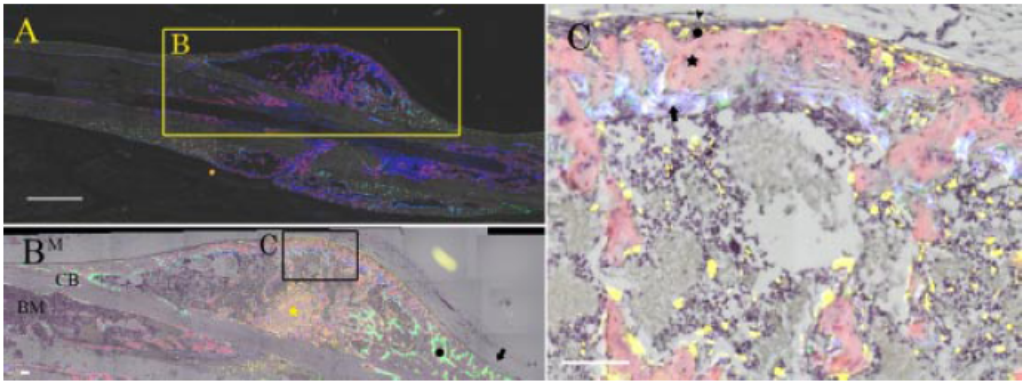


**Figure 1-16 | Remodeling phase of a mouse fracture callus three weeks after injury.** (A) Early and mature osteoblasts are indicated using marker genes Osteocalcin (green) and Col3.6cyan (blue), respectively. Sites of active mineralization are labeled in red. Yellow in (B) and (C) indicate TRAP activity from osteoclasts. From Ushiku *et al*.[61]

## 1.4 Bone Tissue Engineering

### 1.4.1 The promise of bone regeneration, current approaches, and challenges

Large bone defects arise due to trauma, tumor resection, or congenital disorders. The gold standard material for bone grafting is autologous bone, which is simply bone from the patient, and is thus immune-compatible and highly osteogenic. However, in the case of large defects there is simply not enough bone on the patient. Alternatively, bone regeneration can be realized with the use of a scaffold material combined with cells,[62–65] morphogenetic factors[66] or some combination of the two[67]. At present, a scaffold material alone has not induced bone formation *in vivo*, and thus exogenous factors or cells are required.[68]

In 1965, Marshall Urist discovered that demineralized bone, when implanted intramuscularly in rabbits, restarted the developmental process of bone formation.[69] This led him to surmise that demineralized bone contained factors that induced *de novo* bone formation, forming the foundation for the later description of the BMP family of growth factors.[70] At present, only three growth factors are FDA-approved for orthopedic applications. These include recombinant BMP-2 (Infuse, Medtronic), BMP-7 (OP-1, Stryker) and PDGF-BB (Augment, BioMimetic Therapeutics).[71,72] Compared with cells of possibly unknown differentiation state and osteogenic potential, therapeutic factors can be better defined. For instance, the number of mesenchymal stem cells in the bone marrow decreases with age[73] and is also affected by disease state such as diabetes[74]. This feature makes growth factor approaches easier to regulate and gain approval than their cell-based counterparts. Furthermore, BMP-7 delivery in a polycaprolactone scaffold

more consistently healed sheep segmental defects than autologous MSC delivery in the same scaffold (Figure 1-17).[66] However, clinical growth factor doses are far higher than found physiologically, on the order of mg/mL versus ng/mL concentrations.[75] For instance, recombinant OP-1 packaged for use in 3.5 mg vials corresponds to more than twice the amount found in two entire human skeletons.[76] In the case of BMP-2, supraphysiologic concentrations are linked to adverse effects in humans, including but not limited to, ectopic bone formation, osteolysis, and elevated cancer risk.[77] One might ask: why do therapeutic growth factor concentrations need to be so high? One explanation is that the above-mentioned growth factors are delivered without critical cofactors often found in the extracellular matrix. Martino *et al.*[29] recently demonstrated that when a fibronectin fragment was delivered along with PDGF-BB and BMP-2, ng/mL (instead of mg/mL) concentrations were capable of healing rat calvarial critical-size defects. While this approach would need to be examined in larger animal models where higher growth factor concentrations are required, this result shows promise for future growth factor-based bone regeneration and highlights the role of ECM proteins in mediating signaling. However, in their present form, supraphysiological doses of growth factors for bone healing are associated with significant safety concerns.

In stark contrast to the delivery of one or two growth factors, bone healing is a tightly orchestrated cascade involving thousands of genes, which on the order of hundreds are secreted factors.[59,78,79] Cell-based approaches leverage the intrinsic ability of cells to sense and react to these many different signals. Cells are able to respond to microenvironmental cues by releasing factors, migrating, or organizing in well-defined

patterns within strict temporal and spatial scales.[80] This exquisitely controlled behavior decreases the likelihood of off-target effects. Cells can also be genetically modified to provide additional control, such as an apoptosis circuit to prevent aberrant proliferation and tumor formation.

Several cell sources could be implemented in a tissue-engineering strategy, foremost among them are mesenchymal stem cells (MSCs) found in the bone marrow.[81] Some studies have suggested that MSCs are immunopriveleged due to a lack of specific histocompatibility antigens.[82] If indeed safe and equally effective as autologous cells, this would broadly expand the pool of MSCs for therapeutic use. Other cells being investigated for regenerative potential are adipose-derived stem cells, human umbilical vein cells, and periosteal cells.[83] Additionally, satellite cells in the surrounding skeletal muscle can differentiate into osteoblasts.[84] Pluripotent stems cells such as human embryonic stem cells (hESCs) or induced pluripotent stem cells (IPSCs) can also be used to derive osteoblasts. IPS-derived osteoblasts could provide a source of patient-specific cells from a skin biopsy.

Tissue engineering strategies involving a patients own cells have shown promising results in the clinic.[62,85–87] In the only published study of bone tissue engineering in humans, four patients with large diaphyseal defects were treated with porous hydroxyapatite scaffolds and autologous culture-expanded bone marrow cells.[62] All patients recovered limb function, and in 3 of the 4 patients re-examined 6 years following the procedure, the implant was completely fused to the host bone, providing evidence for the long-term

efficacy of a cell-based approach (Figure 1-18). This group proposes "the use of culture-expanded osteoprogenitor cells in conjunction with porous bioceramics as a real and significant improvement in the repair of critical-sized long bone defects." This group notes that controlled clinical trials will ultimately have to be undertaken in order to definitively evaluate the effectiveness of a tissue engineering strategy versus other approaches. Additionally this study found that the ceramic scaffold was still mostly present at 6-7 years post-implantation (Figure 1-18). Cracks in the ceramic scaffold were reported, which could comprise the mechanical integrity of the overlying bone. Therefore it would be advantageous to the patient to use a scaffold with a degradation rate that matches the rate of new bone formation. Furthermore, bone formation was localized to the external surfaces of the ceramic scaffold. This was thought to be due to heterogeneous cell loading or better cell survival at the external surfaces. Thus cell seeding and survival following implantation should be examined and may require improvement.

Due to the difficulty of the defects found in the patients, a control group involving a scaffold without cells was not used. Therefore, this work did not provide evidence of the therapeutic value of the implanted MSCs. By contrast, the contribution of MSCs to bone repair has been demonstrated in numerous animal models (Figure 1-19),[64,65,88,89] however the success rate of this method has been less than 50% in some large animal studies[65,66].

Bone tissue engineering with marrow stromal cells has shown limited clinical success and lagged behind growth factor-based approaches, in part due to technical hurdles such as:

(i) an incomplete understanding of how transplanted cells mediate bone repair *in vivo*, (ii) a poor understanding of cell manipulation prior to implantation and optimal methods thereof, and (iii) current scaffolds are still largely nonphysiological and thus rely on comparatively less potent signaling mechanisms than the *in vivo* milieu. The specific aims presented in Chapter 2 were formulated to directly address these limitations.

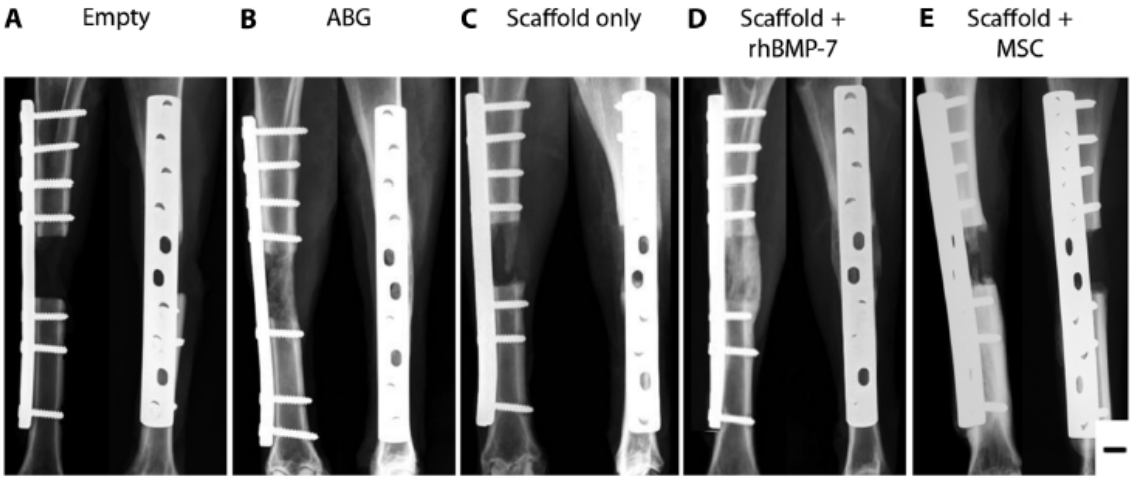


**Figure 1-17 | Comparison of cell-based versus growth factor-based bone tissue engineering in sheep segmental defects.** Radiographs of defects following 3 months of implantation with either (B) autologous bone, (C) a PCL scaffold, (D) a PCL scaffold + BMP-7, (E) a PCL scaffold + autologous MSCs or (A) an empty defect used as a negative control. From Reichert *et al*.[66]

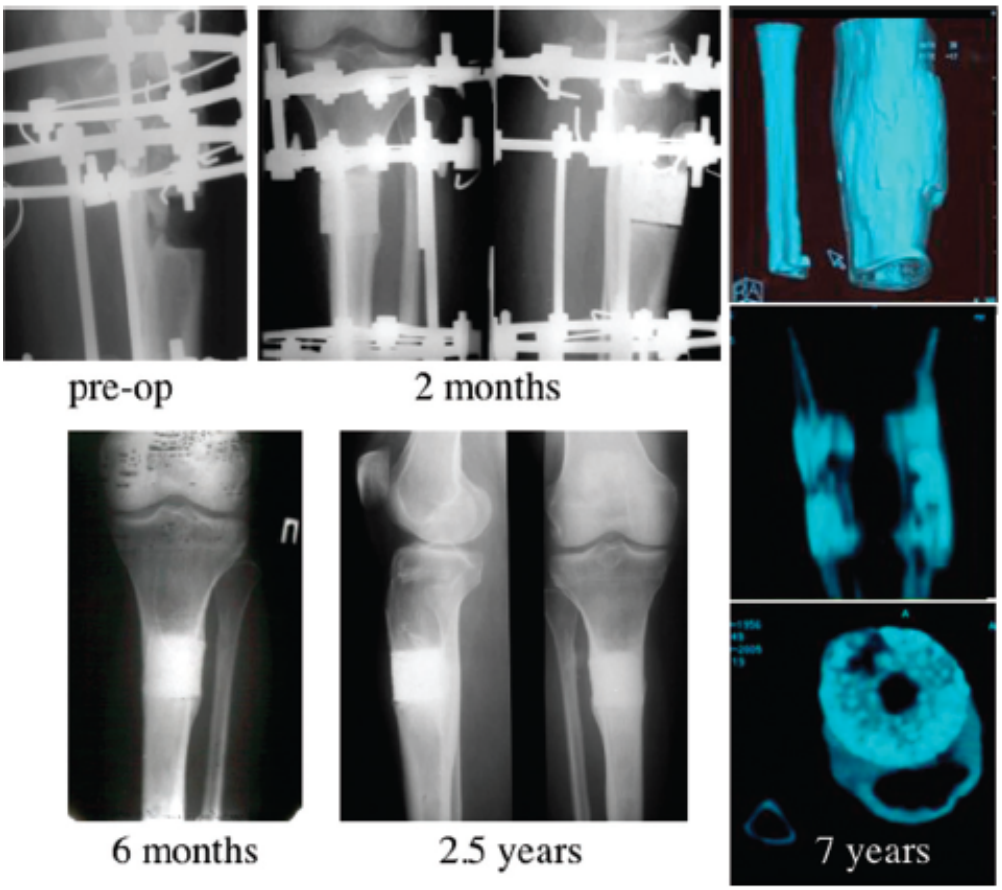


**Figure 1-18 | Bone tissue engineering using culture-expanded MSCs in humans.** X-ray (gray) and CT scan (blue) of bone defect filled with culture-expanded hMSCs before and after surgery. The defect was the result of an unsuccessful bone-lengthening attempt. From Quarto et al.[62]

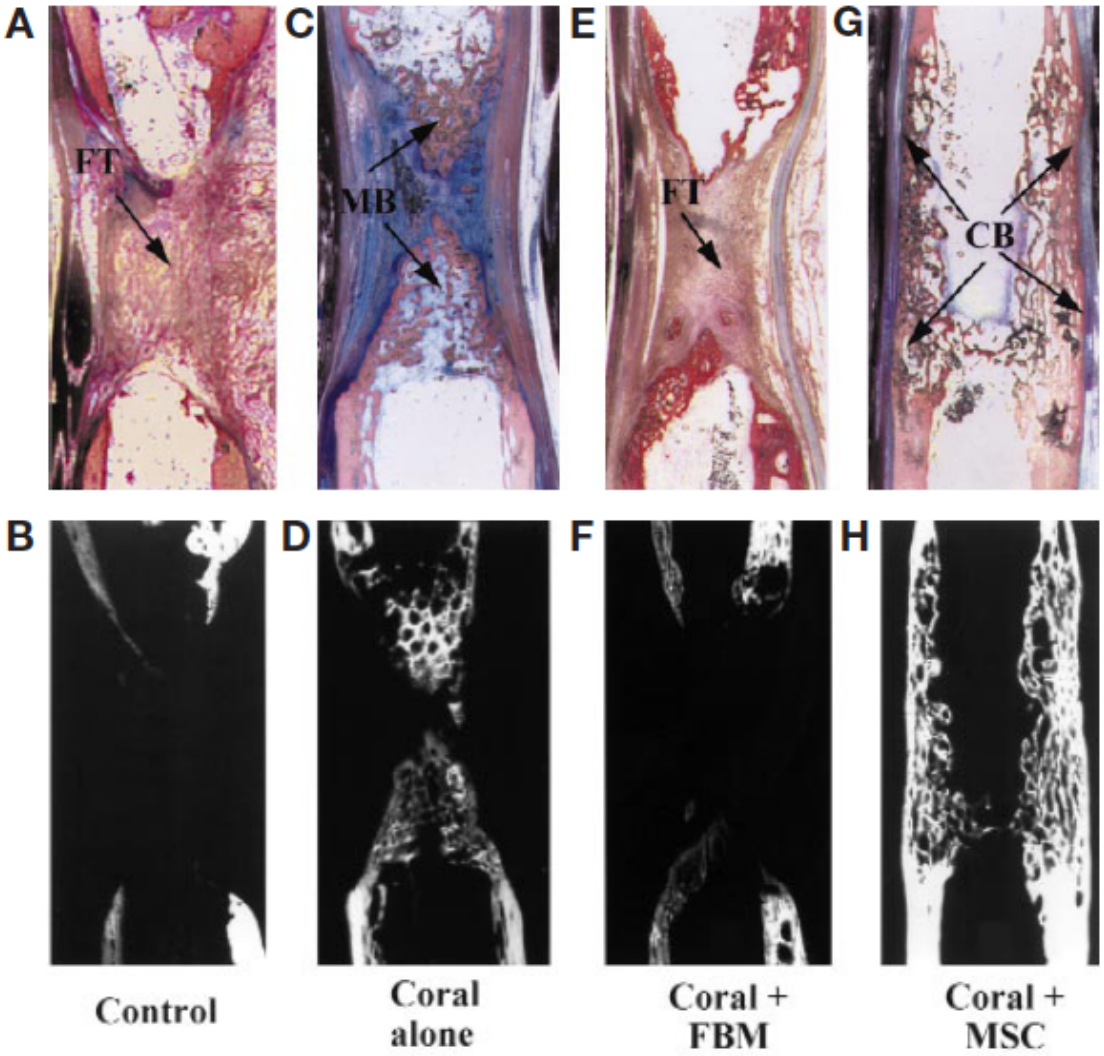


**Figure 1-19 | Healing large defects using culture-expanded MSCs in sheep.** Histology (top row) and radiographs of defect sections (bottom row) 16 weeks after implantation. (A-B) Control-no cells or scaffold. (C-D) Coral scaffold alone. (E-F) Coral scaffold plus fresh bone marrow. (G-H) Coral scaffold plus culture expanded bone marrow MSCs. From Petite et al.[65]

### 1.4.2 Scaffolds for Bone Tissue Engineering

Scaffolds for bone repair include synthetic polymers (poly-L-lactide, polycaprolactone, poly-lactic-co-glycolic acid), proteins (collagen, fibrin, hyalulronic acid), calcium phosphates (β-tricalcium phosphate, hydroxyapatite, substituted hydroxyapatites, natural-

occurring corals) or some combination of these materials.[90] Several graft materials, which designed for use with bone marrow aspirate, are currently available or approaching the market. These are included in the table below.

| Product | Manufacturer | Materials | FDA status |
|---|---|---|---|
| Collagraft | Zimmer | Bovine type I collagen-hydroxyapatite/tricalcium phosphate granules | Approved (PMA) |
| Actifuse | Baxter | Silicon substituted hydroxyapatite – resorbable polymer | Approved (510k) |
| Healos | Depuy | Bovine type I collagen-coated with hydroxyapatite | Approved (510k) |
| Ossimend | Collagen Matrix | Type I collagen – bone mineral | Approved (510k) |
| Mozaik | Integra LifeSciences | Collagen- tricalcium phosphate granules | Approved (510k) |
| InQu | ISTO Technologies | PLGA-hyalulronic acid | Approved (510k) |
| Augment | BioMimetic Therapeutics | Bovine type I collagen-carbonated apatite granules | PMA in process |

**Table 1 | Scaffolds indicated for use with bone marrow aspirate that are on or approaching clinical use.**

Previously, our lab has developed a scaffold composed of type I collagen and hydroxyapatite (Figure 1-20).[89,91,92] This material combination is based on mimicking the collagen and apatite content found in native bone. The collagenous phase is easily mineralized[13] or degraded by MMPs during healing,[93] allowing for fast remodeling. The calcium phosphate phase provides ions[94,95] and a osteoconductive substrate for mineral apposition. Furthermore, the fabrication process is gentle enough to accommodate the addition of protein therapeutics. However, this and other scaffolds that define the state of the art are still largely nonphysiological when compared to the extracellular matrix of the wound microenvironment.

Following injury, fibrinogen combines with thrombin and other clotting factors to form a clot consisting of platelets, fibrin, and other small molecules.[56] Studies in a limb-

regenerating newt model have found that following the initial clot, a transitional matrix is formed consisting of tenascin, fibronectin, and vitronectin.[96] A cartilaginous soft callus is then formed that stabilizes a fracture, which is then ossified before being gradually remodeled back to the original form (endochondral ossification). Alternatively, bone healing may skip the intermediate cartilage deposition step and bone is produced more directly (intramembranous ossification), as is the case in many craniofacial bones.[56] More recently, Zeitouni et al. found that the co-delivery of human mesenchymal stem cells along with their cell-specific extracellular matrix (ECM) enhances bone formation in a rat calvarial defect model.[88] Human MSCs seeded in their *in vitro* secreted matrix and implanted into a critical size defect produced significantly more bone than either cells or matrix alone after 3 weeks of implantation. To increase matrix production *in vitro*, cells were treated with a molecule (GW9662) to promote osteoblastic differentiation. Due to the insolubility of the cell-secreted material, it was difficult to perform a traditional proteomic analysis that would describe the precise composition of the cell-secreted matrix. Instead this group examined the gene expression of cells with GW9962, which produced more matrix than untreated cells, and found that type I, III, V, VI, XI, XII, XIV, XV, and XXI collagen genes were up-regulated. Nonfibrillar collagens (such as type V, VI, XI, XII, XIV and XV) play a role during skeletal development, and were suggested to be responsible for the enhancement in osteogenesis. Additionally, this group suggested that bioconditioning of orthopaedic biomaterials may confer a similar advantage. Since a control scaffold was not included, it is not clear from this study that a cell-secreted matrix confers an additional advantage beyond acting as a scaffolding material.

Lin *et al*. reported that MSC-derived matrices significantly increased proliferation, attachment, migration, and differentiation compared to type I collagen.[97] This result suggests an improvement over type I collagen sponges for bone repair. In contrast to Zeitouni *et al*., Lin *et al*. attribute the observed enhancement to non-collagenous proteins. Further work is needed to elucidate the role of ECM proteins in bone repair, however the ability to leverage the signals provided by the ECM to promote regeneration could improve the efficacy of cell-based bone repair strategies.

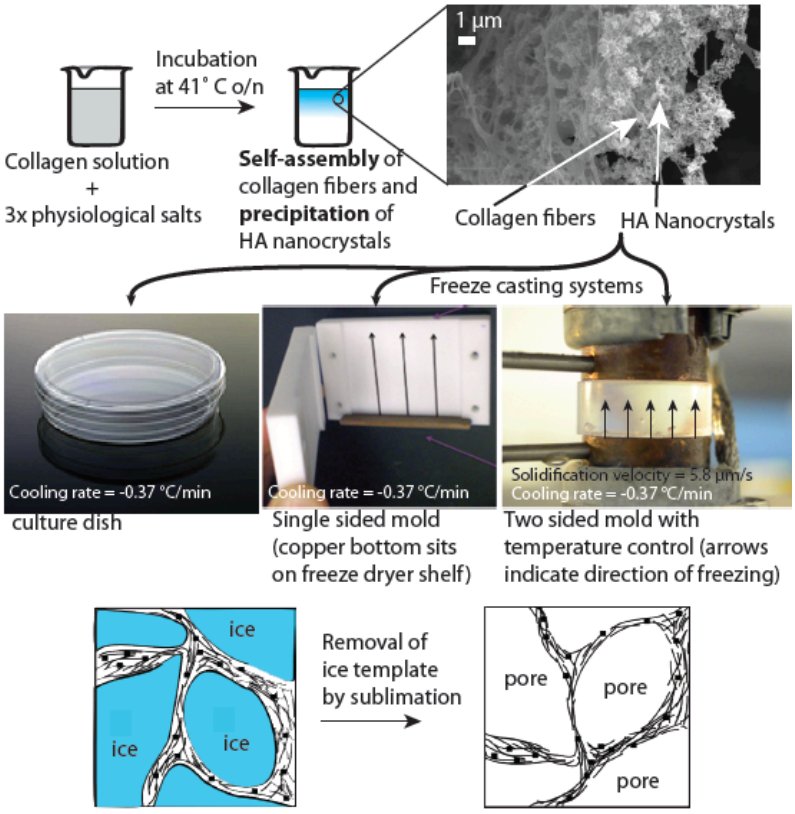


**Figure 1-20 | Collagen-HA scaffold fabrication.** A collagen-HA composite is made by collagen fiber self assembly in the presence of HA nanocrystal precipitation from a physiological salt solution. Then a mixture of water and the collagen-HA composite is frozen in one of three systems: (1) culture dish, (2) single sided mold and (3) double sided mold. The single sided mold cools in the upward direction via a copper plate at the base that is exposed to the cooling shelf of a freeze dryer. The double sided system has

integrated temperature control of the top and bottom copper surfaces, allowing tuning of the freezing rate.[98,99]

## 1.5 2-Photon Microscopy

The unique value that 2-photon microscopy provides is the ability to generate a three-dimensional view of cells in their microenvironment that can be followed through time, even in living tissue. This method has found application in many fields such as neuroscience,[100,101] immunology,[102–105] and skeletal biology[60,106], among others. Compared with other imaging tools such as X-ray tomography or magnetic resonance imaging, 2-photon microscopy is the only method capable of imaging living biological tissue at cellular resolution (Figure 1-21). Furthermore 2-photon microscopy is a version of fluorescence microscopy, which enables the tracking of any cell or molecule of interest using fluorescent proteins. As new fluorescent markers are developed, further expanding the already vast library of fluorescent probes, this technique will become even more useful to the researcher.

The theory of 2-photon fluorescence was described by Maria Goeppert-Mayer in 1931 in her doctoral dissertation entitled "Über Elementarakte mit zwei Quantensprüngen" which translates from German to English as: "Elementary Acts With Two Quantum Jumps".[107,108] Goeppert-Mayer would later win the Nobel Prize in Physics in 1963 for her theory of the nuclear shell model of the atomic nucleus. She became the second woman to win a Noble Prize in Physics, following Marie Curie in 1903. It wasn't until almost 60 year later that this technique was experimentally proven by Winfried Denk and Watt

Webb at Cornell University.[109] Since then, the popularity of this technique has risen exponentially.[110]

### 1.5.1 Multiphoton fluorescence

Fluorescence can be defined as the cyclical process by which a fluorophore is brought to an excited state, releases energy (through heat and light emission), and returns to a ground state. This is depicted in Figure 1-22 (top row). First a fluorophore is excited by an incoming photon of light at a given wavelength. Some energy is lost due to heat in the form of molecular vibration. The fluorophore then returns to its ground state through the emission of a wavelength of light that is longer then the excitation wavelength. Noting light energy is inversely proportional to wavelength ($E \sim 1/\lambda$; i.e. longer wavelength corresponds to lower energy), the emission wavelength must be longer than the excitation wavelength since energy is lost to heat following excitation. The difference between the excitation and emission wavelength is known as the Stokes shift. For 2-photon excitation, the same basic process is at play, with the crucial difference being that two photons provide the excitation energy, each with half the energy required by single photon excitation (Figure 1-22, bottom row). Furthermore, light scattering (the dominant effect limiting imaging deep in tissue) scales with $1/\lambda^4$, therefore longer wavelength light scatters less, allowing deeper penetration with 2-photon sources.

It is important to note that the likelihood of two photons impinging on a fluorophore at the same exact moment is extraordinarily rare under normal conditions. Denk and Svoboda illustrate this point through the following example[111]: Considering if sunlight

was used as the source, it would take over 10 million years for a 2-photon event to excite even the most efficient of absorbers. By contrast, single photon events would occur once every second. Waiting for a 3-photon event would exceed the age of the universe!

Multiphoton excitation requires extremely short-pulse lasers to provide a very high number of photons to the sample, dramatically increasing the probability of this event occurring within a suitable timeframe for imaging. This fact is largely why it took almost 60 years after the theoretical groundwork was laid for multiphoton excitation to be experimentally proven, in particular the development of mode-locked sub-picosecond pulsed lasers that could provide the required high photon density. An added benefit of excitation occurring only in regions of high photon density is that the excitation region is limited to a point for 2-photon microscopy versus an hourglass-like volume for a confocal microscopy, which is a single-photon technique (Figure 1-23). This translates to benefits to the user such as reduced photobleaching, less scattering due to out-of-plane excitation, and no requirement of pinholes (applied in confocal microscopy) used to block out-of-focus light.

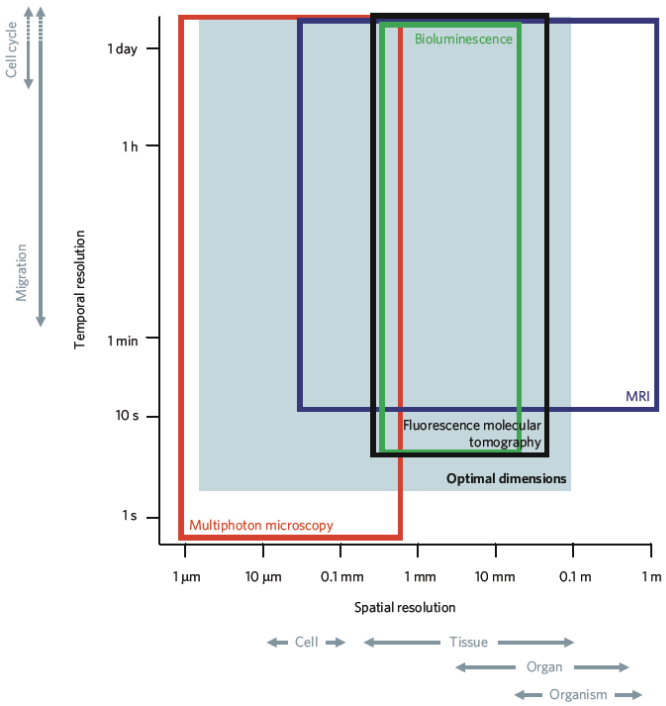


**Figure 1-21 | Imaging modality comparison across temporal and spatial scales.** Note the high temporal and spatial resolution of multiphoton microscopy. From Schroeder.[112]

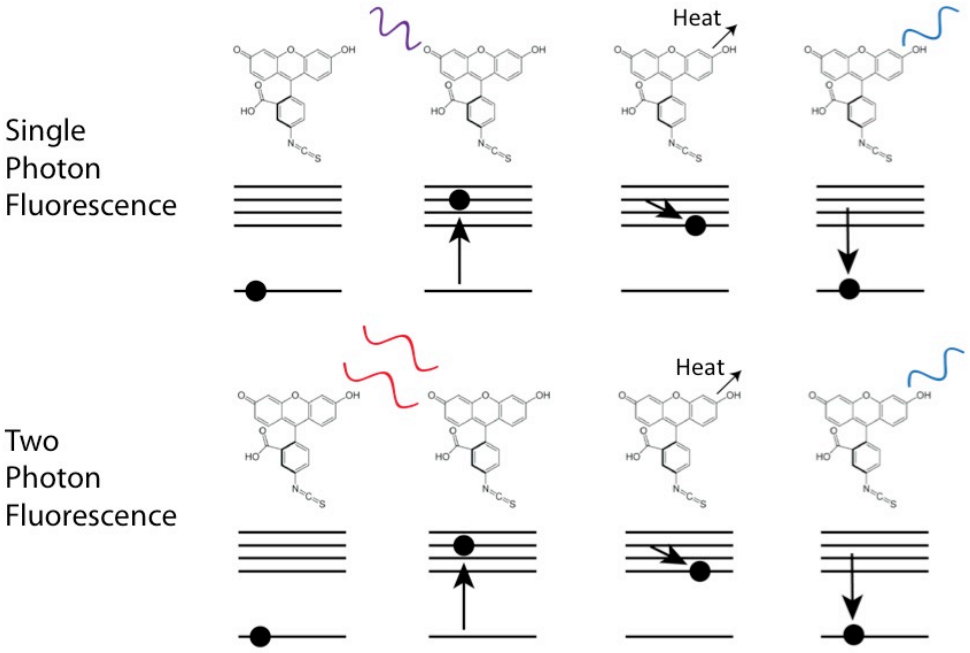


**Figure 1-22 | Single photon versus 2-photon fluorescence.** (Top row) A fluorophore starting in a ground state is brought to an excited state by an incoming photon of light. Energy is lost through vibrations and the fluorophore is reduced to a lower, yet still excited, state. A longer wavelength of light is emitted from the fluorophore, returning it

to a ground energy state. (Bottom row) 2-photon fluorescence proceeds in the same manner as single photon fluorescence (top row) except two photons excite the fluorophore, each with half the energy of the single photon excitation. Fluorophore pictured is fluorescein isothiocyanate.

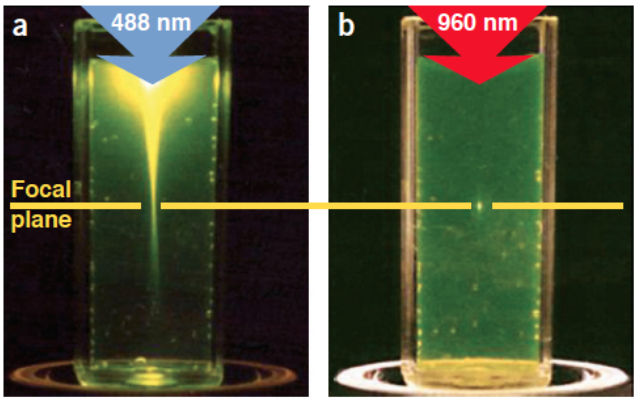


**Figure 1-23 | Comparison of the excitation volumes of single and 2-photon fluorescence.** Each cuvette holds a fluorescent dye, on the left excited via single-photon fluorescence and on the right via 2-photon fluorescence. At left, the exciation volume is large, extending well beyond the focal plane. At right, the 2-photon excitation is a single point, greatly restricted to the focal plane. Image from Zipfel.[110]

### 1.5.2 Second harmonic generation

Another extremely useful aspect of 2-photon microscopy in living systems is the visualization of some biological molecules with no fluorescent labeling at all. Molecules such as type I collagen produce a so-called second harmonic signal, which is a frequency doubling of incoming light through the interaction with the noncentrosymmetric structure of the collagen triple helix.[113–117] For example, if a collagen-containing sample is excited at 900 nm, a second harmonic signal will emerge at 450 nm. The generation of second harmonics was first proven in 1961 using quartz and newly developed lasers.[118] Ten years later, second harmonic generation in biological tissues was demonstrated.[119] A second harmonic can be found in any tissue containing sufficient concentrations of type I

collagen. Since roughly 90% of the inorganic fraction of bone is type I collagen, bone generates a strong second harmonic signal (Figure 1-25), and the different patterns of collagen orientation in mineralized and unmineralized tissue can be visualized. Of particular importance to bone formation, differences between woven and lamellar bone can be appreciated with this approach. Finally, since the second harmonic signal relies on the triple helical unit of type I collagen, this method has also been used to differentiate between triple helical and non-triple helical collagen (gelatin),[120] which has important implications for the how cells interact with this protein.[121]

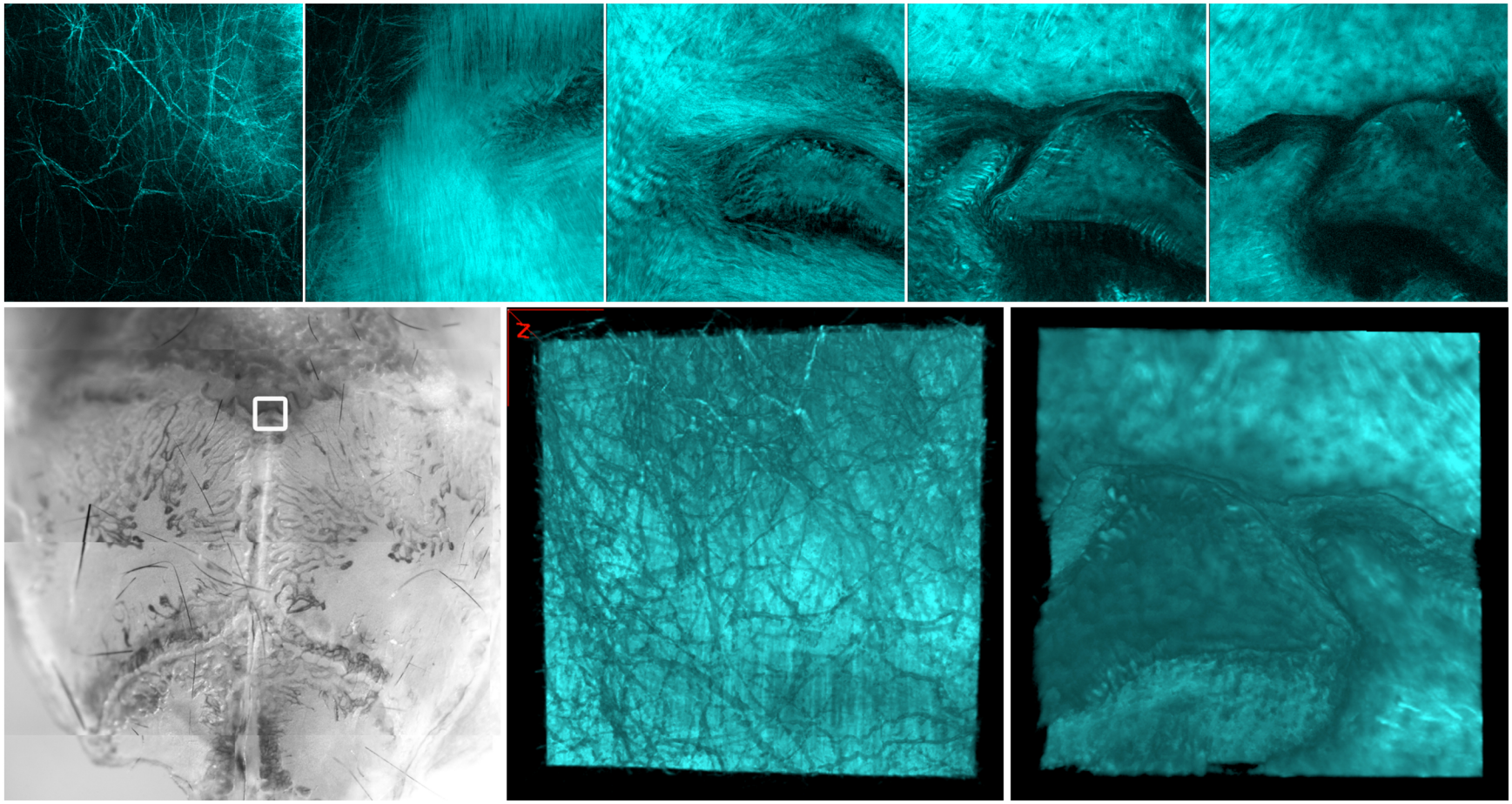

**Figure 1-24 | Second harmonic signal showing different levels of collagen organization in mouse calvarial bone and periosteum.** (Top row, left to right) Single slices form a z-stack of second harmonic images starting from periosteal layer into the marrow space and calvarial bone. Sharpey's fibers are clearly visible in the marrow space. (Bottom row, left to right) Image of mouse calvarium view from the top, small white box indicates the area of interest shown with second harmonic imaging. Rightmost panels are top and bottom views of three-dimensional reconstructions of the second harmonic z-stack.

# 2 Specific Aims

The overall goal of this project was to better our understanding of cell-based bone tissue engineering and improve *in vivo* bone defect repair using mesencyhmal stem cells and a collagen-hydroxyapatite scaffold.

**AIM 1 | Establish a 2-photon platform for imaging bone tissue engineering *in vivo*.** The interactions between cells and biomaterials that lead to osteogenesis are not yet well understood and are difficult to observe. By providing a description of a tissue microenvironment across multiple time points in the same animal, 2-photon microscopy could provide a more continuous perspective than has previously been shown.

**AIM 2 | Improve the repeatability of *in vivo* bone formation with an in-house made collagen-HA scaffold.** A well-defined, open platform is important to the development of scaffold technology. Thus we must be able to produce scaffolds capable of repeatedly forming bone.

**AIM 2a |** Fabricate a sterile collagen-hydroxyapatite scaffold system without compromising material performance.

**AIM 2b |** Determine viability, progenitor distribution, and optimal seeding conditions for murine BMSCs in a collagen-HA scaffold.

**AIM 3 | Evaluate the effect of cell-derived ECM in a collagen-HA scaffold to enhance *in vivo* bone formation.** Current scaffolds are still largely nonphysiological and thus rely on comparatively less potent signaling mechanisms than the *in vivo* milieu. The

application of ECM combined with collagen-HA scaffolds could improve cell-based bone formation.

# 3 Visualizing Osteogenesis *In Vivo* Within a Cell–Scaffold Construct for Bone Tissue Engineering Using Two-Photon Microscopy

## 3.1 Introduction

Regeneration strategies employing a scaffold material combined with cells have shown early success in the clinic,[85] with others rapidly approaching this stage.[122,123,124] However, the cellular mechanisms underlying regeneration are not yet well understood.[125,126] Describing the progression of host-donor-biomaterial interactions behind a successful or unsuccessful therapy is still a difficult process, yet is central to the safe transfer of basic research to a clinical setting. For example, what is the fate of seeded cells? How do these cells induce or conduct repair? What are the cell and scaffold interactions governing a successful or unsuccessful therapy? In order to understand the impact of a given regenerative strategy on the resultant cellular interactions, it is first necessary to observe them.

*In vivo* microscopy has dramatically contributed to our understanding of development,[127] neuroscience,[100,128–130] immunology[102,104,105,131–133] and stem cell dynamics[60,106,134]. Much of this work relies on 2-photon microscopy, the theoretical foundation of which was conceived in 1931[107] and put into practice in 1990.[109] Due to a longer excitation wavelength than conventional fluorescence microscopy, 2-photon microscopy provides deeper tissue penetration, allowing observation of cellular dynamics *in situ* and *in vivo*.[103]

Additionally, a longer excitation wavelength enables collagen to be visualized *in vivo* without the use of an additional stain due to its generation of a second harmonic signal.[114,117,135,136] More recently, *in vivo* fluorescence imaging and 2-photon microscopy have been applied to tissue engineering applications.[39,137] Concurrently, X-ray tomography[64,138] and whole body fluorescence measurements[139] have also provided insights into the cellular interactions governing regeneration in live animals. However, at present, whole body fluorescence imaging does not facilitate single cell resolution and X-ray tomography does not allow integration with fluorescent reporter genes.[112] Fluorescent reporter genes have allowed tracking of lineage specific cell populations *in vitro* or *in vivo* without additional stains. Histology can provide a large field of view of reporter gene activity within a tissue of interest, however, the process compromises the viability of the tissue and the microenvironment can be physically disturbed due to sectioning. Therefore, 2-photon microscopy has the distinct advantage of visualizing tissue at single-cell resolution *in vivo* and *in situ* in three dimensions.[60] By providing a description of a tissue microenvironment across multiple time points in the same animal, 2-photon microscopy provides a more continuous perspective than has previously been shown using different animals at each time point.

This paper describes the establishment of a 2-photon microscopy platform to examine cell-scaffold based therapies for bone regeneration *in vivo*. To establish a live animal imaging platform, experiments were conducted in two steps: (i) to describe the initial calvarial microenvironment prior to injury repair, and (ii) to observe the interaction of cells, scaffold, and new bone during tissue-engineered regeneration in a calvarial defect

model. In order to provide an unambiguous description of the spatial context in which the three dimensional 2-photon data reside, the microenvironment of calvarial bone is described starting with two-dimensional techniques of histology and stereomicroscopy, and then with three-dimensional 2-photon live animal microscopy. Each imaging technique provides a different perspective; stereomicroscopy provides a global view, histology a cross-section, and 2-photon a three dimensional volume.

We have previously employed a calvarial defect model of bone repair in combination with transgenic mice carrying reporters for cells in the skeletal lineage.[89,92,140] In order to assess the cellular interactions within our cell-scaffold system, a murine critical size calvarial defect model was used because the calvarium is thin and reasonably accessible to a microscope objective. Tissue engineered bone formation was observed in animals at four and six weeks after implantation of a scaffold and donor bone marrow stromal cells (BMSCs). 2-photon microscopy during tissue engineered bone formation enabled visualization of host cells, donor cells, scaffold and type I collagen at two time points, *in vivo* and *in situ.*

## 3.2 Materials & Methods

### 3.2.1 Live animal imaging

A bone mineralization label (alizarin complexone) was injected into the tail vein of the mouse to be examined one day prior to an imaging session. On the day of imaging, the mouse was anesthetized with a ketamine (135 mg/kg) – xylazine (15 mg/kg) blend. If the vasculature was to be visualized, 100 μL of rhodamine-labeled dextrans (50 μg/μL) were

injected into the tail vein. The skin above the calvarium was shaved and a u-shaped incision was made (Fig. 3-1a). The skin flap was sutured to an area above the nose and the animal was placed in a stereotaxic frame (Mouse and Neonatal Rat Adaptor #51625, Stoelting). The head was stabilized at three points by two blunt ear bars and a bite bar (Fig. 3-1a). The animal was then placed beneath a 2-photon microscope (Ultima IV, Prairie Technologies, Fig 3-2). Adjusting the height of the ear bars leveled the exposed calvarium. The calvarium was imaged with a water immersion objective (XLUMPlanFL 20x/0.95W, Olympus) in sterile PBS. To acquire a stack of images through the depth of the calvarium, a 459 by 459 μm area was scanned in the x-y plane while the z depth was increased by 1 μm increments, controlled by the acquisition software (Prairie Viewer, Prairie Technologies). All fluorophores were excited at 900 nm and data were collected in four channels with the following filter limits: channel 4, 435-485 nm; channel 3, 500-550 nm; channel 2, 570-620 nm; and channel 1, 640-680 nm. When exited at 900 nm, type I collagen emits a 450 nm second harmonic; this signal was detected in channel 4. Cyan fluorescent protein-expressing osteoblasts (Col3.6cyan) were detected in channels 3 and 4. Yellow fluorescent protein-expressing osteoblasts (Col3.6topaz) were detected in channels 2 and 3. Emerald green fluorescent protein-expressing osteoprogenitors, osteoblasts, and osteocytes (SMAAemd, Col2.3emd) were detected in channel 3. The scaffold (Healos®, DePuy) was autofluorescent in all channels. Rhodamine-labeled vasculature and alizarin complexone mineral label were detected in channel 1, but used separately in the current study. After the completion of an experiment, z-stacks were reconstructed in three dimensions using the 3D viewer plugin[141] for FIJI.[142] This study used 3-month-old B6 (SMAAemd) and CD1 (Col3.6topaz, Col3.6cyan, Col2.3emd) mice

(Fig. 3-1a). All procedures in this study were approved by the UConn Health Center Institutional Animal Care and Use Committee (IACUC).

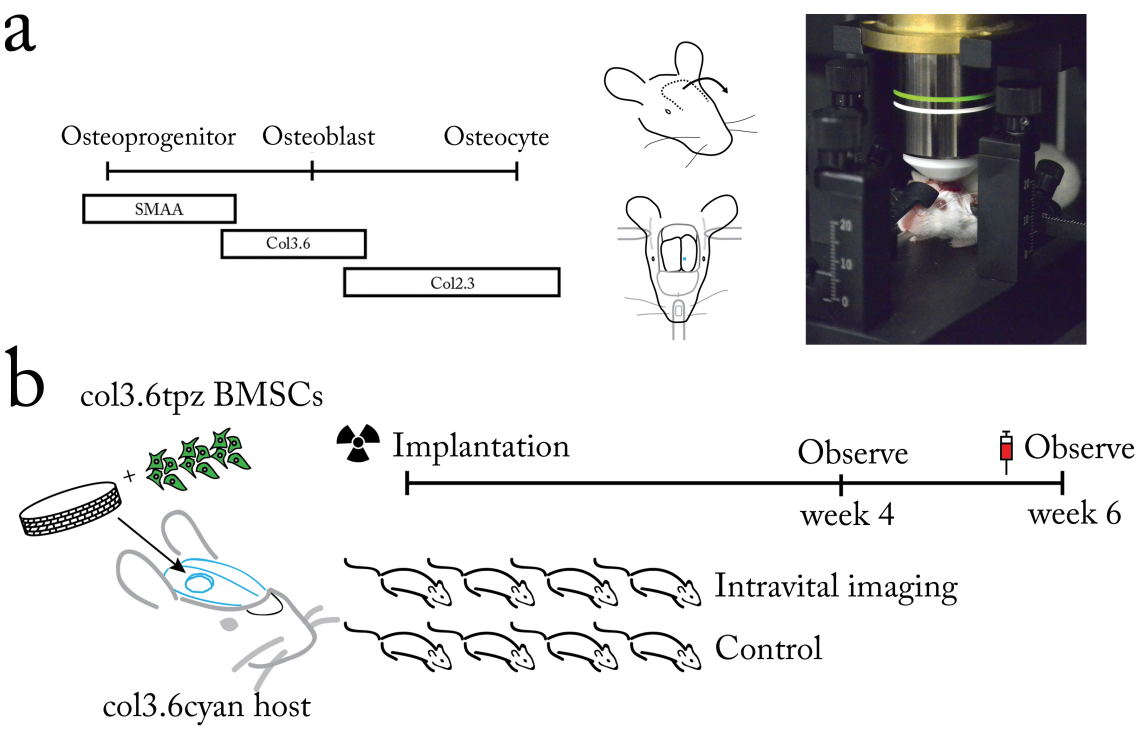


**Figure 3-1| Examination of skeletal cells in native and tissue engineered bone with live animal microscopy.** (a) Reporters of the skeletal lineage used in this study, surgical procedure and animal stabilization on the microscope. Left, skeletal lineage reporters used in this study. Middle, the calvarium was exposed by incision and the skin flap was sutured down. The stereotaxic frame stabilizes the head by three-point fixation at the ear canals and front teeth. Right, animal positioned under the objective lens of the 2-photon microscope. (b) Observing tissue engineered bone regeneration. Col3.6topaz BMSCs were seeded onto a collagen-HA scaffold and implanted into a Col3.6cyan host. Host animals were irradiated and given a bone marrow transplant to prevent immunorejection of donor cells. At both 4 and 6 weeks later, animals in the imaging group were examined by 2-photon microscopy. For comparison, the control group did not undergo imaging surgery. To visualize the mineral surface, alizarin complexone was injected into both groups one day prior to sacrifice.

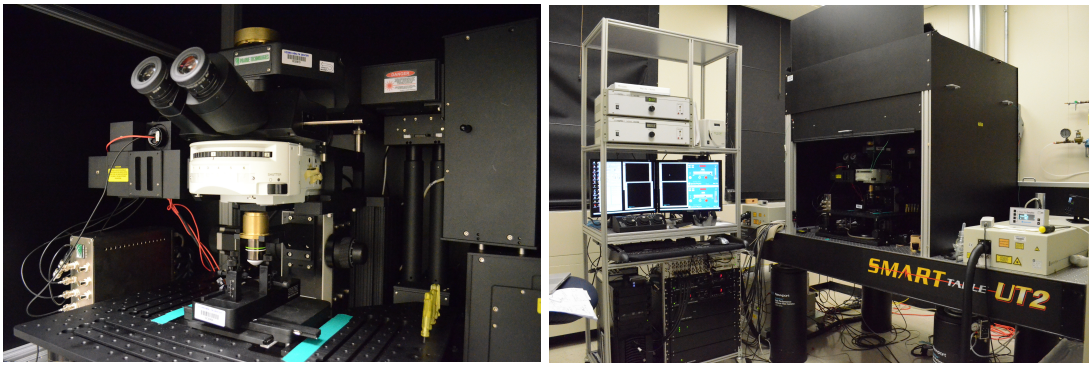


**Figure 3-2 | 2-photon microscope at the University of Connecticut Health Center.** At left, the microscope eyepiece, brass objective lens and stage are shown. At right, the vibration isolation table with microscope, two femtosecond Ti:Sapphire lasers on the left and right of the microscopy shroud are pictured. The computer workstation with x, y and z stage control is also visible.

### 3.2.2 Calvarial defect model of tissue engineered bone

Bone marrow stromal cells were isolated from the femur and tibia of CD1 wild type and Col3.6topaz animals for bone marrow rescue following irradiation and scaffold seeding, respectively. Cells were plated in α-MEM (Gibco) containing 10% FBS and 1% penicillin-streptomycin. Following isolation, cells were allowed to attach in an incubator at 5% $CO_2$, ambient $O_2$ and 37 ˚C. After 7 days of culture, Col3.6topaz cells were trypsinized and seeded onto a collagen-hydroxyapatite scaffold (Healos®, DePuy Spine) at a density of $1.0\times10^6$ cells/scaffold at the time of implantation. To prevent immunorejection of the cell-scaffold implant, Col3.6cyan host animals underwent 900 rads of irradiation to ablate the bone marrow 1 day prior to implantation. Host animals subsequently received a bone marrow transplant of $1.5\times10^6$ cells from wild type CD1 animals via retro-orbital sinus injection. Animals were anesthetized with a ketamine (135 mg/kg) – xylazine (15 mg/kg) blend and a 3.5 mm diameter defect was introduced in the right parietal lobe using a Dremel® MultiPro drill with a trephine bit. Extreme care was

taken to prevent damage to the dura mater beneath the calvarium. After the scaffold-cell construct was placed in the defect, the incision was closed with resorbable sutures and the animals were given analgesic (bupronephrine, 0.08 mg/kg). To enable imaging at four and six weeks, animals were anesthetized, and an incision was made above the defect area. To assess the effect of imaging surgery on bone formation, two groups of animals were used (Fig 3-1b). One group (n=4) underwent surgery to expose the calvarium and was subsequently imaged with *in vivo* 2-photon microscopy at four and six weeks post-implantation. The other group (n=4), acting as a control, did not undergo surgery or imaging. Both groups were sacrificed at six weeks post-implantation and examined with histology and X-ray imaging.

### 3.2.3 Histology, stereomicroscopy and X-ray imaging

Concluding a 2-photon experiment, animals were sacrificed by $CO_2$ asphyxiation. The calvaria were dissected, placed in 10% formalin at 4 °C for 1 day and then in 30% sucrose solution overnight. Photographs and X-ray images (LX60, Faxitron) were taken. The calvaria were placed then in sucrose solution in a culture dish beneath the stereomicroscope objective (Lumar V12, Zeiss). Images were acquired on the stereomicroscope using a digital camera (Axiocam, Zeiss) and filter set (49002, 31002 & 31043, Chroma). Images were acquired at different locations using stage automation; these resultant images were stitched together with acquisition software (AxioVision, Zeiss) in order to capture a large field of view. Following stereomicrosopy, each calvarium was covered with embedding medium (Cryomatrix, Termo Shandon) and affixed to an aluminum stage for cryosectioning. Thin sections (7 μm) of tissue were

transferred via tape (Cryofilm, Section-Lab) to a plastic slide. Sections were then rinsed three times in PBS, followed by distilled water, and placed on a glass slide. A 50% glycerol solution was applied to the section and a glass coverslip was placed on top. Images of finished slides were acquired with a fluorescent microscope (ImagerZ1, Zeiss) equipped with a digital camera (Axiocam, Zeiss) and filter set (49002 & 31002, Chroma).

### 3.2.4 Image analysis

To quantify integration of host bone with the edge of the scaffold, a Euclidean distance analysis[106] was performed on X-ray images of calvaria in dorsal view from both groups using FIJI[142]. First, the inside edge of the host bone was selected manually with an elliptical region of interest (ROI) and saved for the following step. The entire image was then cleared to white (8-bit grayscale value of 255) and the outline of the saved ROI was drawn in black (8-bit grayscale value of 0) on the white image. A Euclidean distance map (EDM) was produced from this image, coding each white pixel a grayscale value corresponding to its distance in pixels from the black ROI representing the edge of the defect. A duplicate of the original X-ray image was then converted to a binary image (0 or 255 only) by setting pixels above a threshold value to 0 and below to 255, for bone and non-bone pixels respectively. In order to combine the distance information from the EDM with the location of bone pixels from the binary image, the pixel values between the two images were compared, and the maximum value was chosen to form a composite image. Calculating a histogram of the composite image yielded the number of bone pixels as a function of pixel distance from the edge of the host bone. White background pixels (255) in the histogram were excluded from the analysis. The same procedure was

repeated with the entire defect area set to 0, representing the defect as theoretically filled with bone, i.e., perfect host-implant integration. To normalize these data, the histogram derived from the X-ray composite was then divided by the histogram representing perfect host-implant integration. For each group, the mean value of bone pixels was plotted as a function of distance from the edge of the defect. Pixel distance was converted to microns using the spatial calibration for the magnification used.

The area fraction of bone in the defect area was measured from histological sections using the following method. The defect was cropped with a rectangular ROI and pixels were classified as either bone or not bone using the WEKA trainable segmentation plugin[143] for FIJI. The user first identified a selection of pixels belonging to each class (bone, non-bone) and the computer classified the entire image. The misclassification error was less than 0.2% for images examined by this method. The classified image was then output as a binary image. An ROI that had been manually drawn around the defect area was applied to the classified image. A histogram was calculated, resulting in the number of bone pixels and total pixels in the ROI. Dividing the number of bone pixels by the total pixels in the ROI gave the bone area fraction in the defect.

To determine the thickness of new mineral on the host bone, an ROI was manually defined around a second harmonic signal indicative of collagen within mineralized tissue (Fig. 3-3). Our rationale for classifying a second harmonic signal as collagen within mineralized tissue is based on observing the morphology of the second harmonic signal in native bone. We also observed this morphology in areas that appeared to be new bone

formation in the defect model. When mineral label (alizarin complexone) was administered, the label localized to the surfaces of this second harmonic signal, indicating such a morphology was due to collagen within mineralized tissue. After region selection, the contents of the ROI were set to 255 and processed with the local thickness plugin[144] implemented in FIJI. This plugin calculates the thickness of a 2D region using a circle filling algorithm, coding each pixel a value corresponding to the diameter of the circle it is contained by. A histogram of the image provided the mean pixel value corresponding to the mean thickness of new mineral on the host bone. New mineral on the scaffold surface was determined using the WEKA trainable segmentation plugin to classify pixels as either scaffold or new mineral. The resultant image was used to calculate the mean thickness using the local thickness plugin. The mineral apposition rate (MAR) was calculated by dividing the mean thickness of mineral on either the scaffold or host bone by the time since implantation.

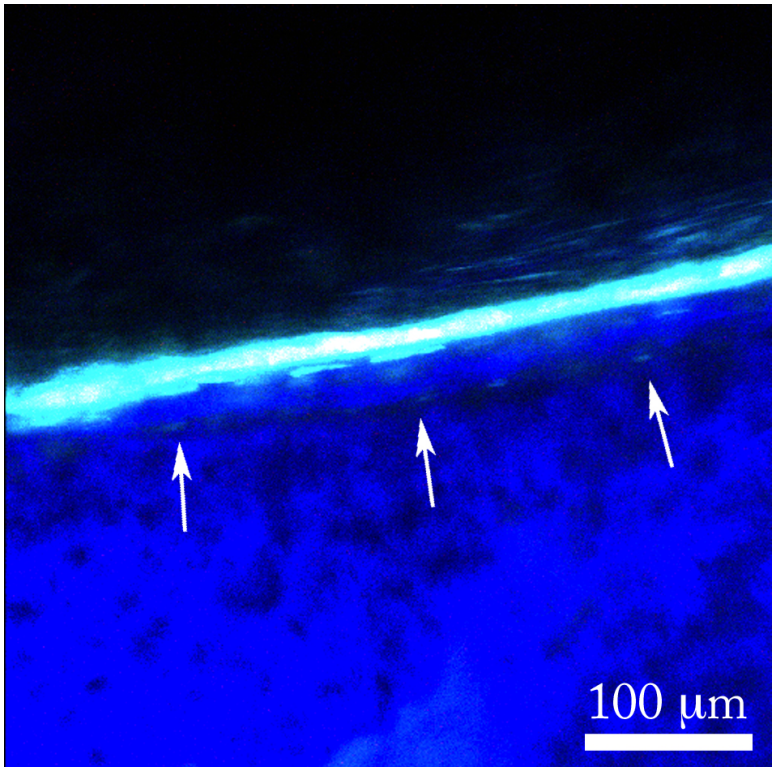


**Figure 3-3 |** Cyan host osteoblasts overlying a second harmonic signal indicative of collagen within mineralized tissue at the defect margin.

## 3.3 Results

### 3.3.1 Surveying the calvarial microenvironment in two and three-dimensions

In order to orient three-dimensional 2-photon data within the context of the surrounding tissue and aid interpretation of 2-photon data when viewed alone, a Col2.3emd[31] transgenic animal was examined with 2-photon microscopy, stereomicroscopy and histological sectioning in this order. Here we will describe the 2D data obtained by stereomicroscopy and histology first, followed by the 3D 2-photon data. The Col2.3emd reporter shows osteocytes and osteoblasts via the emerald green fluorescent protein and the mineral surface was labeled with alizarin complexone (red). Starting with stereomicroscopy, a bird's eye view of the calvarium contained osteoblasts distributed

throughout marrow spaces in the parietal bone and suture lines (Fig. 3-4a). Osteoblasts colocalized with the mineralization label covering the endosteal surface (Fig. 3-4b). Osteocytes could be seen embedded in the cortical bone (Fig. 3-4b, black arrow). Blood vessels reside within the marrow spaces of the parietal bone (Figs. 3-4b & 3-4c, white arrows are placed at identical locations). Taken together, this data represents the repeating motif of parietal bone in the calvarium.

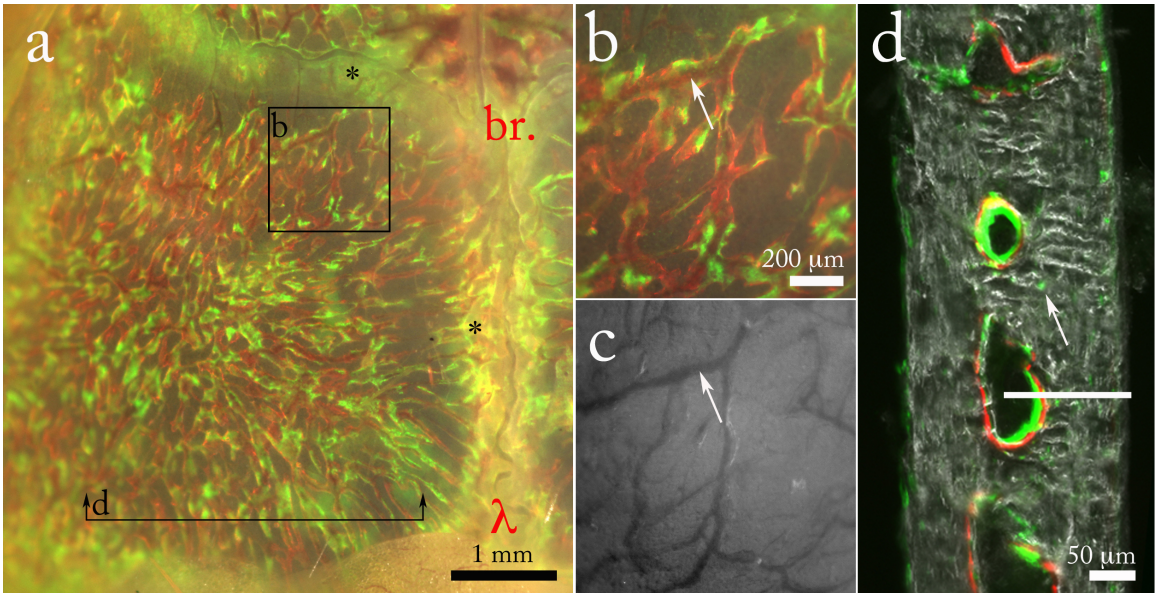


**Figure 3-4 | Osteoblasts, osteocytes and mineralization in the calvarium.** (a) View of the left parietal lobe of a Col2.3emd mouse showing osteoblasts (green) and mineral surface labeled with alizarin complexone (red). The green, red and brightfield channels are overlaid to show the colocalization of the osteoblasts and new bone label. The sagittal and coronal suture lines also contain osteoblasts, indicated by the black stars (*). The horizontal line indicates the approximate location of the cross sectional view shown in (d) The anatomical locations lambda and bregma are labeled λ and br., respectively. (b) Inset from (a) shows a magnified view of the marrow spaces located in the parietal bone. Blood vessels (white arrows in b and c) are seen within the marrow spaces. (c) Brightfield channel showing the organization of vasculature (white arrow). (d) Histological section of (a) showing Col2.3emd osteoblasts and osteocytes (white arrow) in the marrow spaces and cortical bone, respectively. Mineralization label (red) is located on the surface of marrow spaces. The white line indicates the 139 µm total depth of the 2-photon z scan shown in Fig. 3-5a.

Histology of the 200 μm thick calvarium was used to examine the same tissue in cross-section (Fig. 3-4d). From this perspective, osteoblasts overlie new mineral on the endosteal surface (Fig. 3-4d). Osteocytes are also visible in the histological view, occupying sites within the cortical bone (Fig. 3-4d, white arrow). The histological description taken together with the dorsal view obtained by stereomicroscopy more rigorously defines the three-dimensional microanatomy. The section pictured in Figure 3-4d shows marrow spaces approximately 100 μm from the periosteal surface of the bone to their center. Due to light scattering, the 2-photon microscope cannot image completely through the calvarial bone, however, marrow spaces are routinely reached. The white bar in Fig. 3-4d indicates the maximum depth (139 μm in this case) of the 2-photon stack shown in Fig. 3-5a.

Lastly, the 2-photon z-stack previously taken of the parietal bone from the same animal shows a woven pattern of collagen fibers at the surface of the calvarium, visible by its second harmonic signal[114,117,135,136] (Fig. 3-5a, 10 μm). As the scan moves into the calvarium, many dendritic osteocytes were visible occupying lacunae in the cortical bone (Fig. 3-5a, 34 μm). Moving into the marrow space (Fig. 3-5a, 64 and 93 μm), Col2.3emd osteoblasts are seen at high density lining the endosteal surface labeled in red. At 120 μm, the sharpness of the image begins to degrade due to scattering in the tissue (Fig. 3-5a, 120 μm). The description of the calvarial microanatomy with stereomicroscopy, histology, and 2-photon microscopy provides a robust framework for the interpretation of 2-photon data when viewed alone.

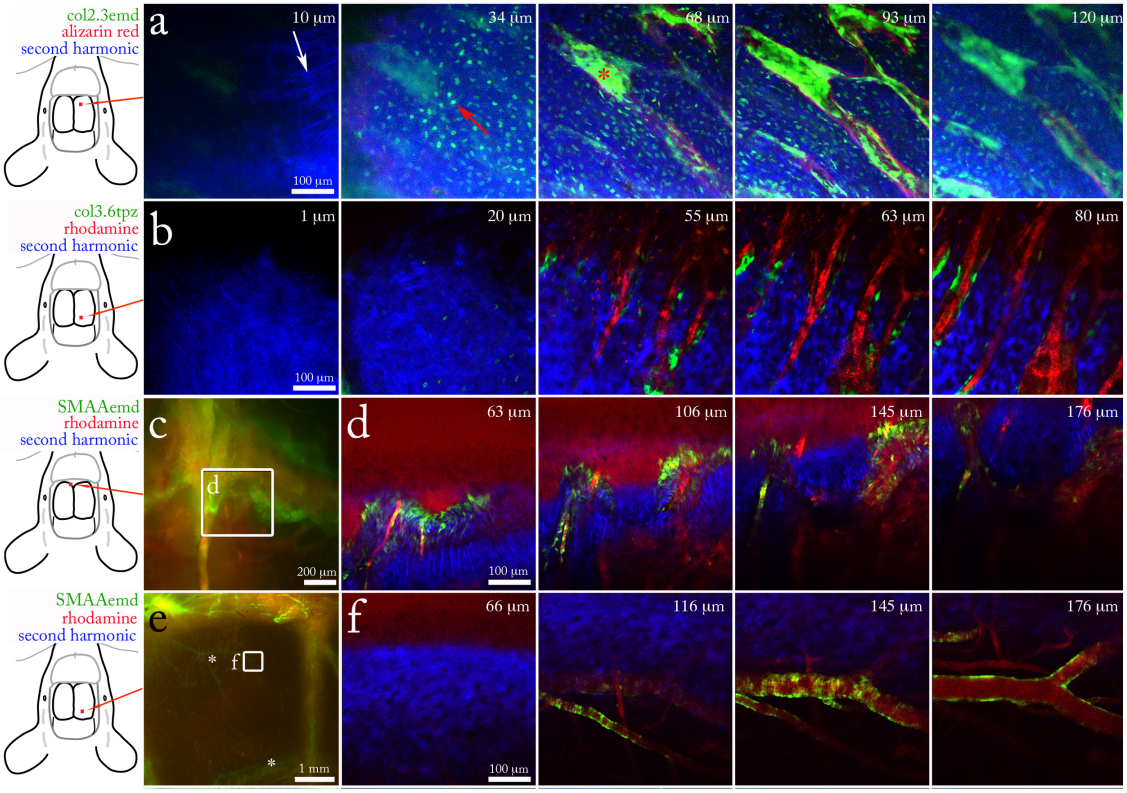


**Figure 3-5 | 2-photon live animal imaging of skeletal reporters in pristine bone.** (a) 2-photon z-stack through mouse calvarial bone carrying a Col2.3emd reporter (green) and alizarin mineral label (red). Red square on leftmost diagram indicates the x-y imaging location. 10 µm slice shows collagen fibers, white arrow. 34 µm slice contains osteocytes, red arrow. (b) Parietal bone carrying a Col3.6topaz reporter (green) and rhodamine labeled dextran in the vasculature (red). Osteoblasts localize in the area between the vasculature and the endosteal surface of bone. (c) Stereomicroscopy (leftmost panel) and 2-photon z-stack of suture line containing SMAAemd osteoprogenitors (green) and rhodamine labeled blood vessels (red). (d) Z-stack of SMAAemd osteoprogenitors shown in inset of (c). (e) Stereomicroscopy (leftmost panel) and 2-photon z-stack of large blood vessels in the parietal bone labeled with SMAAemd. (f) Smooth muscle cells labeled with SMAAemd wrap around rhodamine labeled blood vessels.

### 3.3.2 2-Photon imaging of skeletal lineage reporters

We used the reporters SMAA[145] (osteoprogenitors), Col3.6[43] (early osteoblasts) Col2.3[31,43] (mature osteoblasts and osteocytes), (Fig. 3-1a) in order to describe their baseline expression in the cellular microenvironment prior to use in later experiments. The starting tissue is rarely characterized prior to a regeneration study, yet this is an

important step in understanding where responsible cells may originate. Col3.6 osteoblasts are present in the marrow spaces of the parietal bone and inside the suture lines. Blood vessels residing in the marrow space were visualized with a rhodamine injection (Fig. 3-5b). The SMAA transgene marks vascular lining cells, myofibroblasts, and a population of osteoprogenitor cells.[145] We observed SMAAemd cells in the suture lines (Figs. 3-5c & 3-5d) and in the smooth muscle lining of blood vessels (Figs. 3-5e & 3-5f). This result implies that in a repair scenario involving resident SMAA osteoprogenitors, these cells would have to migrate from the suture lines to the site of injury. Taken together, these data form a part of the host's cellular initial conditions preceding a bone defect in the calvarium.

Collagen content and organization contribute to the mechanical properties, mass transport, and cell motility of living tissue.[146] Collagen is readily observed in the calvarium by its generation of a second harmonic.[114,117,135,136] We observed distinct features of collagen organization in the calvarial suture microenvironment. On the upper surface of the calvarium, the periosteal membrane contained highly organized collagen fibers in a woven pattern (Fig. 3-6, red star, 19 μm). Deeper down, inside the cortical bone (Fig. 3-6, 63-109 μm), collagen within mineralized tissue produces a more uniform second harmonic signal than nonmineralized membranous collagen. Within the suture space there are many strands of wavy collagen fibers. These strands, collectively known as Sharpey's fibers,[147] terminate in bundles along the wall of the marrow space at a regular interval , 109 μm). Second harmonic imaging also allowed stain-free visualization of collagen-based scaffolds (Fig. 3-7).[135] These results provide the template of collagen in

the periosteal membrane, suture space, and cortical bone in the host calvarial microenvironment preceding injury.

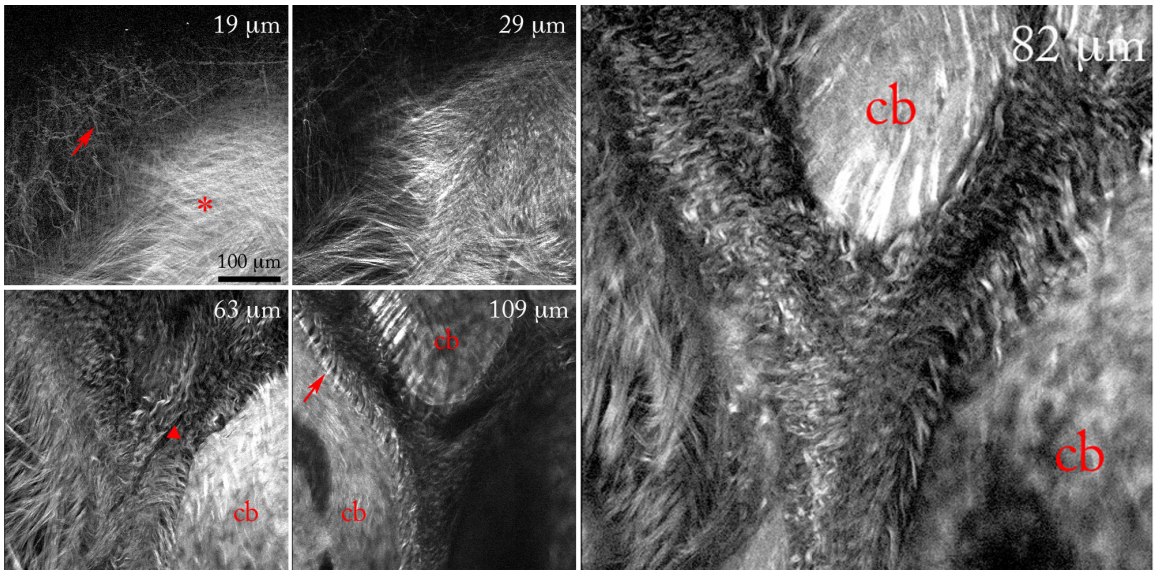


**Figure 3-6 | Collagen organization in the calvarial suture microenvironment.** Second harmonic signal shows the organization of collagen fibers in the suture space. 19 µm: The top layer of the calvarium shows loosely organized fibers (red arrow) followed by more densely packed woven fibers (red star). 29 µm: Woven collagen of the periosteum. 63 µm: Woven fibers give way to wavy fibers inside the marrow space (red triangle). Cortical bone (cb) shows a uniform second harmonic signal with the exception of bright streaking at insertion sites of collagen fibers from the marrow space into bone. 82 µm: Wavy fibers within the marrow space, surrounded by cortical bone (cb). 109 µm: Bundles of collagen fibers insert in collagen bone (red arrow). Fibers bundles (red arrows) are placed at regular intervals along the marrow wall.

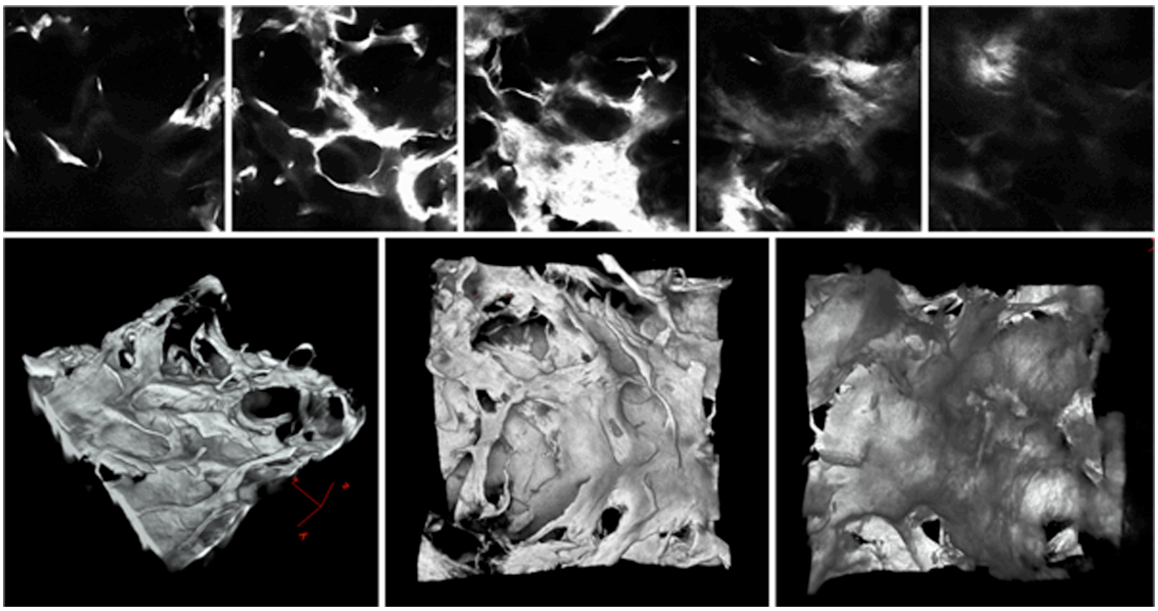

**Figure 3-7 | Second harmonic generation by a collagen-hydroxyapatite scaffold.** Top row: Individual slices taken from the top to bottom of a z-stack. Bottom row: Isometric, top view and bottom view of a three dimensional reconstruction of the z-stack presented above.

### 3.3.3 Tissue-engineered defect repair

At four and six weeks post-implantation of a scaffold seeded with BMSCs, animals were observed with 2-photon microscopy (Fig. 3-1b). Two locations were examined in each animal: an area in the central part of the implant and at the edge of the defect. At week four, in the central part of the defect, a woven layer of collagen containing weakly expressing Col3.6cyan host cells with spindle-shaped morphology surrounded the implant on the top surface (Fig. 3-8d, panel 2). Host cell density was high in this layer above the defect. Relatively few donor cells were observed in this fibrous layer. Underneath the fibrous layer, scaffold and donor cells were visible (Fig. 3-8d, panel 4-6, supplementary movie). Due to it's spectrally broad autofluorescence, the scaffold appeared whitish in color, distinguishable from cells and the second harmonic signal (Fig. 3-8d, red arrows). A second harmonic signal similar to that observed in native bone was

observed overlying the scaffold surface, suggestive of collagen in new mineral. The apposition rate of this layer on the scaffold surface was 0.69 +/- 0.48 μm/day (n=3, in one sample the implant was completely resorbed). Bright Col3.6topaz donor cells with osteoblastic cuboidal morphology populated the scaffold region, with some cells fully embedded in the new layer covering the scaffold surface. Donor cell density appeared moderate, with clusters of cells overlying the second harmonic layer indicative of new mineral. At the perimeter of the host bone four weeks after implantation, again a layer of host cells populated a fibrous layer above the scaffold and host bone. Similar to the central defect region, a few donor cells were visible in the fibrous layer (Fig. 3-8e). In contrast to more disparate clustering of donor cells in the implantation site, host cells formed a dense layer of bright Col3.6cyan osteoblasts on the surface of the host bone. Host cell density and cell-cell contact appeared to be greater on the surface of host bone than donor cells on the scaffold in the central defect region (Fig. 3-8d & 3-8e, panel 4 and below). This dense layer of host cells appeared to be depositing new mineral on the edge of host bone towards the central implant region (Fig. 3-3). The mineral apposition rate calculated from the thickness of the new mineral layer and the time since implantation was 1.88 +/- 0.13 μm/day (n=2, the edge of the original defect was not visible in the other samples). Some host cells were observed embedded in mineral behind the mineralization front. These results indicate bone formation had occurred on the scaffold, predominantly by donor cells, and on the host bone, predominantly by host cells, at four weeks post-implantation.

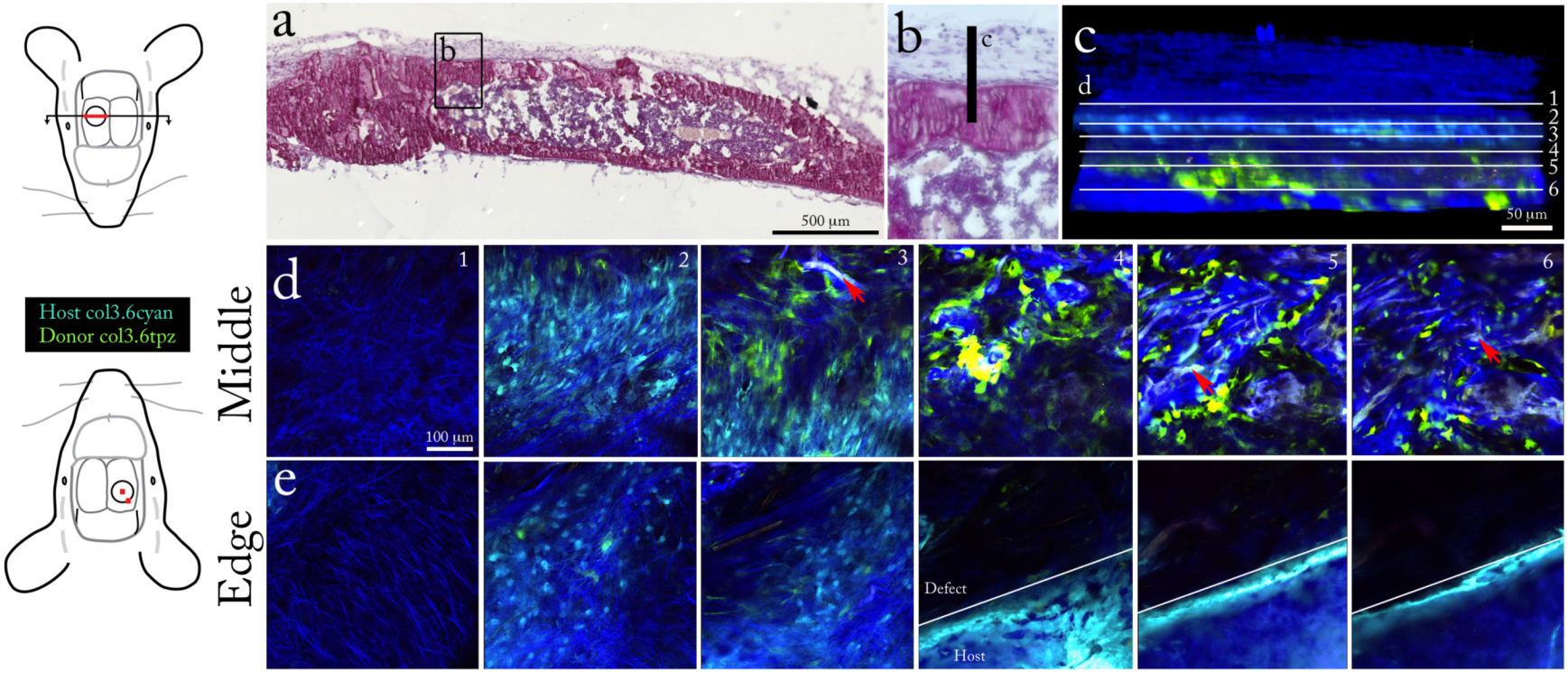


**Figure 3-8 | Donor cells mineralize scaffold *in vivo*.** (a) Hematoxylin stained section of the implant obtained after the conclusion of imaging. Diagram at left shows the location of the cross-section, highlighted in red, with respect to the circular defect. Inset (b) shows the area viewed by 2-photon live animal microscopy (c). (c) Three-dimensional reconstruction of 2-photon z-stack viewed side-on providing a histological orientation. White lines indicate the position of the 6 slices shown in (d). (d) 2-photon z-stack through the middle of the defect area at 4 weeks post implantation. Diagram at left shows the location of the z-stack with respect to the defect (red square in middle of defect). Host cells are seen populating a layer of collagen fibers above the implant area (slice 2). Scaffold is visible due to autofluorescence (slice 3, 5, and 6, red arrow) and has a dense second harmonic signal on the surface, shown in blue. Donor cells populate the implant region (slice 4, 5, and 6). (e) 2-photon z-stack through the edge of the defect area at 4 weeks post implantation. A layer of host cells covers the top surface (slice 2$^{nd}$ from left). Deeper into the stack, host osteoblasts form a dense layer on the surface of host bone. All 2-photon images share the scale bar shown in the leftmost tile of (d).

Using the pattern of the scaffold network as a guide, we returned to the same central defect location two weeks later (Fig. 3-9, compare two rightmost columns, arrows indicate identical features). At week six, additional mineral was deposited in the implant center indicated by a large increase in the second harmonic layer, indicative of collagen within mineral (Fig. 3-9, compare two rightmost columns). Furthermore, scaffold near the top surface was removed (Fig. 3-9, compare two leftmost columns, stars indicate identical locations), while deeper down, scaffold was retained in mineral. Vertical canals were visible within the second harmonic surface labeled with alizarin complexone (Fig. 3-9b, rightmost panel, white triangle). The colocalization of red mineral label to the second harmonic layer covering the scaffold confirms this tissue is indeed mineralized (Fig. 3-9b, two rightmost panels). From four to six weeks, donor cell density appeared reduced in two animals, while it remained similar in one animal. Bright Col3.6cyan host cells were observed on the mineral surface in the animal that retained moderate cell density. Taken together, these results indicate an increase in mineral deposition from four to six weeks and provide evidence of site-specific scaffold removal.

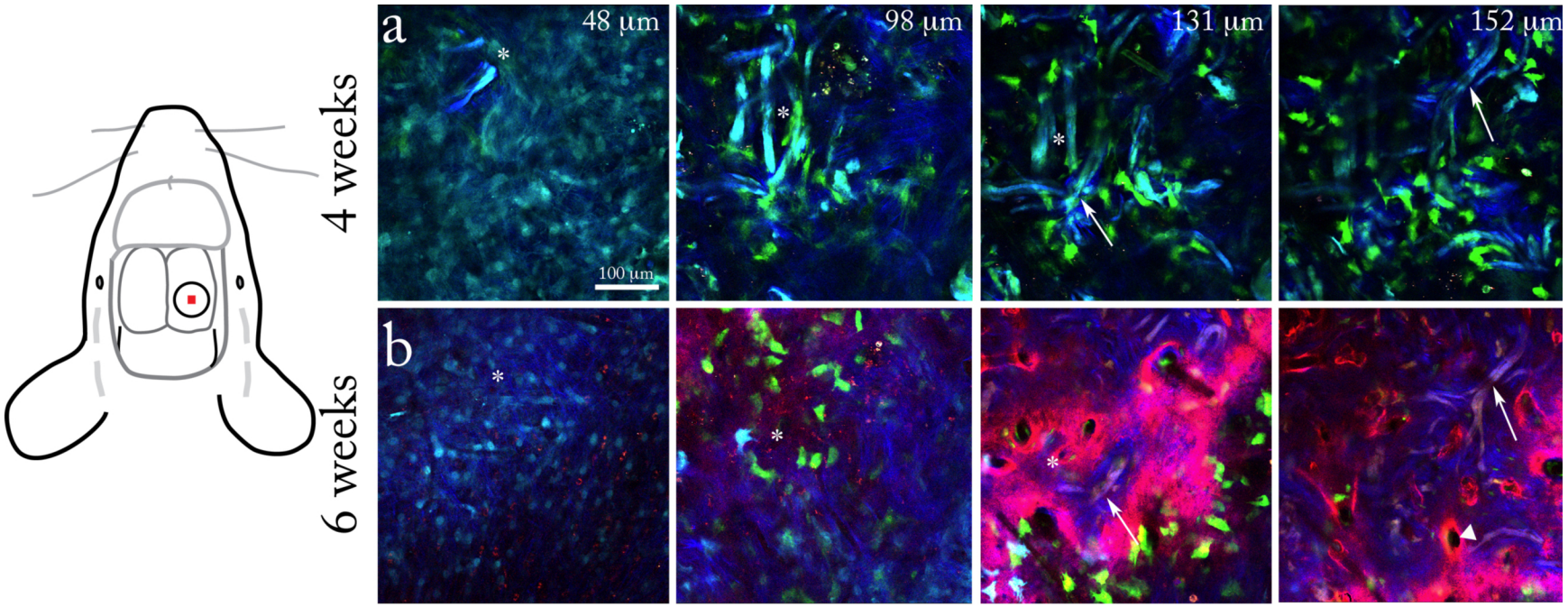


**Figure 3-9 | Mineral deposition and scaffold remodeling at week 6 post implantation.** Two z-stacks taken at an identical location in the middle of the defect at 4 (a) and 6 weeks (b). Diagram at left shows the location of the stack with respect to the defect (red square). Scaffold on the top surface was removed between 4 and 6 weeks post implantation (white stars indicate identical locations at 4 and 6 weeks). Deeper into the implant, the scaffold was retained (white arrows, slice 131 and 152 µm. A red mineralization label at 6 weeks (b) shows vertical channels in the matrix (white triangle, rightmost panel).

After imaging at week six, calvaria from both the imaged and control group (no imaging or surgery) were harvested, X-rayed, and cut into thin sections. By examining the X-ray micrographs, better integration of the implant with host bone was observed in the control group than the test group (Figs. 3-11a, b & c). However, by histomorphometry, the area fraction of bone that formed in the defect was similar between the two groups (Figs. 3-11d, e & f). The resultant bone formed a core-shell architecture. Hematopoietic cells were observed in the core region (Fig. 3-10), suggesting the marrow space was functional. Col3.6 osteoblasts were visible lining the inside and outside of the cortical shell (Figs. 3-11d & e). These data indicate that imaging surgery to expose the calvarium has a negative effect on host integration, but did not prohibit bone formation.

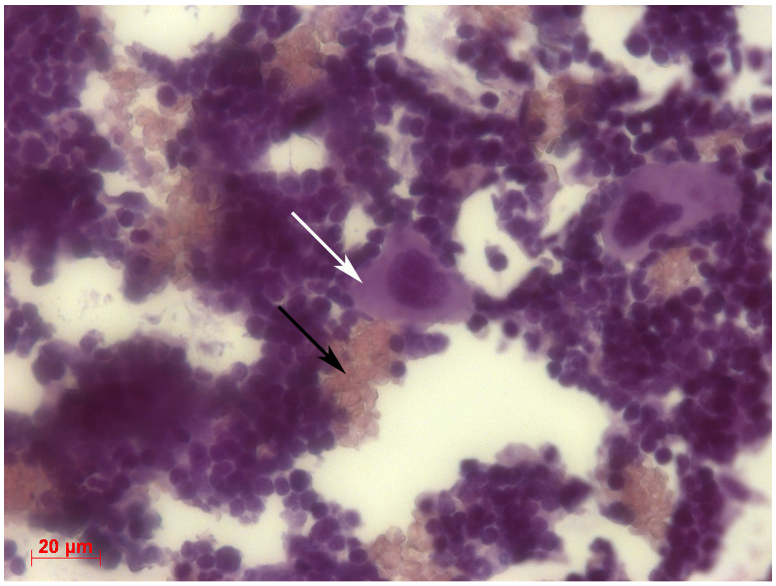


**Figure 3-10 | Bone marrow in implant is functional.** Megakaryocyte (white arrow) shedding RBCs (black arrow) in the bone marrow formed within the implant.

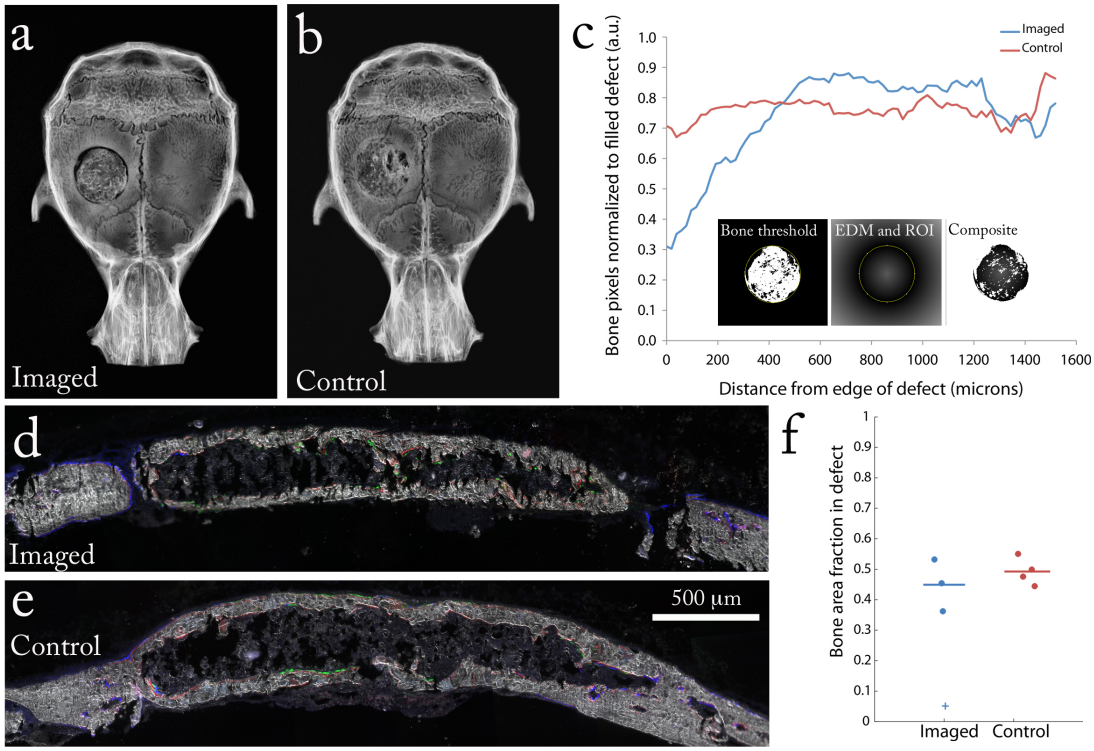


**Figure 3-11 | Imaging surgery affects host integration, but new bone formed is similar.** (a) X-ray of calvarium in imaged group and (b) control group. (c) Radiopacity as a function of distance from the edge of the defect for control and imaged group (n=3). (d) Histological section of defect from imaged group and (e) control group. Donor cells (green), host cells (blue) and mineral label (red). (f) Bone area fraction in the defect region. Horizontal lines indictate the mean value for each group. The plus sign represents the sample that did not form bone in the time preceding imaging and was therefore excluded from the calculation of the mean.

## 3.4 Discussion

2-photon microscopy combined with transgenic reporter animals has enabled researchers to observe, *in vivo,* the spatial and temporal dynamics of cell turnover during bone homeostasis and regeneration,[60] and single transplanted hematopoietic progenitor cells as they engraft in the bone marrow.[106,134] We have established a live-animal imaging model of tissue engineered bone using 2-photon microscopy and transgenic reporter animals. Using this approach, we examined host cells, donor cells, scaffold, and collagen matrix *in vivo* during a tissue-engineered repair. Following the implantation of a collagen-

hydroxyapatite scaffold seeded with bone marrow cells, we observed the *in vivo* outcome four and six weeks after implantation. New bone had formed on the surface of the scaffold primarily by donor-derived osteoblasts carrying the Col3.6topaz reporter at four weeks post implantation (Fig. 3-8d, panel 5). This indicates that a sufficient number of donor cells survived transplantation and went on to form a major contribution to osteogenesis in the repair site. This finding recapitulates Yu et al., who found transplanted Col3.6cyan calvarial osteoprogenitor cells survived and formed new bone in a calvarial defect filled with a collagen-hydroxyapatite scaffold.[89] Additionally, Cowan et al., using X-Y chromosome detection, found donor cells contributed 84-99% of new bone at 8 weeks following implantation.[64]

An important question in bone tissue engineering is how does the host contribute to repair? In the present study, an outer layer of host cells with fibroblastic morphology encapsulated the implant in collagen fibers. These cells were weakly expressing the Col3.6cyan reporter and may later contribute host osteoblasts to the implant. Host Col3.6cyan cells were found on the mineral layer surrounding the scaffold at both week four and six, albeit at a much lower incidence than donor Col3.6topaz cells. Park et al., using live animal 2-photon microscopy, found that Mx1 osteoprogenitor cells rapidly filled a calvarial microfracture (<1 mm diameter) and differentiated into osteoblasts at the bone edge.[60] In the present study, fibroblastic host cells stemmed from the periosteal surface of the host calvarium, seen by histological examination (data not shown). The periosteum is a well-known contributor to fracture repair of long bones.[148] Due to orientation of the imaging plane, 2-photon microscopy enabled unprecedented

observation of the new periosteal layer formed by the host above the cell-scaffold construct, likely by a similar osteoprogenitor population found by Park et al.

An increase in mineral deposition indicated by the second harmonic signal was observed between four and six weeks post-implantation. Additionally, it appeared that the scaffold near the top surface was resorbed (Fig. 3-9, 48 & 98 μm). This may be due to cell-mediated proteolytic degradation of type I collagen fibers in the scaffold by matrix metalloproteinases, namely MMP-1.[93,149] By contrast, scaffold deeper inside the implant was embedded in mineral and persisted for the duration of the experiment (Fig. 3-9, 131 & 152 μm). The mineral and cellular organization in the scaffold at week six is likely an intermediate stage before the bone is more fully remodeled. Thus, the embedded scaffold would only be removed after substantial remodeling of tissue-engineered bone. Yu et al. found that scaffold structure influences the structure of newly formed bone.[89] We found matrix being directly deposited on the scaffold structure until the pores were filled. Vertical channels were also noted in the new cortical layer produced at six weeks. These channels presumably link blood vessels from outside the implant to the implant core. Live animal microscopy enabled high-resolution examination of implant microenvironments at two time points, showing new mineral apposition and scaffold remodeling. This approach could provide new insights on how other scaffold materials are degraded and how mineral is deposited on scaffold surfaces.

Differences in cell organization and density were observed between host cells on the defect edge and donor cells on the mineral surface surrounding the scaffold. At the edge

of the host bone, Col3.6cyan host osteoblasts formed a dense layer of cells that formed bone inward towards the implant. In contrast, donor cell density on the scaffold surface appeared more moderate with disparate clusters of cells. Additionally, the mineral apposition rate appeared to be greater at the host edge than in the scaffold region. More robust measurement of mineral apposition is needed, however, this would suggest that tissue engineered bone formation is lagging behind host osteogenesis.

In the imaged group there was lower scaffold-host integration. This may be due to additional inflammatory signals introduced as a byproduct of the imaging surgery. However, the amount of bone in the defect area was similar (Fig. 3-11d,e,f), and bone continued to form beyond the four-week time point as shown by the increase of second harmonic signal in Fig 3-9 (two rightmost columns). This suggests that despite the imaging surgery, the processes essential to osteogenesis are preserved. Therefore, important questions that exist within the bounds of osteogenesis, regarding angiogenesis, scaffold degradation, cell signaling, proliferation and differentiation, may be addressed with this method. In combination with fluorescent reporters, any genetic entity of interest may be examined *in vivo* during bone formation in a cell-seeded construct. By enabling researchers to probe osteogenesis *in vivo*, 2-photon microscopy combined with fluorescent reporters should improve our understanding of the mechanisms that drive bone healing in a cell-scaffold construct.

In the future, new techniques and improved optics may enable imaging noninvasively through the skin. Recently, Tang et al. has enabled significant improvements in imaging

depth of multiphoton microscopy by active compensation and reduction of light scattering in thick heterogeneous tissue.[150] In their work, they imaged completely through a mouse skull to visualize fluorescent beads under the bottom surface. Although this method is currently limited to small fields of view (~10 μm), implementing image reconstruction algorithms should bring *in vivo* imaging to new depths within an arbitrarily large field of view. Additionally, the use of longer wavelength excitation (near infrared), corresponding to less light scattering, should also extend the maximum depth of 2-photon imaging systems. However this also depends on the development of probes capable of far-red excitation. Thus, future examination of cells in bone and bone defects may be performed noninvasively, eliminating imaging surgery and associated effects.

## 3.5 Conclusion

In summary, we have evaluated tissue-engineered bone *in vivo* at single cell resolution and *in situ* in three dimensions at two time points in the same animals. Using skeletal lineage reporters, we have described the tissue microenvironment preceding a repair study and enabled the connection between stereomicroscopy, histology, and 2-photon microscopy. In doing so we have also described the collagen organization in calvarial bone and marrow space. Lastly, we have revealed a window into the dynamic progression of a tissue-engineered construct *in vivo*, previously unseen. In this view we have made observations of donor cells, host cells, scaffold, and collagen organization in the repair site. Visualizing the cell and biomaterial interactions that govern the regeneration process *in vivo* should contribute to the development of tissue engineering therapies that efficiently utilize donor cells and cooperate with host response.

# 4 Bone tissue engineering with a collagen-hydroxyapatite scaffold and culture expanded bone marrow stromal cells

## 4.1 Introduction

Cell-based tissue engineering of bone has shown promising clinical[62] and preclinical[64,65] results, however, this approach is not yet well understood and faces several challenges before becoming a transformative clinical procedure. One such challenge is the delivery of progenitor cells in a supportive biomaterial that provides the microenvironmental cues for cell survival, vascular invasion, and bone formation. Additionally, the biomaterial scaffold must be degradable, leaving only new tissue behind when the repair is complete. Thus far, an ideal scaffold for bone tissue engineering has not been identified.[68]

Bone is primarily composed of hydroxyapatite [$Ca_{10}(PO_4)_6OH_2$] (~69% by weight) substituted with ions such as carbonate and magnesium.[6,7] Type I collagen forms ~90% of the organic fraction of bone, with the remaining ~10% being proteins such as osteonectin, fibronectin, and osteopontin, among many others.[6] Following a biomimetic design paradigm, we have developed a type I collagen-hydroxyapatite scaffold (herein termed Col-HA).[92] The type I collagen phase is easily degraded by cell-secreted collagenases, supports differentiation of progenitor cells into bone forming osteoblasts,[89,92] and contains unique binding motifs for the attachment of other ECM

molecules such as fibronectin[151]. Additionally, the degradation of collagen into gelatin may provide a means for cells to modulate the availability of RGD sites, normally hidden within the collagen triple helix.[152]

Several collagen-calcium phosphate materials are currently FDA-approved for use with bone marrow extract as a bone void filler, such as Healos® (Depuy), Collagraft® (Zimmer), Ossimend® (Collagen Matrix), and Mozaik® (Integra LifeSciences). However, osteoprogenitors represent only a very small fraction of the bone marrow population,[37] and it has been found previously that the number of progenitors strongly influences osteogenesis *in vivo*.[153] One study has indicated that fresh bone marrow combined with a coral scaffold did not form bone when implanted in a ovine segmental defect, whereas culture-expanded bone marrow stromal cells (BMSCs), seeded to the same material, did form new bone.[65] Thus culture expansion, which greatly increases the number of osteoprogenitors, is a likely requirement for successful cell-based bone tissue engineering. Currently, there is no clinical precedent for the use of commercial collagen-HA scaffolds with culture-expanded osteoprogenitors.

Commercial scaffolds are useful for the development of cell-based therapies for bone tissue engineering, due to their sterility, use-history, and consistency. However design modifications by the researcher are generally out of reach. Additionally, in order to understand how scaffold properties influence cell-based outcomes it would be of benefit to the researcher to have full control over scaffold properties. This would ultimately allow for a deeper understanding of cell-scaffold interactions, ultimately leading to

optimal scaffold design and contributing to the long-term goal of safe and efficient cell-based therapies in the clinic.

The goals of this work were to (i) fabricate a sterile collagen-HA scaffold (ii) evaluate cell attachment, viability, and progenitor number in the scaffold just prior to implantation, (iii) achieve consistent osteogenesis *in vivo* with the Col-HA scaffold combined with culture-expanded BMSCs, and (iv) compare the level of early bone formation in the Col-HA scaffold to an established commercial collagen-HA biomaterial. The Col-HA scaffold presented here supports robust osteogenesis and is fully defined, open, and modifiable. This platform is ideal for basic research and facilitates the development of collagen-hydroxyapatite biomaterials for bone tissue engineering.

## 4.2 Materials & Methods

### 4.2.1 Scaffold fabrication by collagen-hydroxyapatite co-precipitation and freeze casting

The main component of the scaffold, type I collagen, was derived from rat tail tendons following Rajan et al.[154] Collagen fibers and HA nanoparticles were formed simultaneously by precipitation in a modified simulated body fluid (mSBF) solution.[91] Briefly, the collagen solution was adjusted to 2.5 mg/mL by a two-fold dilution in sterile ultrapure water at 4 °C. For a 200 mL solution of mSBF, the following salts were added in the order they appear: 1.08 g NaCl, 0.1428 g $K_2PO_4$, 0.0622 g $MgCl_2$, 2.4 g HEPES, 0.1758 g $CaCl_2$, and 0.294 g $NaHCO_3$. While kept cold, the pH of the solution was adjusted to 7.0 with sodium hydroxide solution and then transferred to a water bath at 40 °C for 24 hours to allow *in situ* co-precipitation. The gel-precipitate was centrifuged at

11,000 g and 4 °C for 12 min. The supernatant was discarded and the pellet was freeze dried (Labconco). The collagen-HA precipitate was reconstituted with water at a concentration of 100 mg/mL, briefly homogenized to obtain a uniform slurry, and placed in a polystyrene culture dish. To impart a porous structure, the sample was freeze-dried starting from room temperature to -40 °C at a cooling rate of -0.37 °C/min. The dried scaffold was immersed in a solution of 20 mg/mL EDC [1-ethyl-3-(3-dimethylaminopropyl) carbodiimide hydrochloride] for 24 hours at 4 °C to covalently crosslink the collagen fibers. The scaffold was then rinsed in a solution of 5% (w/w) glycine in sterile water overnight to block unreacted EDC, followed by three sequential rinses in sterile water for 15 minutes each at 4 °C. Finally, rinsed scaffolds were freeze-dried again, cut to a thickness of ~500 μm with a milling machine and punched to a diameter of 3.5 mm.

Healos® is composed of bovine type I collagen fibers mineralized with a thin coating of calcium phosphate, and formed into a high porosity sponge containing 4-200 μm pores. This material was received sterile. In house scaffolds were terminally sterilized with a 24-hour exposure to ethylene oxide gas using a bench-top sterilizer (Anprolene AN74i, Anderson Products), followed by a 24-hour purge of excess gas in a vented hood. Before implantation, sterility of Col-HA scaffolds was assessed by incubating sterilized and unsterilized scaffolds, a negative control, in Tryptic Soy Broth (Sigma) at 40 °C for 2 weeks. The sterility of the scaffold was confirmed by the absence of bacterial growth in vials containing ethylene oxide sterilized scaffolds under these culture conditions.

### 4.2.2 Characterization of collagen-hydroxyapatite scaffold

The ratio of inorganic (HA) to organic (collagen) content was determined by thermogravimetric analysis (TGA Q-500, TA Instruments). The inorganic material was examined by X-ray diffraction (D2 Phaser, Bruker) performed on the resultant powder from a proteinase-K (Invitrogen) digestion of the scaffold. Diffraction peaks were acquired from a 2Θ of 10° to 90° at a scan speed of 2.4 °/min.

Infrared absorbance spectra from 4000 to 400 $cm^{-1}$ was acquired at a resolution of 4 $cm^{-1}$ over 32 scans (Magna 560, Nicolet). Spectra were then analyzed with KnowItAll V9.5 software (BioRad).

Electron micrographs were acquired with a field emission scanning electron microscope (JSM-6335F, JEOL). Prior to imaging, Col-HA scaffolds were sputter-coated (Polaron E5100) with a thin layer of gold-palladium.

To enable examination of scaffolds with X-ray tomography, scaffolds were stained with 1% iodine in ethanol overnight to enhance radiopacity.[155] 1500 images were acquired at an angle of -103˚ to 103˚ with an exposure time of 4 s, source power of 8 W, a voltage of 55 kV, and a 20x objective (MicroXCT-400, Xradia). Tomography images were reconstructed with XM Reconstructor (Xradia) and viewed with the 3D viewer plugin for the FIJI distribution of NIH ImageJ.[142]

Scaffold porosity, wall thickness, and anisotropy were calculated from tomography data from dry scaffolds with the BoneJ plugin for FIJI.[156] Since very small pore interconnects may result in a near 100% interconnectivity, but have minimal contribution to mass transport, we excluded pores with a size less than 15 microns from the interconnectivity measurement. This was accomplished by performing a sphere-filling algorithm (thickness, BoneJ)[156] to the void volume. A threshold was then performed to select the fraction of the void volume with a caliber from 0-15 μm. This was added to the original solid structure to fill the small holes (≤15 μm) in the scaffold walls. Finally, the interconnectivity (connected void volume/total void volume) was calculated using the 3D objects counter[157] applied to the void volume. The largest object was used as the interconnected volume.

Scaffold pore size was determined from histological sections of the scaffold using the mean linear intercept method.[158] Briefly, transverse sections of scaffolds were obtained by cryosectioning (CM3050 S Cryostat, Leica) and imaged with darkfield optics (Axio Scan.Z1, Zeiss). Image processing was performed with ImageJ. Four sections were analyzed by drawing four lines regions of interest (ROIs) at different orientations for each section. The mean pore size was calculated as an average of the pore lengths falling on the line ROIs.

Scaffold permeability, k ($m^4$/Ns), was measured with water and a custom flow cell using the following equation found in reference [159]:

$$k = \frac{\Delta x}{A \cdot M_{B2}} \cdot \frac{2\pi^2 r^4}{(M_{B1}/M_{B2})^2 - 1}$$

where, $\Delta x$ = scaffold length (m), A = scaffold cross-sectional area ($m^2$), $M_{B1}$ = mass flow rate without scaffold (g/s), $M_{B2}$ = mass flow rate with scaffold (g/s), and r = radius of the outlet (m).

### 4.2.3 *In vitro* cell culture with primary mouse osteoprogenitors

Mouse BMSCs were isolated from the femur and tibia of CD1 wild type animals. Cells were added to 100 mm culture dishes in α-MEM (Gibco) containing 10% fetal bovine serum and 1% penicillin-streptomycin. Following isolation, cells were allowed to attach to the culture dish in a humidified incubator at 5% $CO_2$, ambient $O_2$ and 37 ˚C. To allow hematopoietic cells to contribute to early colony formation by osteoprogenitors, the culture medium was changed four days after seeding the bone marrow pellet. After six days of incubation, cells were trypzined and seeded dropwise onto the top of either the Col-HA scaffold or a bovine collagen-hydroxyapatite scaffold (Healos®, Depuy) at a density of $1.0x10^6$ cells in 15 μL of culture medium to immerse the scaffold. After seeding, cells were allowed to settle for 30 minutes before an additional 1 mL of culture medium was added to the culture well. Cell permeation and attachment were assessed at one minute, one hour, and 12 hours after seeding. Cell-seeded constructs were also incubated for a one-week period to evaluate cell attachment, distribution, and to check for dramatic scaffold degradation associated with the sterilization method.

Following *in vitro* incubation, scaffolds were fixed in 10% formalin and stained for F-actin (Rhodamine-Phalloidin, Invitrogen) and nuclear DNA (Hoescht, Invitrogen). Cell viability and progenitor status was examined after one and five days of *in vitro* incubation.

Viability was assessed using calcein and ethidium homodimer-1 provided as a kit (Live/Dead, Invitrogen). Osteoprogenitor cells were labeled using the α-SMAAmCherry fluorescent reporter. This reporter marks a population of multipotent cells and consists of a transgene containing the mCherry fluorescent protein driven by the smooth muscle alpha actin (α-SMA) promoter. [41]

To enable viewing of the scaffold cross-section, the scaffold was cut in half and glued to the bottom of a culture well, with the cross-section facing up. The cross-section of the scaffold was scanned in three-dimensions to a depth of 100 μm with a 2-photon microscope (Ultima IV, Prairie technologies). Several tiles were stitched together to form a high-resolution (20x objective) wide field view. Second harmonic images were acquired at an excitation wavelength of 900 nm and data was collected at 450 nm, corresponding to the frequency doubling of the excitation wavelength as it interacts with the noncentrosymmetric structure of the collagen triple helix.[113]

### 4.2.4 Image processing and analysis of *in vitro* data

Cell distribution from the outside edge was assessed by a distance analysis.[106] The cell seeding efficiency (CSE), defined as the number of cells in the scaffold divided by the total number of cells seeded, was calculated using the 3D particle counter to identify and count cell nuclei in 3D stacks of seeded scaffolds.

### 4.2.5 *In vivo* bone formation in a mouse calvarial defect

Two groups (n=5) of NOD.Cg-*Prkdc*$^{scid}$ *Il2rg*$^{tm1Wjl}$/SzJ (NSG) immunodeficient mice were used as hosts. One day after scaffold seeding, host mice were anesthetized with a ketamine (135 mg/kg) – xylazine (15 mg/kg) blend and a 3.5 mm diameter critical size defect was created in the right parietal lobe using a bur trephine (RAL #229-030, Benco Dental). Extreme care was taken to prevent damage to the dura mater beneath the calvarium. Animals were given postoperative analgesic (bupronephrine, 0.08 mg/kg). At three weeks post-implantation, animals were sacrificed for X-ray and histological analysis. To mark areas of active mineralization, calcein and alizarin complexone labels were injected intraperitoneally at two and three weeks, respectively.

In order to track cell fate after transplantation, donor cells were derived from bone marrow from CD1 animals carrying a Col3.6Cyan reporter gene. The reporter consists of the cyan fluorescent protein driven by a type I collagen promoter region that is activated in osteoblasts.[43] The bone marrow was flushed with a 27-gauge needle from the femur and tibia of CD1 Col3.6Cyan animals and plated in α-MEM (Gibco) containing 10% FBS and 1% penicillin-streptomycin, incubated at 37 ˚C, 5% $CO_2$, and ambient $O_2$. After 6 days, adherent cells were removed with 0.25% trypsin-EDTA (Gibco). One million cells in 15 µL of culture medium were seeded dropwise to each dry Col-HA and Healos® (Depuy) scaffold. After seeding, cells were allowed to settle for 30 minutes before one mL of culture medium was added. Cells were incubated with scaffolds overnight to ensure full cell attachment to the scaffold surface. All procedures in this study were approved by the UConn Health Center Institutional Animal Care and Use Committee (IACUC).

### 4.2.6 Histomorphometric analysis of *in vivo* data

To quantify the bone area fraction and donor cell area fraction for the test and control group, a region of interest (ROI) outlining the defect area was manually drawn on radiographs and histological sections. A threshold was then applied to the images to demarcate areas of bone.

To evaluate the edge integration of the constructs from radiographs, a line ROI was manually drawn along the perimeter of the implant, but inside the defect area. The line ROI contains the peripheral regions of the implant that were contacting host bone. If the implant was connected to the host bone, this would appear as a bone pixel in the line ROI placed between the construct and the edge of the host bone. To find the fraction of the host bone perimeter that was connected to the implant by bone, the number of bone pixels was divided by the total number of pixels in the line region.

Donor cell colocalization with the mineral label was determined using the distance analysis mentioned in the *in vitro* image analysis section. To exclude donor cells not associated with the label surface, a cutoff value of 14 μm was applied, corresponding to the mean distance from the edge of the label surface to the far edge of a donor cell on the label surface.

### 4.2.7 Statistical analysis

A t-test was used to determine statistical significance ($p<0.05$) between the Col-HA and Healos® groups (n=5).

## 4.3 Results

### 4.3.1 Characterization of the collagen-hydroxyapatite scaffold

Following freeze casting, the scaffold contained 15.36% water, 60.94% collagen, and 23.70% HA by thermogravimetric analysis (Fig. 4-1). The identity of the inorganic phase was confirmed as HA by analysis of the XRD pattern of the resultant powder following proteinase-K digestion of the collagen-HA composite (Fig. 4-2f). The XRD pattern was indicative of a poorly crystalline HA with broad peaks, namely at a 2Θ of 25.9˚ and 31.8˚ corresponding to the (002) plane, and overlap of the (211), (112), and (300) planes of HA, respectively.

FT-IR absorbance spectra of the digested scaffold sample further indicated that the inorganic phase is a carbonated HA, sharing similarities with the absorbance spectra of hydroxyapatite from dentin (Fig. 4-2g). Phosphate vibrational bands were observed at 961 (ν1), 475 (ν1), 1046 (ν3), 603 (ν4), and 567 (ν4) $cm^{-1}$.[160] Carbonate vibrational bands were observed at 873 (ν2) and 1400-1580 (ν3) $cm^{-1}$.[161] Amide I and Amide B bands from residual collagen in the sample were detected at 1653 and 2923 $cm^{-1}$, respectively.[161] Taken together, these results indicate the inorganic phase of the scaffold is a poorly crystalline carbonated hydroxyapatite similar to that found in native bone.

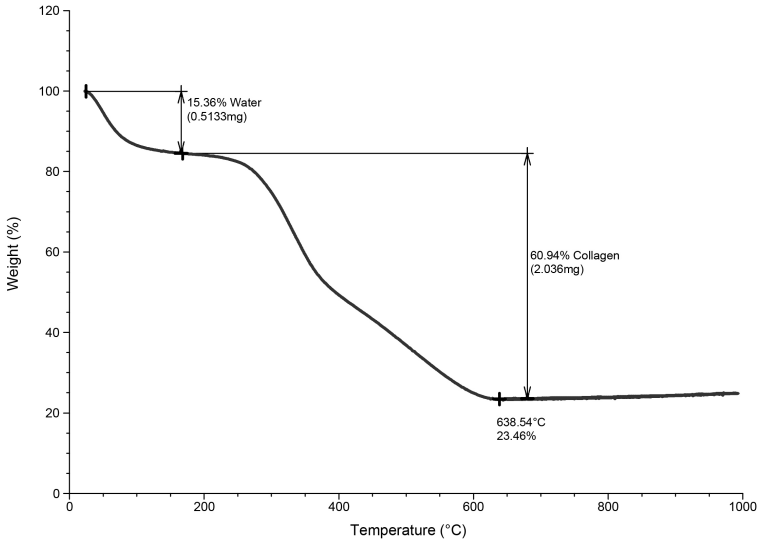


**Figure 4-1 | Thermogravimetric analysis of collagen-HA scaffold.**

The collagenous phase of the scaffold produced a strong second harmonic signal when examined with 2-photon microscopy (Fig 4-2h-j). Since the second harmonic signal from collagen is due to the repeating noncentrosymmetric structure of the triple helical protein,[113] this indicates the scaffold contains collagen in a triple helical conformation rather than a denatured conformation (gelatin) which does not produce a second harmonic signal.[120]

The scaffold microstructure has a cellular organization with sheet-like walls (Fig 4-2a, 4-2c, 4-2d). Near the nanoscale, the scaffold structure consists of agglomerated HA nanoparticles interspersed within collagen fibers (Fig. 4-2b). By X-ray microtomography, the porosity of the scaffold was found to be 93% (Table 2). The mean pore size was 101±71 μm, with a scaffold wall thickness of 5.5±2.4 μm (Fig. 4-2d). Pore alignment was largely isotropic with an anisotropy value of 0.3 (one being a perfectly aligned structure and zero being random). The scaffold permeability and degree of interconnectivity was

$1.68\times10^{-10}$ $m^4$/Ns and 99%, respectively (Table 2). This scaffold architecture and composition should be supportive of cell infiltration, attachment, and osteogenesis.

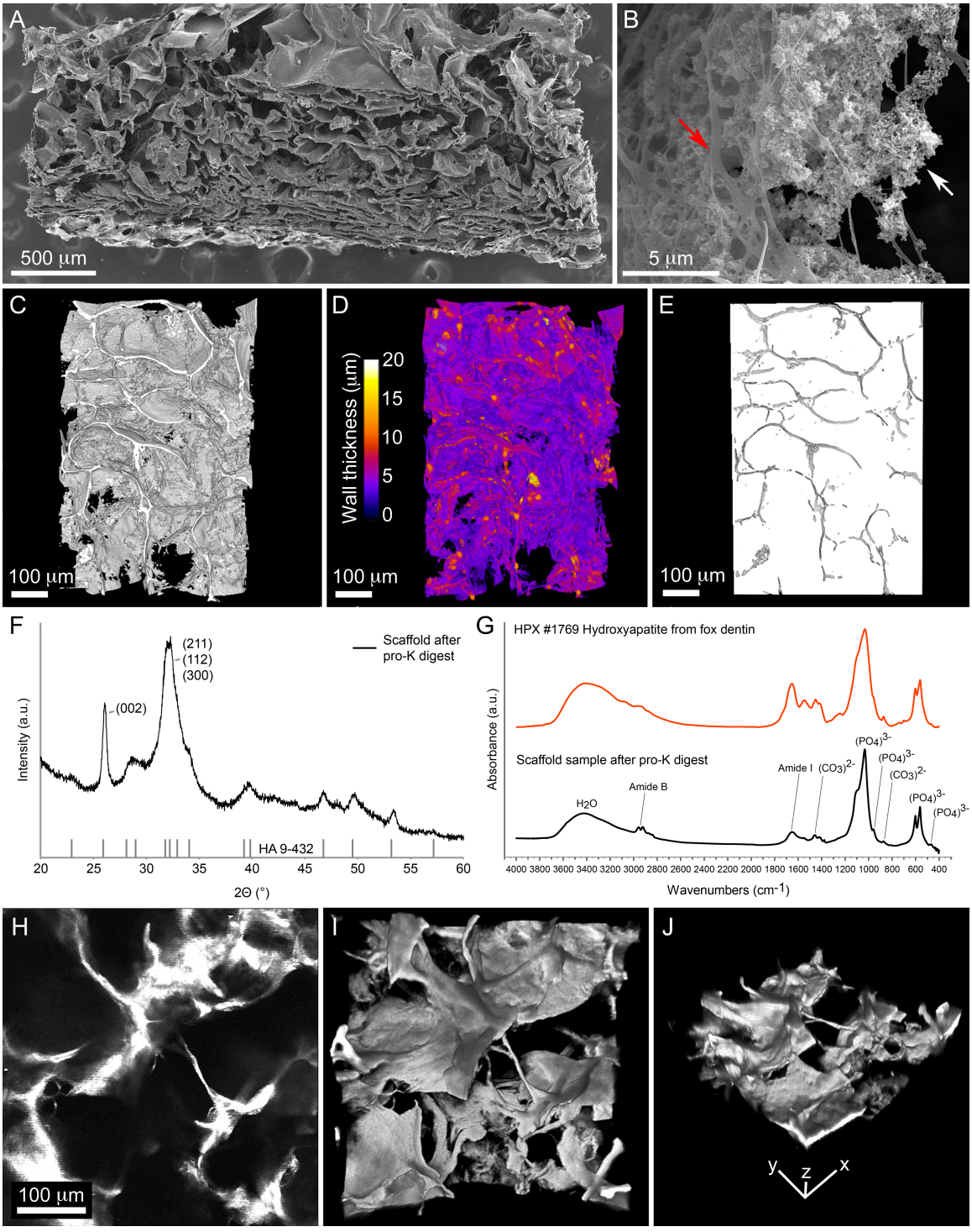


**Figure 4-2 | Characterization of Col-HA scaffold.** (A) Electron micrograph of a Col-HA scaffold cut in cross section. (B) Magnification of hydroxyapatite nanoparticles (white arrow) interspersed with collagen fibers (red arrow). (C) 3D reconstruction of the scaffold acquired by X-ray microtomography. (D) 3D reconstruction of the scaffold color-coded to indicate wall thickness. (E) Scaffold pore volume in 3D acquired by X-ray microtomography. (F) X-ray diffraction pattern of the inorganic phase of the scaffold

compared with a hydroxyapatite reference (vertical bars). (G) Infrared absorbance spectra of the inorganic phase of the scaffold (black line) compared with a hydroxyapatite reference spectra (red line). (H) A single slice of a 3D stack of images representing the collagen-HA scaffold imaged by its second harmonic signal. (I) Top and (J) isometric view of a 3D reconstruction of the collagen-HA scaffold viewed with second harmonic microscopy.

| Sample | Porosity (%) | Pore size (μm) | Wall thickness (μm) | Interconnectivity (%) | Permeability ($m^4$/Ns) | Anisotropy |
|---|---|---|---|---|---|---|
| Col-HA | 93 | 101±71 | 5.5±2.4 | 99 | $1.68\times10^{-10}$ | 0.3 |

**Table 2 | Scaffold architectural properties.** The interconnectivity is defined as the connected void volume divided by the total void volume. The value of the anisotropy parameter tends toward zero for randomly oriented structures and to one for parallel flat plates.

### 4.3.2 Cell seeding and attachment to collagen-hydroxyapatite scaffolds

To evaluate the time required for culture-expanded mouse BMSCs to attach to the scaffold, cells were seeded to Col-HA scaffolds and Healos®. Subsequently, scaffolds were harvested at one minute, one hour, and 12 hours after seeding. It was found that cells were well-attached after 12 hours of *in vitro* culture, but not within one hour or, not surprisingly, within one minute (Fig. 4-3a-f). The one-minute condition represents the initial conditions at the time of implantation when cells are seeded to a scaffold and immediately implanted.

Cells were present throughout the thickness of both scaffolds at all time points, indicating cells were able to penetrate through interconnections in the void volume (Fig. 4-3a-f). However, cell density decreased with increasing distance from the outer surface of the scaffold (Fig. 4-3g). The cell seeding efficiency was found to be ~10% when the initial seeding number was one million cells. This corresponds to about 100,000 cells seeded to a scaffold, prepared in the geometry of a 3.5 mm diameter mouse critical-size

calvarial defect. Furthermore, large clumps of cells on top of the scaffold were observed at one minute and one hour after seeding (Fig. 4-3a,b, & Fig. 4-4). In a separate experiment, these clumps were not present after a few weeks of implantation,[162] suggesting that these cells do not survive after implantation. Similarly, cell clumping on the loading side of the scaffold was not observed after 12 hours of *in vitro* culture, indicating that unattached or poorly attached cells may not survive beyond a few hours. These results indicate that a 12-hour incubation time is sufficient for culture-expanded mouse BMSCs to fully attach to the scaffold. To ensure cell attachment before implantation, a 12-hour incubation period was used in all experiments described hereafter.

Sterilizing protein-based biomaterials is challenging due to the potential for material damage as a result of the sterilization process. Immersion in 70% ethanol is not a robust sterilization method, since hydrophilic virus and bacterial spores are resistant to this method.[163] Previously, we observed rapid degradation of our scaffolds (< one week) when sterilized with gamma irradiation and cultured with mouse BMSCs (data not shown). Herein, ethylene oxide gas was employed to sterilize Col-HA scaffolds. Sterility was confirmed by the absence of bacterial growth after two weeks in bacterial culture medium at 40 °C.

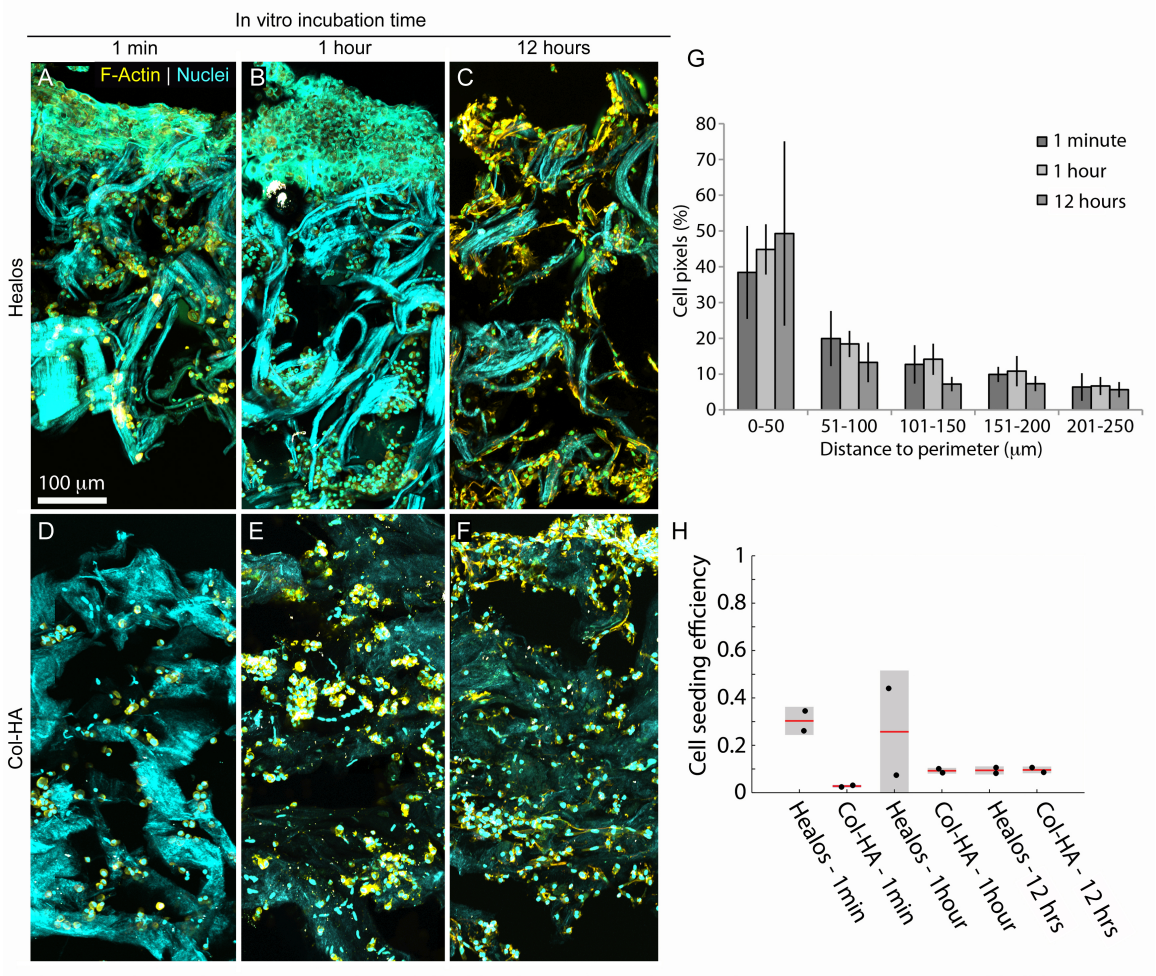


**Figure 4-3 | In vitro characterization with mouse BMSCs.** Maximum intensity projections of scaffolds cut in half and imaged in 3D normal to the cross-section. Healos scaffold after (A) one minute, (B) one hour and (C) 12 hours of incubation with mouse BMSCs. Col-HA scaffold after (D) one minute, (E) one hour and (F) 12 hours of incubation with mouse BMSCs. The collagen content generates a second harmonic signal (cyan). Cells were stained for F-actin (yellow) and nuclei (punctate cyan signal). (G) Quantification of cell distribution relative to the outside edge. (H) Cell seeding efficiency at one minute, one hour, and 12 hours of incubation after seeding (initial seeding density was 1 million cells/scaffold, approximately 3.5 mm in diameter and 500 μm thick).

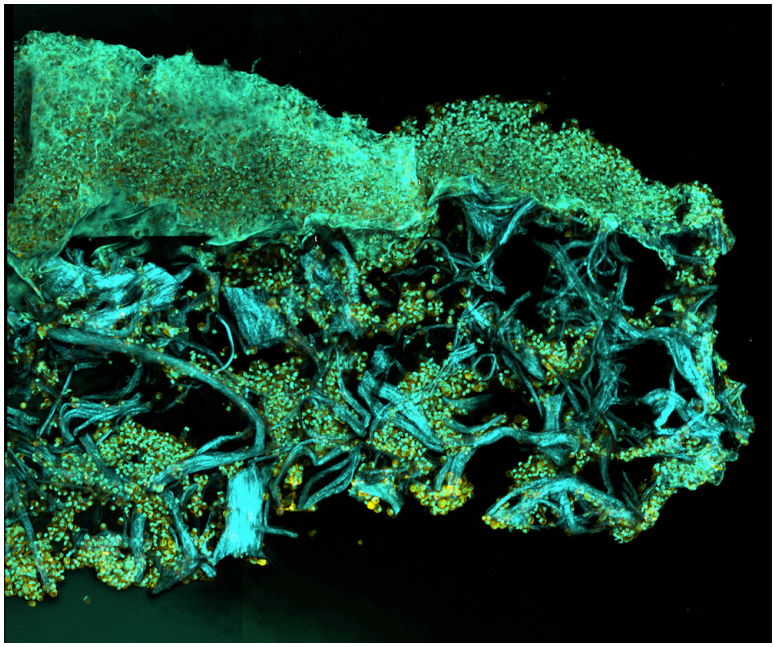

**Figure 4-4 | Cell clumping on scaffold. Maximum intensity projection of a 2-photon stack acquired in a cross-sectional view of a Healos® scaffold**. Cells are stained for F-actin (yellow), nuclei (cyan) and the scaffold produces a second harmonic signal (blue).

To determine if the sterilization procedure had a negative effect on scaffold degradation, as observed with irradiation sterilization, scaffolds were cut into disks and seeded with culture-expanded mouse BMSCs and incubated for one week. In contrast to gamma irradiation (data not shown), ethylene oxide sterilized scaffolds did not exhibit rapid degradation when cultured with cells for one week (Fig. 4-5). The Col-HA scaffolds maintained their original circularity, while the Healos® control group expanded anisotropically upon hydration (Fig. 4-5a-d). When stained for F-actin filaments after 1 week *in vitro*, cells were well attached to the scaffold surface and distributed throughout the thickness (Fig. 4-5e-g). These results suggest ethylene oxide is a suitable method for producing sterile collagen-hydroxyapatite scaffolds without resulting in rapid degradation (<1 week *in vitro*) and maintaining good cell attachment to the biomaterial.

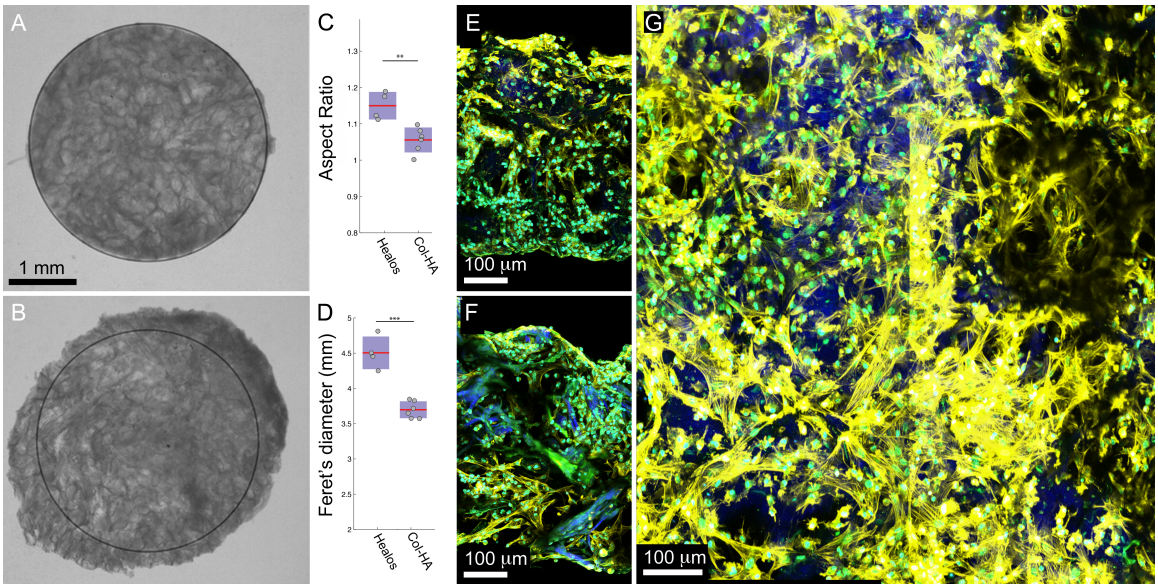


**Figure 4-5 | Sterilized scaffolds seeded with mouse BMSCs after one week in vitro.** (A) Ethylene oxide gas-sterilized Col-HA scaffold, and (B) Healos® after one week in vitro with mouse BMSCs. Quantification of the (C) aspect ratio (long axis/short axis) and (D) longest diameter (Feret's diameter) Col-HA and Healos® scaffolds after 1 week in vitro. Maximum intensity projection of (E) a Col-HA and (F) a Healos® scaffold seeded with mouse BMSCs cut in cross-section after one week in vitro. (G) Maximum intensity projection of a 2-photon stack acquired from a top view of a Col-HA scaffold. Cells (E)-(G) are stained for F-actin (yellow), nuclei (cyan), and the scaffold produces a second harmonic signal (blue).

Previous work has indicated that the BMSCs from the donor population are predominantly responsible for bone formation in the calvarial model.[64,89,162] This observation underscores the need for a viable progenitor population within the seeded scaffold to achieve consistent osteogenesis. Here, we examined the cell viability and the distribution of osteoprogenitor cells at one and five days after seeding Col-HA scaffolds. At day one, the majority of cells were viable, however, cells were not uniformly distributed in the radial direction of the scaffold (Fig. 4-6a). By contrast, at day five, cells were well distributed throughout the scaffold (Fig. 4-6b), highlighting the ability of cells to migrate into available space. Upon closer inspection with 2-photon microscopy, a subset of smaller diameter nonviable cells was found within the scaffold walls (Fig. 4-6e).

To examine cell viability throughout the thickness of the scaffold, samples were cut in half and viewed in cross-section. Cells appeared predominantly viable throughout the scaffold thickness five days after seeding (Fig 4-6f), suggesting that strictly diffusive transport in the relatively thin scaffold is sufficient to support cell viability over this period. Similarly, when cells containing a fluorescent marker for osteoprogenitor cells, α-SMAAmCherry[41], were seeded to Col-HA scaffolds, they were not homogenously distributed by day one (Fig. 4-6c), but were homogenously distributed by day five after seeding (Fig. 4-6d). Taken together, these results suggest that at one day after seeding, representing the initial conditions at the time of implantation used here, cells were well attached to the scaffold, viable, and the population contained large numbers of osteoprogenitors.

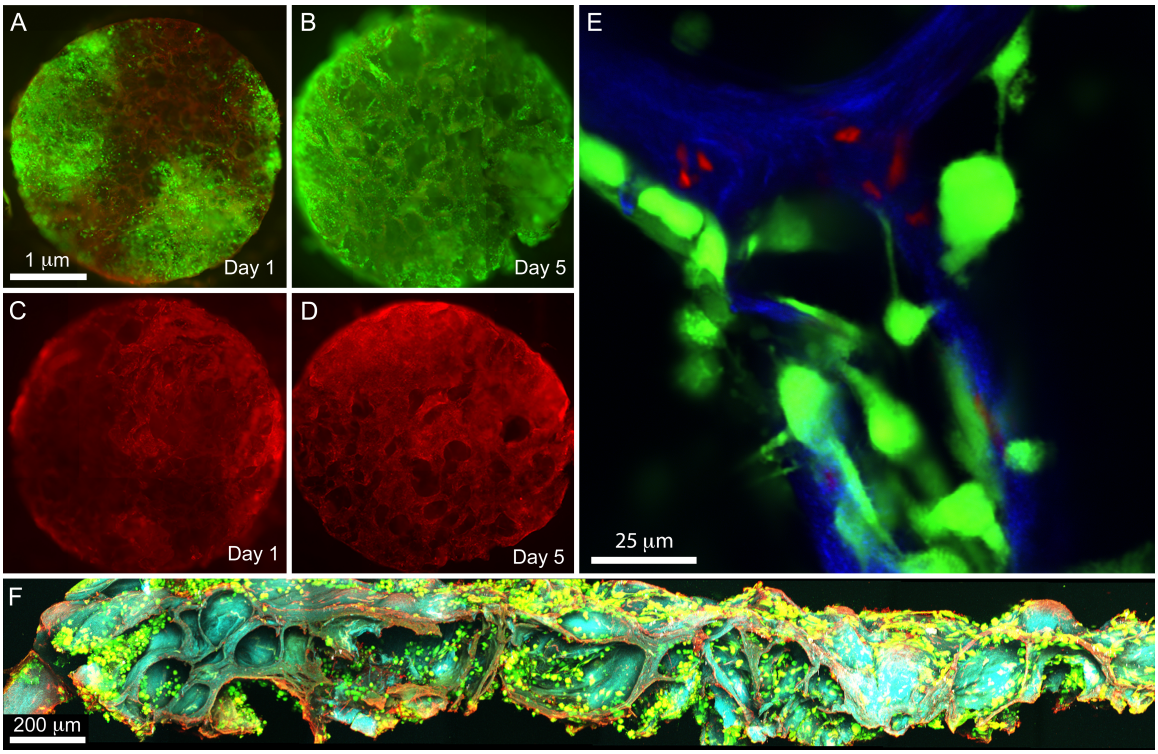


**Figure 4-6 | Cell viability and progenitor status.** Col-HA scaffolds seeded with culture expanded mouse BMSCs and incubated for (A) one and (B) five days in vitro. Scaffolds were stained for live (green) and dead (red) cells. (A slight red background is visible, due to scaffold adsorbance of the dead stain). Col-HA scaffolds seeded with culture expanded mouse BMSCs carrying a SMAAmCherry (red) reporter for osteoprogenitor cells and incubated for (C) one and (D) five days in vitro. (E) Single image of a 2-photon micrograph showing live (green) overlying the scaffold (blue) and smaller dead (red) cells that have invaded the scaffold walls after one day in vitro. (F) Maximum intensity projection of a 3D stack of the scaffold containing cells stained for live (green) and dead (red) viewed in cross section after five days in vitro.

### 4.3.3 *In vivo* calvarial defect model of bone repair

Three weeks after implantation, calvaria containing critical size defects filled with BMSCs combined with either the Col-HA scaffold or Healos® were harvested. Viewed with a stereomicroscope (Fig. 4-7), the implant regions were more opaque than the surrounding host bone. All samples contained bone by radiographic discrimination and several implants appeared well integrated to the host bone (Fig. 4-8a through 4-8d, and 4-

8g through 4-8i). Two samples were not well connected to the host bone (Fig. 4-8f, 4-8h, orange arrows) and two others exhibited significant gaps between the implant and host (Fig. 4-8e, 4-8j, orange arrows). Some implants appeared to overlap the edge of the host bone rather than filling the defect (Fig. 4-8e, 4-8g, 4-8h, 4-8i, blue arrows). Since all scaffolds were placed in the defect at the time of implantation, this would require the edge of the scaffold to pop out some time after.

Mineralized tissue was observed between the red and green mineralization labels, given at two and three weeks respectively (Fig. 4-8k, 4-8l, 4-8o, 4-8p), indicating that new bone had formed as opposed to mistaking the calcium phosphate phase of the scaffold for new bone. Donor cells carrying the Col3.6Cyan[43] osteoblast reporter gene were found lining the active mineralizing surface labeled with alizarin red (Fig. 4-8l, 4-8p). Furthermore, 75±0.10% and 67±0.05% of the mineral label was lined with donor cells for Healos® and Col-HA respectively, (Fig. 4-9) suggesting that the donor source played a dominant role in early bone formation (<3 weeks). Taken together, these results indicate that all samples contained mineralized tissue deposited primarily by donor cells and that some of the samples appeared to have degraded.

The mean bone area fraction (AF) from radiographs was slightly higher for the Col-HA group compared to the Healos group, however this difference was not significant (Fig. 5s). In cross-section, the mean bone AF was similar between the groups (Fig. 4-8t). The Col-HA scaffolds, when viewed from the top, were slightly more integrated with host than the Healos® group, however, this result ($p$=0.077) was not significant (Fig. 4-8u).

When the mean AF of donor cells in the defects viewed in cross-section was compared, the Healos® group was slightly higher, although this difference was not significant (Fig. 4-8v). The in-group standard deviation for each of the four parameters investigated was smaller for the Col-HA group compared with the Healos® group (Fig. 4-8s through 4-8v, blue bars indicate one standard deviation). Taken together, these results indicate the Col-HA group exhibited consistent bone formation and appeared well attached to the host in four out of five samples. When compared to Healos®, the Col-HA scaffold performed favorably, providing evidence for the efficacy of the Col-HA scaffold for cell-based bone repair.

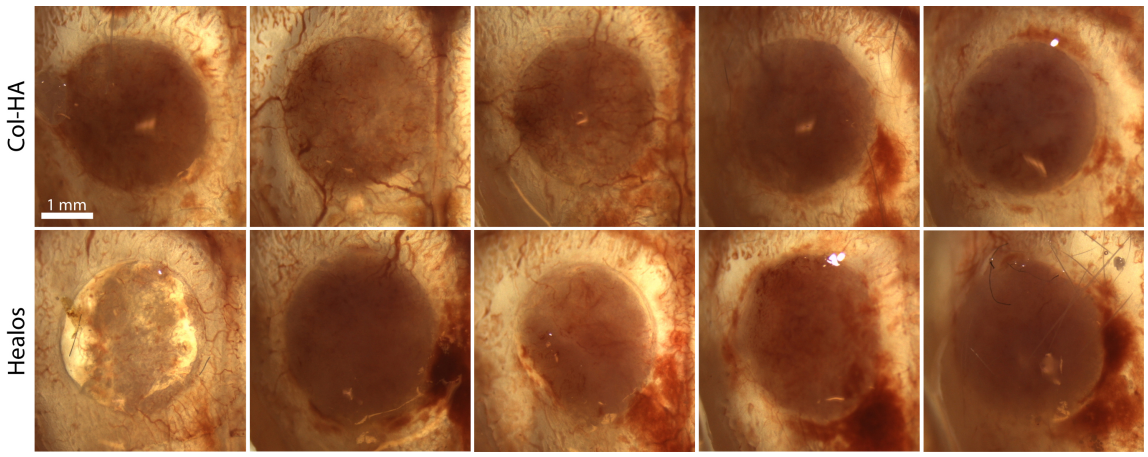


**Figure 4-7 | Stereomicroscopy of scaffolds after 3 weeks of implantation in mouse critical size calvarial defects.** Presented in the same arrangement as the radiographs shown in Fig. 5.

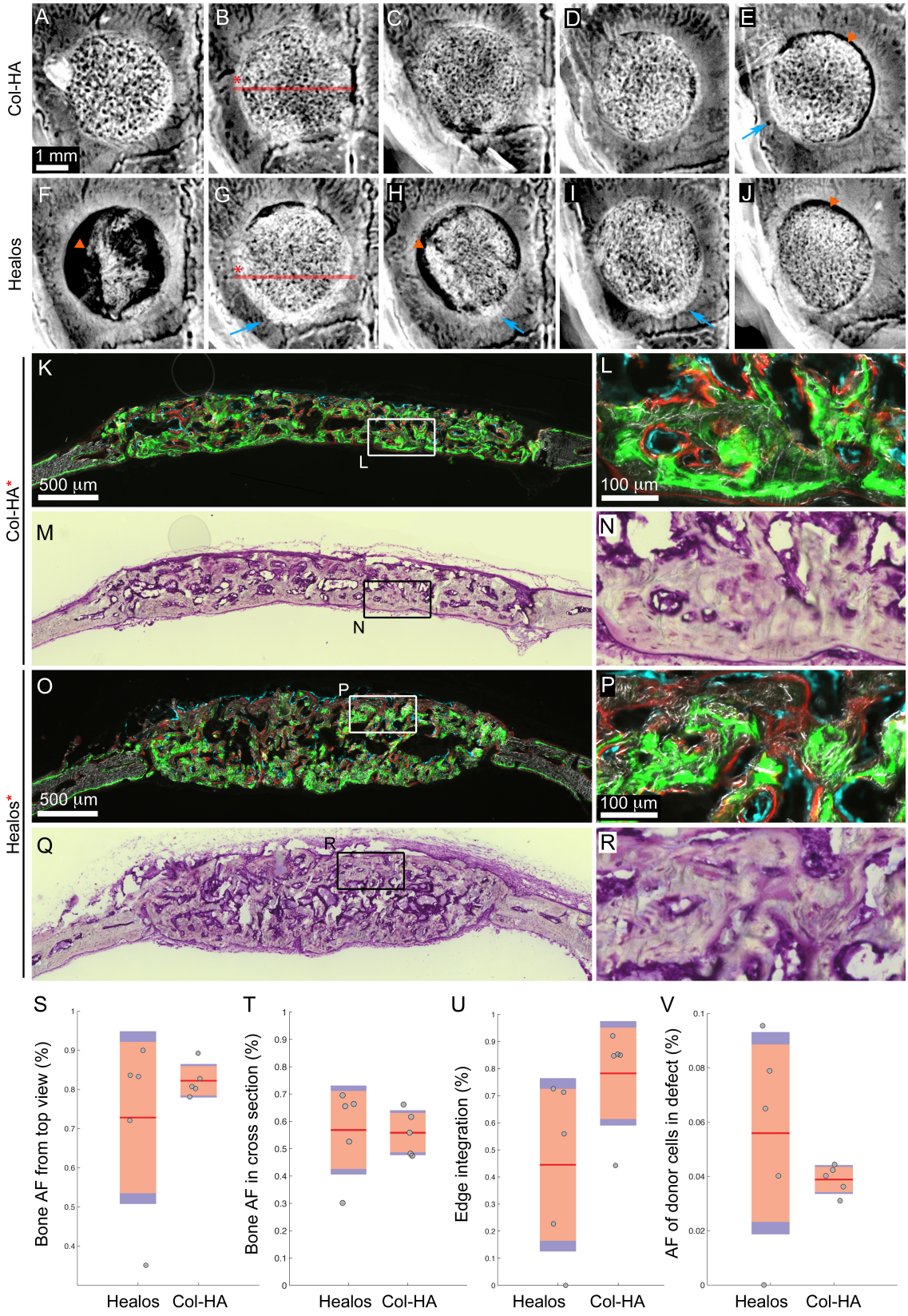
Col-HA
Healos
Col-HA*
Healos*
A
B
C
D
E
F
G
H
I
J
K
L
M
N
O
P
Q
R
1 mm
500 µm
100 µm
S
T
U
V
Bone AF from top view (%)
Bone AF in cross section (%)
Edge integration (%)
AF of donor cells in defect (%)
Healos
Col-HA

**Figure 4-8 | Evaluation of bone formation within mouse critical size calvarial defects after three weeks.** Radiographs of calvarial defects filled with mouse BMSCs in (A)-(E) Col-HA and (F)-(J) Healos® scaffolds after three weeks. Blue arrows indicate areas where the scaffold popped out of the defect. Orange arrows indicate sites of scaffold degradation. (K) Fluorescence and (M) toluidine-blue stained sections from (K)-(N) Col-HA and (O)-(R) Healos® scaffolds. The samples, (B) and (G), from which the sections, (K) and (O), came are indicated on the radiographs by the red line. Fluorescence images contain donor cells (cyan), mineralization label delivered at two weeks (green) and one day before sacrifice at three weeks (red), overlayed on a darkfield image of the mineralized tissue. Quantification of (S) bone area fraction from radiographs, (T) bone area fraction from histological sections, (U) edge integration from radiographs, and (V) area fraction of donor cells from histological sections. (S)-(V) Red line indicates the mean, pink bars indicate 95% confidence intervals and blue bars indicate one standard deviation. Individual samples are represented by dots.

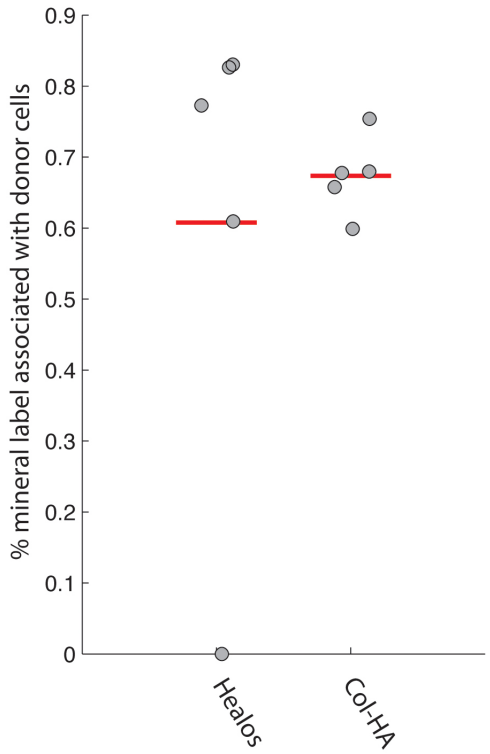


**Figure 4-9 | Donor cell colocalization to the surface of the mineralization label.**

## 4.4 Discussion

Biomaterials for cell delivery have enabled considerable progress towards consistent bone regeneration in defect sites.[65,164,165] However, challenges remain, such as cell survival in the implant[88] and realizing the ideal degradation rate of the biomaterial[63]. We have developed a type-I collagen-hydroxyapatite scaffold for cell-based bone tissue engineering that is relatively simple to fabricate, highly porous, and is easily remodeled by cells. Here we show that this biomaterial retains progenitor cells, supports robust new bone formation after only three weeks *in vivo*, and for the metrics and time point examined here, is comparable in performance to a clinical-grade material (Healos®), used here as a benchmark. Unlike the commercial benchmark, the Col-HA material is an open scaffold produced in an academic lab, facilitating further modification and development of this class of biomaterials towards healing bone defects in a clinical setting with culture-expanded osteoprogenitors.

The microstructure of the Col-HA scaffold is an interspersed composite of collagen fibers and HA nanoparticles (Fig. 4-2b), generated by simultaneous collagen fibrillogenesis and precipitation of HA nanoparticles. By contrast, Healos® is composed of collagen fibers with a thin coating of hydroxyapatite. The collagen component of the Col-HA scaffold is arranged in a triple-helical conformation, indicated by second harmonic imaging (Fig. 4-2h through 4-2k). Cell attachment to collagen has been reported to be strongly dependent on protein conformation.[121,152,166] The availability of collagen motifs on the scaffold surface may facilitate binding of cells, ECM proteins, and provide signals to infiltrating cells as the collagen is remodeled.

Employed here to fabricate the Col-HA scaffold, freeze casting is a relatively gentle process that accommodates the incorporation of proteins and generates a highly porous and thin-walled architecture. Due to the compliant mechanical properties of the collagen-HA scaffold, it may be best suited for non-loading bearing indications such as craniofacial repair. However, many bone fractures require fixation in combination with bone grafting, thus a compliant collagen-HA scaffold could theoretically be applied in a load bearing application when combined with mechanical fixation. If new bone quickly fills a defect, it will supersede the poor mechanical properties of the original scaffold, just as the soft cartilaginous callus becomes rigid bone following normal fracture healing. Additionally, a more radiolucent biomaterial, such as the Col-HA scaffold, enables better radiographic discrimination of the progression of new bone formation in a cell-seeded construct.

Marcacci *et al*. found that a pure hydroxyapatite scaffold was not fully degraded after 6 years of implantation with culture-expanded BMSCs in humans.[63] By contrast, the collagen-HA scaffold described here can degrade faster (~weeks) than pure hydroxyapatite scaffolds owing to MMP-mediated degradation of the collagen phase. A few of the collagen-HA scaffolds tested herein exhibited more rapid degradation (<3 weeks) at the peripheral edge. This type of rapid degradation impairs host integration and reduces the amount of bone formed. Rapid degradation may result from early MMP-mediated degradation of type I collagen by host cells of the innate immune system.[167–169] In a separate experiment, it was found that repeated surgery to expose the implant for live-animal imaging resulted in a similar radial gap between the host and implant,

whereas a control group that did not undergo additional surgery displayed much better integration, further pointing to an inflammatory mechanism behind peripheral scaffold degradation.[162] Neutrophil-derived MMP-8 has been reported to act on type I collagen scaffolds implanted in mouse myocardium.[169] Interestingly, when empty scaffolds were implanted in mouse calvarial defects, scaffolds persist without noticeable degradation (data not shown), suggesting a dependence on the donor BMSC population for peripheral scaffold degradation. BMSCs have been shown to play an immunomodulatory role *in vitro* and *in vivo*, with an anti- or pro-inflammatory effect proving at times variable and strongly dependent on the microenvironment they experience.[170,171] One possibility regarding the samples exhibiting degradation herein, is that the wound microenvironment experienced by the donor BMSCs did not drive them towards immunosuppression. Instead, primed by such a milieu, seeded BMSCs could have promoted neutrophil invasion and MMP-mediated degradation of the scaffold.[170]

Donor cells were predominantly responsible for bone formation in both groups of scaffolds, echoing earlier reports.[64,89,162] Here we observed Col3.6Cyan donor osteoblasts overlying a red mineralization label, providing a rigorous indicator that donor cells were responsible for *de novo* tissue formation. Since the scaffold is relatively thin (400-500 μm), diffusion of nutrient and waste removal appears sufficient to support cells through the early period following implantation when a functioning vasculature has not yet formed. Larger defects will likely require a more advanced vascular plexus prior to implantation to ensure donor cell survival. The limitations of this study include the relatively early time frame examined, the non-load bearing model, and the small sample

size (n=5). In the future, longer time points in a load-bearing defect combined with mechanical testing of the functional properties of new bone should be examined to more critically evaluate this approach.

## 4.5 Conclusion

We have developed a sterile collagen-HA scaffold for cell-based bone tissue engineering and examined its material properties and biological performance *in vitro* and *in vivo* combined with culture-expanded mouse BMSCs. The scaffold is composed of triple-helical type I collagen and poorly crystalline carbonated apatite arranged in a porous (93%) cellular architecture. When seeded to the scaffold, cells percolate through the full thickness of the thin geometry (~ 500 μm thick) and are fully attached to the biomaterial after 12 hours *in vitro*. The population of seeded cells just before implantation contained predominantly viable cells and large numbers of osteoprogenitors. When the Col-HA and control scaffolds were seeded with culture-expanded mouse BMSCs and implanted into a critical size calvarial defect, robust bone formation was observed in both groups at three weeks post implantation. For the number of scaffolds (n=5) and early time point investigated here, quantitative histomorphometry indicated no significant difference between the Col-HA and control scaffold in terms of bone formation and donor cell retention. The Col-HA scaffold is an open and well-defined platform that enables the researcher to have greater control of a cell-biomaterial model system, facilitating further development of collagen-hydroxyapatite biomaterials for cell delivery and bone defect repair.

# 5 Effects of a cell-attachment period and extracellular matrix cell on bone formation *in vivo* with collagen-hydroxyapatite scaffolds

## 5.1 Introduction

Cell-based bone tissue engineering holds promise to supplement or replace the limited supply of autologous bone for bone grafting procedures. Osteoprogenitors can be sourced from the bone marrow, expanded *in vitro*, and seeded to a scaffold to form a bone graft. Several animal studies using a scaffold combined with bone marrow stromal cells (BMSCs) have shown encouraging results healing bone defects.[65,164,172] This approach was also tested in a few human patients, and appeared to form new bone when viewed radiographically.[62,63] However, there has been no large-scale clinical trial of cell-based bone tissue engineering as of yet, and this approach has lagged behind growth factor based-approaches.[66] Negative side effects have been observed in connection with the delivery of a single morphogenetic factor, which requires very high doses to be effective.[77] By contrast, cells produce hundreds of factors during healing, and a cell-based approach could sidestep limitations regarding side effects associated with supraphysiological doses of growth factors. However, several issues remain before effective bone formation using culture-expanded osteoprogenitors becomes a clinical reality. These include optimizing cell delivery to a site of bone injury.

A number of methodologies have been proposed to optimize cell seeding efficiency[173–176] and *in vitro* culture conditions.[176–178] However there is limited *in vivo* evidence[179] describing which approaches are most effective at healing a bony defect. Presently in the clinic, whole bone marrow aspirate can be added to a scaffold material at the time of implantation. While this approach avoids any *in vitro* manipulation, and the associated time and cost, the progenitor number is very low in the bone marrow [37]. Previously, progenitor number has been correlated to the volume of mineralized callus formed after implantation to a fracture nonunion, and in some cases low progenitor number led to suboptimal healing.[153] By contrast, *in vitro* expansion can provide large numbers of osteoprogenitors and therefore increase the therapeutic power of a cell-based approach. Culture expansion is used here to ensure that large numbers of osteoprogenitors are delivered to the bony injury. Nonetheless, the degree of cell attachment, distribution, and phenotype in a cell-seeded scaffold is largely unknown. Therefore the construct initial conditions (cell attachment, number, viability, phenotype) require continued examination in terms of *in vivo* outcomes. Examination of a tissue-engineered construct prior to implantation can be a useful quality control checkpoint when used in the clinic.[86] Previous work in the mouse has shown an upper limit on the length of time osteoprogenitors can be cultured *in vitro* and still produce bone *in vivo*.[179] In this case, a length of about six to eight days corresponded to maximal bone formation, due to increasing osteoblastic differentiation beyond this period. Similarly, it has also been suggested that when human cells are used for bone tissue engineering, an osteoprogenitor phenotype, rather than differentiated osteoblasts, may lead to better *in vivo*

osteogenesis.[180]

Cell attachment is linked to cell viability through integrin binding[181] and may enhance the survival of implanted cells.[88] We sought to evaluate the effect of a cell-attachment period prior to implantation on bone formation. To examine this question, bone formation within scaffolds seeded at the time of implantation was compared to scaffolds seeded and incubated overnight to allow complete cell attachment prior to implantation (Fig. 5-1). Implanted constructs were examined with radiography and histology after three weeks *in vivo*. If cell attachment prior to implantation improves *in vivo* outcomes, this would have implications for the clinical delivery of cells, which are currently seeded to a scaffold at the time of implantation. The vast majority of cells are not attached to the scaffold within minutes of seeding.[182] More critically, it is unclear if the *in vivo* wound microenvironment promotes or hinders cell attachment.

We also sought to evaluate the effect of an extracellular matrix (ECM) carrier material on bone formation, possibly helping to hold cells in position after seeding, and/or conferring benefits such as synergistic signaling by the ECM.[29] The ECM performs several critical roles in signal presentation and transduction.[19,29,183–185] Recent reports have indicated that the ECM promotes cell retention, survival, and differentiation.[88,97,186] Here we evaluated the use of a reduced growth factor formulation of basement membrane extract (BME) gel (Cultrex®, Trevigen Inc., also sold as Matrigel®) as a cell suspension to seed osteoprogenitor cells to a scaffold. BME gel consists mainly of laminin, entactin, and collagen IV. Four hundred and eighty unique proteins were identified within growth

factor-reduced BME, representing a complex matrix of extracellular, binding, catalytic, and regulatory proteins.[187]

The goals of this work were to (i) examine the effect of a cell attachment period prior to implantation on bone formation, and (ii) to assess the effect of a complex ECM as a secondary delivery carrier on bone formation. We evaluated these conditions in two different collagen-hydroxyapatite scaffolds, Healos® (DePuy) and an in-house scaffold, here denoted Col-HA. Identifying the optimal conditions for cell-delivery should improve the efficacy and repeatability of cell-based bone tissue engineering.

## 5.2 Materials & Methods

### 5.2.1 Scaffold fabrication and sterilization

To fabricate the in-house scaffold, type-I collagen was first derived from rat tail tendons following Rajan *et al*.[154] A collagen-hydroxyapatite composite was then formed by self-assembly of collagen fibers in the presence of precipitating hydroxyapatite from a modified simulated body fluid (m-SBF)[188]. Briefly, the collagen solution was adjusted to 2.5 mg/mL by a two-fold dilution in sterile ultrapure water at 4 °C. To make a 200 mL solution of collagen-containing m-SBF, the following salts were added in the order they appear to the 2.5 mg/mL collagen solution: 1.080 g NaCl, 0.142 g $K_2PO_4$, 0.062 g $MgCl_2$, 2.400 g (4-(2-hydroxyethyl)-1-piperazineethanesulfonic acid) HEPES, 0.175 g $CaCl_2$, and 0.294 g $NaHCO_3$. While kept cold to prevent collagen fibrillogenesis, the pH of the solution was adjusted to 7.0 with sodium hydroxide solution and then transferred to a water bath at 40 °C for 24 hours to allow simultaneous precipitation of hydroxyapatite

and collagen fibrillogenesis. The gel-precipitate was centrifuged at 11,000 g and 4 °C for 12 min. The supernatant was discarded and the pellet was lyophilized (FreeZone 12L, Labconco). The collagen-HA precipitate was reconstituted with water at a concentration of 100 mg/mL, briefly homogenized to obtain a uniform slurry, and frozen in a polystyrene culture dish from room temperature to -40 °C at a cooling rate of -0.37 °C/min. Following drying, the scaffold was immersed in a solution of 20 mg/mL EDC [1-ethyl-3-(3-dimethylaminopropyl) carbodiimide hydrochloride] for 24 hours at 4 °C to covalently crosslink the collagen fibers. The scaffold was then rinsed in a solution of 5% (w/w) glycine in sterile water for an overnight period in order to block unreacted EDC. Crosslinking was followed by three sequential rinses in sterile water for 15 minutes each at 4 °C. Finally, rinsed scaffolds were freeze-dried, cut to a thickness of ~500 μm with a milling machine and punched to a diameter of 3.5 mm. Scaffolds were terminally sterilized with a 24-hour cycle of ethylene oxide gas (Anprolene AN74i, Anderson Products). The Healos® material was received sterile. Healos® is a lyophilized bovine type-I-collagen sponge with high porosity and a pore size ranging from 4-200 μm, coated with a thin layer of calcium phosphate.

### 5.2.2 *In vitro* culture of bone marrow osteoprogenitors

Mouse BMSCs were isolated from the femur and tibia of OsterixCRE/Ai9 B6 animals. Osterix is a critical regulator of osteoblast differentiation.[189] The combination of the OsterixCRE and Ai9[190] transgenes activate the expression of the TdTomato (red) fluorescent protein following Osterix expression. This reporter construct activates the production of TdTomato when a cell expresses Osterix, and continues expression of

TdTomato in subsequent daughter cells. Thus, following three weeks of *in vivo* implantation, the TdTomato signal will label osteoprogenitors, committed osteoblasts, and osteocytes. Bone marrow cells from femur and tibia were collected by a centrifugation method. Briefly, interlocking filtration column and collection tubes were modified by removing the filter and autoclaved. Femur and tibia were cut in half and placed cut end down in the top tube. The bones were spun at 3100 g for 2 minutes, ejecting the bone marrow cells into the lower collection tube containing 100 mL of PFE (98% PBS, 2% FBS, 2 mM EDTA) to prevent clotting. Bone marrow cells were flushed through a 70 mm cell strainer (BD Biosciences) and re-suspended in α-MEM. Cells were then added to 100 mm culture dishes in warm α-MEM (Gibco) containing 10% fetal bovine serum and 1% penicillin-streptomycin. To allow hematopoietic cells to contribute to the expansion of osteoprogenitor cells, the culture medium was changed four days after seeding the bone marrow pellet. Two different types of scaffolds (Healos® and Col-HA) were seeded the day before implantation or incubated overnight, with or without BME gel as a seeding suspension, resulting in eight groups (n=3). The sample hierarchy is shown schematically in Fig. 5-1A. Cells were either seeded in a suspension of growth factor reduced Basement Membrane Extract (BME, 15 mg/mL in PBS, Trevigen) or in a suspension of α-MEM. The cell suspension was made by adding 15 mL of culture medium, or cold BME, to a cell pellet containing $1.0\times10^6$ cells, resulting in a concentration of $6.66\times10^7$ cells/mL. Prior to seeding, adherent BMSCs were trypsinized and seeded dropwise on top of either the dry Col-HA scaffold or Healos®. After seeding, cells were allowed to settle for 30 minutes before an additional one mL of warm culture medium was added to the culture well. On the day of implantation, samples denoted

'implanted immediately' were seeded with $1.0\times10^6$ cells in 15 µL of culture medium, or BME, and implanted in less than one minute after seeding.

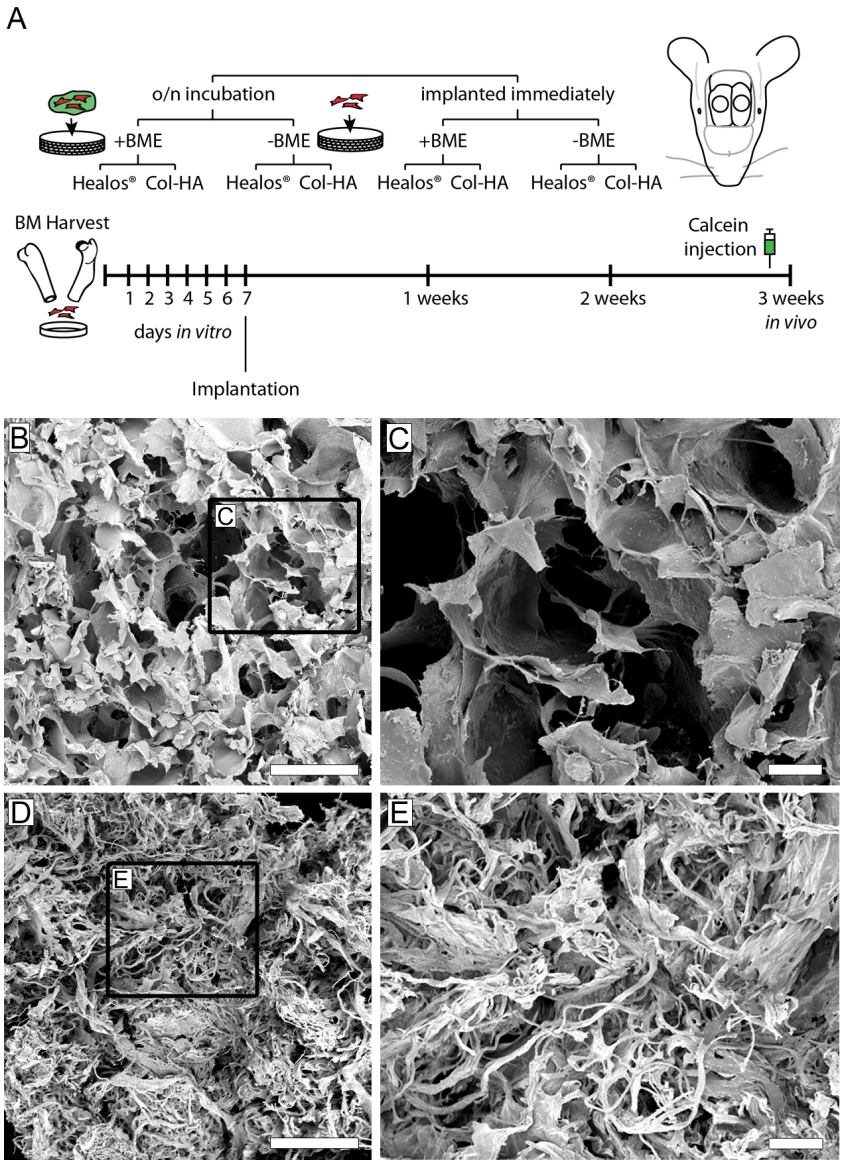


**Figure 5-1 | Experimental design and scaffold morphology.** (A) Schematic of Experimental Design. Osteoprogenitors from the bone marrow were expanded *in vitro* before seeding to collagen-hydroxyapatite scaffolds and implanted in critical size calvarial defects. To label areas of active mineralization, calcein was injected intraperitoneally one-day prior to euthanization at three weeks post-implantation. (B) Electron micrograph of the Col-HA scaffold showing cellular morphology. Scale bar is 500 µm. (C) Enlarged inset from (A). Scale bar is 100 µm. (D) Electron micrograph of Healos® scaffold. Scale bar is 500 µm. (E) Enlarged inset from (D). Scale bar is 100 µm.

### 5.2.3 *In vivo* mouse model of bone repair

On the day of implantation, nod *scid* gamma immunodeficient mice were anesthetized with a ketamine (135 mg/kg) – xylazine (15 mg/kg) blend and two 3.5 mm diameter critical-size defects were made in the right and left parietal lobe using a bur trephine (RAL #229-030, Benco Dental). Extreme care was taken to prevent damage to the dura mater beneath the calvarium. Seeded constructs were placed in the defects, alternating the order of scaffold type in the left and right hole, for each of the 12 animals. Following closure of the scalp with resorbable sutures, animals were given postoperative analgesic (bupronephrine, 0.08 mg/kg). One day prior to euthanization at three weeks post-implantation, host mice were injected intraperitoneally with calcein to mark surfaces of active mineralization. All procedures used in this study were approved by the UConn Health Center Institutional Animal Care and Use Committee (IACUC).

### 5.2.4 Image acquisition and analysis

After three weeks of implantation, animals were euthanized, and the extracted calvarium were fixed in 10% formalin overnight. The following day, samples were placed in a 30% sucrose solution, while kept cold and in the dark for another overnight period. Radiographs of calvarium were acquired with a digital X-ray system (MX20, Faxitron). The samples were then prepared for histology by trimming the calvaria to the defect regions, and embedding each sample in Cryomatrix (Thermo). Three sections were cut from each calvarium using a cryostat (Leica) and tape to transfer sections to a glass slide

(Cryofilm Type2C, Section-Lab). All sections were imaged with a 10× objective on a fluorescent microscope (Axio Scan.Z1, Zeiss) equipped with stage automation and an LED light source (Colibri.2, Zeiss).

Bone formation was quantified from radiographic images by selecting a region of interest (ROI) surrounding only the defect area and calculating the mean pixel intensity using FIJI.[142] To quantify the area fraction of donor cells, calcein label, and darkfield signal from histological sections for each group, an ROI outlining the defect area was manually drawn for each image and saved using FIJI. A threshold was then applied to each channel, and the area fraction was calculated from the total defect area. To process the images as a batch and ensure the same threshold was consistently applied, a macro was written for FIJI.

To determine the position of each cell pixel relative to the outside edge of the implant, a distance mapping technique[106] was performed. Briefly, a distance transformation was applied to the defect region, coding pixel intensity according to pixel distance from the outer perimeter of the defect (i.e. intensity of 20 corresponds to 20 pixels from the perimeter). Then a threshold was applied to the cell image and converted to binary (0 for background, 255 for cells) to be used as a mask when applied to the distance map. The image calculator tool was used to find the minimum value between the distance map and the cell mask. Since the cell pixels are always higher than the map pixels in this case, the resultant image contains distance-coded information at each cell pixel. Noting the spatial

conversion from pixels to microns, a histogram of the resultant image yields the number of cell pixels as a function of distance from the outside edge for each section.

### 5.2.5 Statistical Analysis

Quantitative data is presented as the mean ± standard deviation (error bars and blue bars). In some cases 95% confidence intervals (light red bars) are also included. A two-sample independent t-test was used to determine significance between groups. P-values less than 0.05 (both tails) were considered statistically significant and are indicated with an asterisk. P values less than 0.01, 0.001, and 0.0001 were indicated with two, three, and four asterisks, respectively.

### 5.2.6 Permeability Measurement

The permeability, k ($m^4$/Ns), of Healos® and Col-HA scaffolds was measured with water and a custom flow cell using the following equation found in reference [159]:

$$k = \frac{\Delta x}{A \cdot M_{B2}} \cdot \frac{2\pi^2 r^4}{(M_{B1}/M_{B2})^2 - 1}$$

where, $\Delta x$ = scaffold length (m), A = scaffold cross-sectional area ($m^2$), $M_{B1}$ = mass flow rate without scaffold (g/s), $M_{B2}$ = mass flow rate with scaffold (g/s), and r = radius of the outlet (m).

## 5.3 Results

### 5.3.1 *In vitro* examination of expanded cells

Four days after plating whole bone marrow, colonies of fibroblastic cells had begun to appear in the culture dish. Following six days *in vitro*, colonies had proliferated and become confluent. When examined using a fluorescent microscope, fibroblastic cells were positive for the TdTomato osteoprogenitor marker (Fig. 5-2), indicating that large numbers of osteoprogenitor cells were present in the culture dishes prior to scaffold seeding.

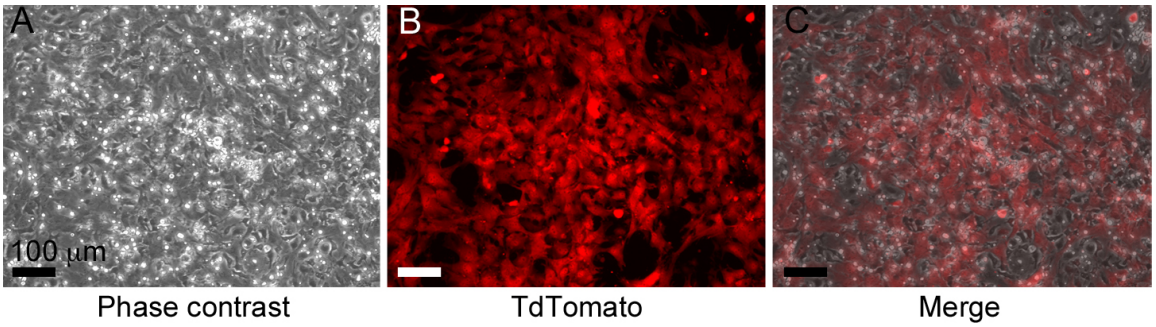


**Figure 5-2 | Osteoprogenitor cells following six days of *in vitro* expansion.** (A) Phase contrast showing near confluent cell culture, (B) TdTomato reporter driven by OsterixCRE and (C) Merged image of (A) and (B) indicating a large fraction of cultured cells are osteoprogenitors.

### 5.3.2 Radiographic evaluation of calvarial defects following three weeks *in vivo*

Three weeks after implantation, calvaria were harvested to examine the implants. By radiographic discrimination (Fig. 5-3), it appeared that all samples contained areas of radiopacity indicative of mineralized tissue. Both scaffolds contain hydroxyapatite (~30% by weight), however if collagen-HA scaffolds seeded with cells undergo mineralization *in vivo*, a clear increase in radiopacity is observed (an example radiographic progression

is shown in Fig. 5-4). Two of the 24 scaffolds had moved from the defect region (Fig. 5-3C and 5-3M), however the remaining implants appeared in good contact with the surrounding host bone. Quantification of the radiographic images showed significantly greater radiopacity in the Col-HA samples seeded immediately compared with the Col-HA samples provided an overnight incubation (Fig. 5-3N). When BME gel was used as the seeding medium during overnight incubation of Col-HA samples, the mean radiopacity was greater than Col-HA samples incubated overnight without BME gel (Fig. 5-3N). Histological examination was performed to further examine implant osteogenesis.

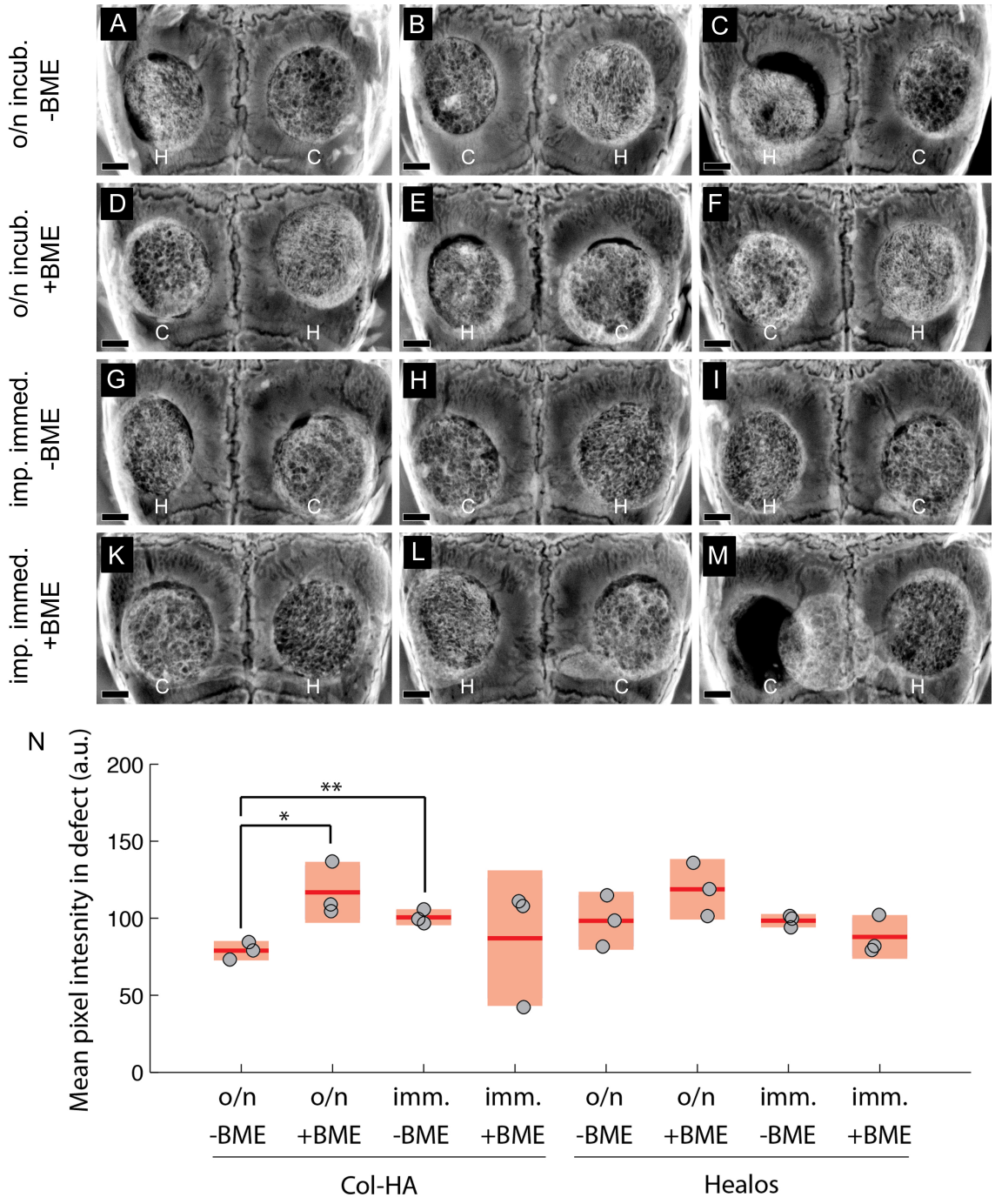


**Figure 5-3 | Radiographs of cell-scaffold constructs after 3 weeks *in vivo*.** (A)-(M) H and C denote Healos and Col-HA scaffolds, respectively. Scale bars are 1 mm. (N) Quantitation of radiographs. Light red bars indicate 95% confidence intervals and blue bars indicate one standard deviation.

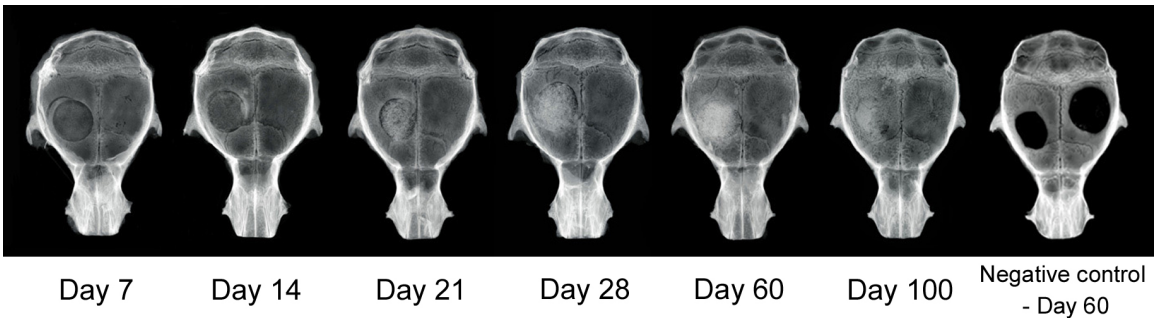


**Figure 5-4 | Radiographic progression of calvarial repairs.** 4 mm critical-size calvarial defects filled with Healos® scaffold and neonatal calvarial cells. Radiographs show progression of increase in radiopacity as scaffolds are mineralized over 7, 14, 21, 28, 60, and 100 days after surgery. The rightmost image shows the negative control calvarium, which includes defects filled with the Healos® scaffold alone (right hole) and no scaffold or donor cells (left hole).

### 5.3.3 Histological evaluation of calvarial defects following three weeks *in vivo*

To verify bone formation and determine the distribution of donor cells in the implants (marked by a TdTomato fluorescent reporter, Fig. 5-2), histological sections of the calvaria were generated (Fig. 5-5). Histological examination of the implants showed bone formation in several samples, indicated by donor cells embedded in a mineral phase (Fig. 5-5, right column, blue arrows). Modest bone formation was found in the Col-HA groups incubated overnight (Fig. 5-5A and 5-5E). The Healos® samples appeared to contain more bone and less scaffold than the Col-HA samples, which contained areas of scaffold still intact (Fig. 5-5F and 5-5N, white astericks). Several pores in the Col-HA scaffolds did not contain donor cells (Fig. 5-5A, 5-5F, and 5-5N), suggesting limited cellular invasion.

The Healos® samples without incubation (Fig. 5-5K and 5-5O) had larger marrow spaces than the Healos® samples with an overnight incubation prior to implantation (Fig. 5-5C

and 5-5G). Marrow spaces also contained cells of donor origin (Fig. 5-5P and 5-5L). Fewer marrow niches appeared to have emerged in the Col-HA samples (Fig. 5-5A, 5-5E, and 5-5M).

Donor cells were found on the surface of the mineral label, pointing to their contribution to bone formation in the defects (Fig. 5-5, white arrows). Mineral label was present in all samples, indicating the label was able to diffuse into the tissue by systemic delivery. Some regions of the Col-HA scaffold appeared to take up the mineral label as a weak nonspecific stain (Fig. 5-5F and 5-5N, white astericks) rather than a distinct line characteristic of an active mineralizing surface.

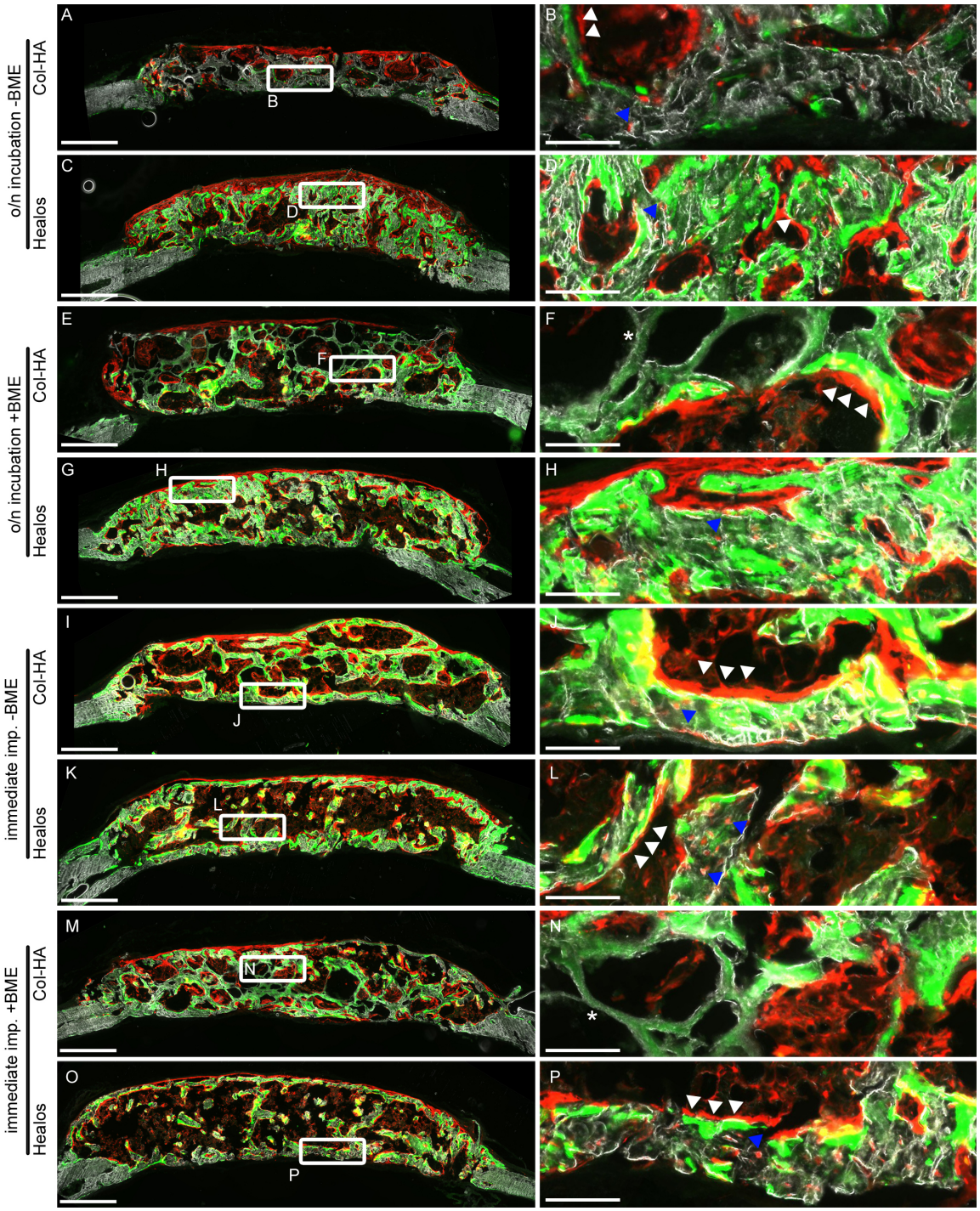


**Figure 5-5 | Histological sections of defects following 3 weeks of *in vivo* implantation.** (Left column) Defect wide view of scaffolds and mineralized tissue (darkfield channel), +TdTomato donor cells (red), and the mineralization label (green, calcein). Scale bars are 500 µm. (Right column) Magnifications of left column. Blue arrows indicate +TdTomato donor cells embedded in bone. White arrows indicate +TdTomato donor cells overlying mineral label. Scale bars are 100 µm.

### 5.3.4 Quantitative histomorphometry following three weeks *in vivo*

To quantitatively compare the experimental groups, a histomorphometric analysis was performed. Analysis of the darkfield channel (shown as the grayscale channel in Fig. 5-5) indicated that the Col-HA groups implanted immediately had a higher mean darkfield area fraction than the Col-HA groups incubated overnight (Fig. 5-6A). It should be noted that the darkfield signal contains areas of bone and scaffold, as shown in Fig. 5-5E. When the donor cell area fractions were examined, both Healos® and Col-HA samples wherein cells were implanted immediately had significantly higher area fractions of donor cells than the same scaffold type given an overnight attachment period (Fig. 5-6B). The Col-HA samples implanted immediately had a higher mean calcein area fraction compared with the Col-HA samples incubated overnight (Fig. 5-6C). By contrast, the mean donor cell and calcein area fractions were very similar whether or not BME gel was applied. As a whole, histomorphometric analysis of the darkfield, donor cell, and calcein area fractions supported the notion that immediate implantation led to an defect with more donor cells and mineralizing surfaces compared with samples incubated overnight.

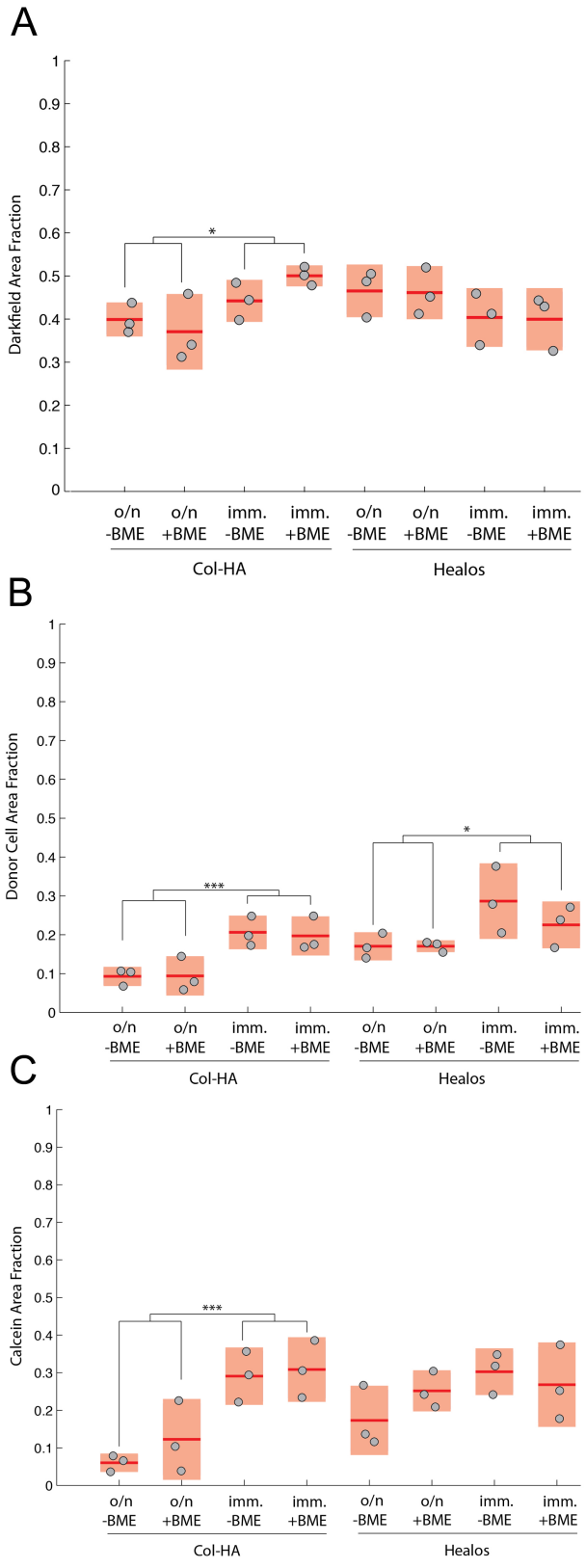
A
Darkfield Area Fraction
1
0.9
0.8
0.7
0.6
0.5
0.4
0.3
0.2
0.1
0
*
o/n -BME
o/n +BME
imm. -BME
imm. +BME
o/n -BME
o/n +BME
imm. -BME
imm. +BME
Col-HA
Healos
B
Donor Cell Area Fraction
***
*
C
Calcein Area Fraction
***

**Figure 5-6 | Quantitative histomorphometry of darkfield, donor cell, and calcein channels.** (A) Quantification of the darkfield area fraction in the defect area. (B) Quantification of donor cell area fraction using TdTomato signal. (C) Quantification of mineralizing surface using the calcein mineralization label. Light red bars indicate 95% confidence intervals and blue bars indicate one standard deviation.

To examine the effect of scaffold type and delivery method on the distribution of donor cells in the implant, a distance analysis was performed. For each defect, a distribution of donor cells as a function of distance from the outside edge of the implant was generated. When viewed by scaffold type, the donor cell distribution in the Healos® samples was not significantly deeper when compared to the Col-HA samples (Fig. 5-7A). Interestingly, the groups incubated overnight had significantly deeper mean cell penetration when BME gel was included, regardless of scaffold type (Fig. 5-7B). The inclusion of BME gel may increase cell penetration only if cells are incubated in the scaffold overnight.

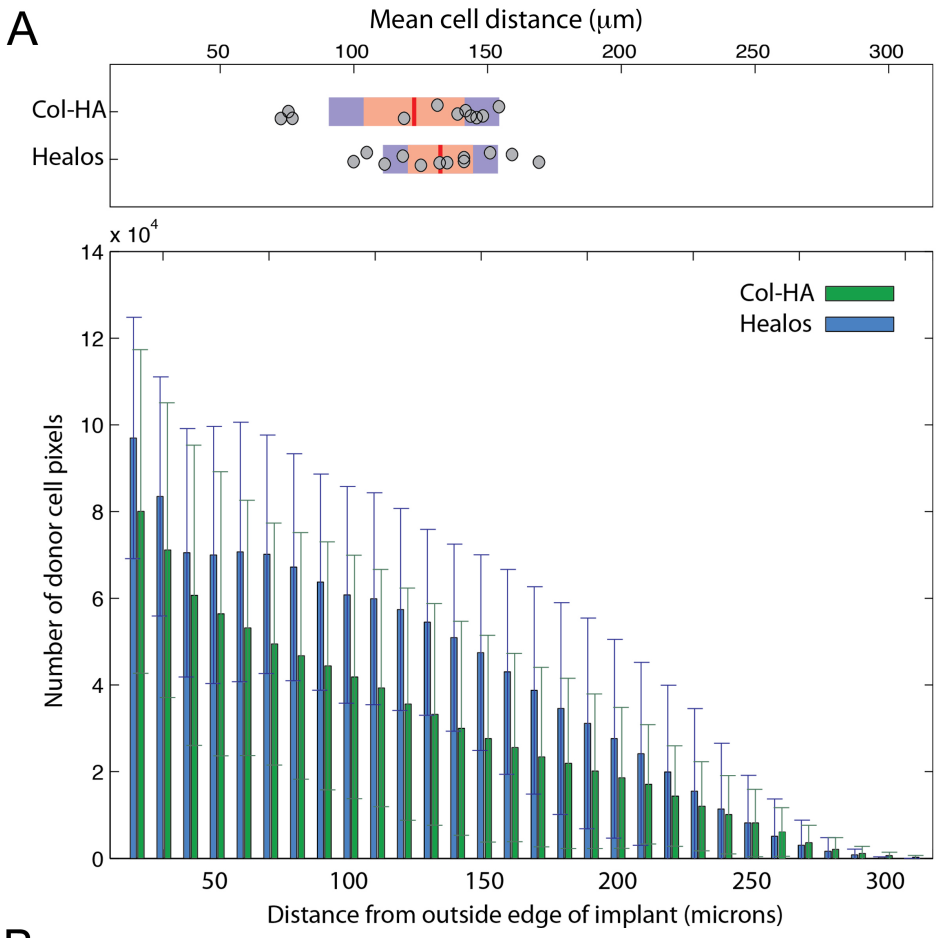
A
Mean cell distance (μm)
50
100
150
200
250
300
Col-HA
Healos
x 10^4
14
12
10
8
6
4
2
0
Col-HA
Healos
Number of donor cell pixels
50
100
150
200
250
300
Distance from outside edge of implant (microns)

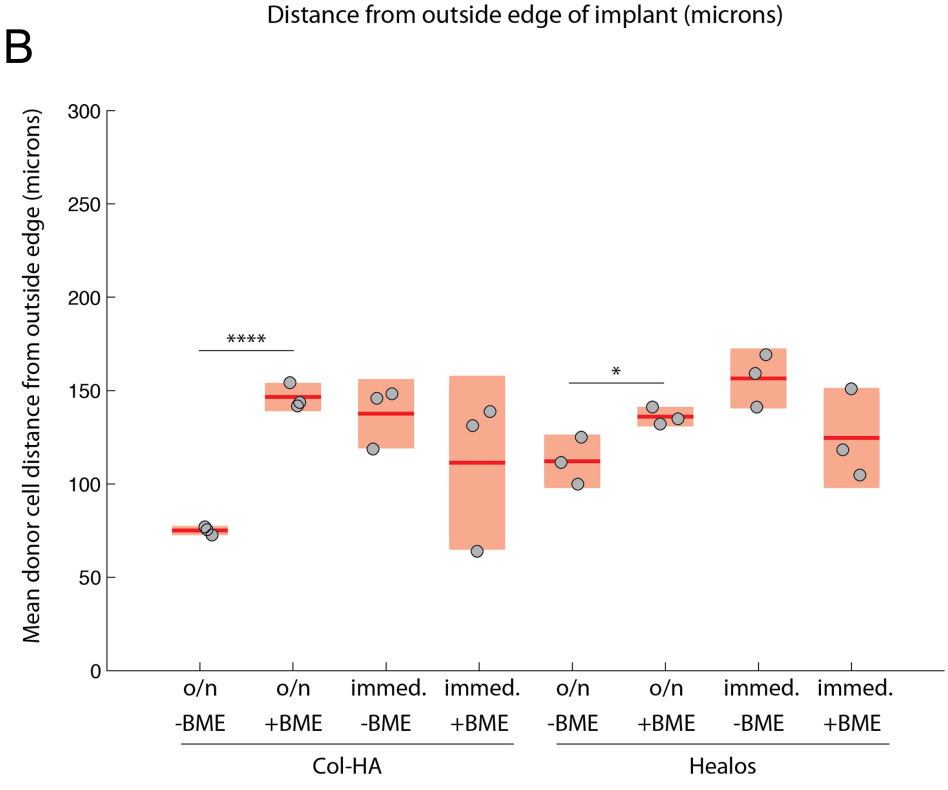
B
Mean donor cell distance from outside edge (microns)
300
250
200
150
100
50
0
****
*
o/n -BME
o/n +BME
immed. -BME
immed. +BME
o/n -BME
o/n +BME
immed. -BME
immed. +BME
Col-HA
Healos

**Figure 5-7 | Donor cell distribution in the scaffolds.** (A) Comparison of donor cell distribution from the outside edge of the implant for Healos® and Col-HA. Error bars indicate one standard deviation. Plot above shows a comparison of the means for each sample according to scaffold type. (B) Comparison of the mean donor cell distance from the outside edge of the implant. Light red bars indicate 95% confidence intervals and blue bars indicate one standard deviation.

### 5.3.5 Permeability measurement of scaffolds used *in vivo*

When the permeability of the two scaffolds was compared, the Healos® sample was more permeable than the Col-HA sample by three orders of magnitude, $4.2 \pm 3.4\times10^{-9}$ and $2.9 \pm 3.0\times10^{-12}$ $m^4$/N-s, for Healos® and Col-HA, respectively.

## 5.4 Discussion

We examined if an *in vitro* cell attachment period before implantation, and/or an ECM-based delivery suspension, would improve donor cell survival and bone formation *in vivo*. The outcome of the experiment presented here suggests that immediate implantation improves donor cell delivery and scaffold mineralization; likely due to a higher number of cells implanted in this case (Fig. 5-8). Immediate loading corresponded to a higher mean radiopacity in the Col-HA scaffolds compared with Col-HA scaffolds provided with an overnight incubation (Fig. 5-3N). Similarly, the donor cell area fraction was significantly higher for both types of scaffolds implanted immediately compared with the same scaffold type incubated overnight. Finally, the mean area fraction of the mineralization label was significantly higher for the Col-HA scaffolds implanted immediately compared with Col-HA scaffolds given an overnight incubation (Fig. 5-6C). This suggests that cell attachment and survival may not be hampered by the *in vivo* microenvironment of a fresh bone injury. Furthermore, immediate seeding and

implantation is faster, requires less cell manipulation, and in this study, enabled the delivery of significantly higher numbers of donor cells (Fig. 5-8). The efficient use of a precious cell source would also be advantageous to the user. An increase in radiopacity was not found in the Healos® groups seeded immediately, possibly because of bone remodeling characteristic of a more advanced healing stage [55]. This was evidenced by the large marrow spaces found in Fig. 5-5K and 5-5O, which would reduce the overall radiopacity compared to Healos® groups incubated overnight (Fig. 5-5C and 5-5G).

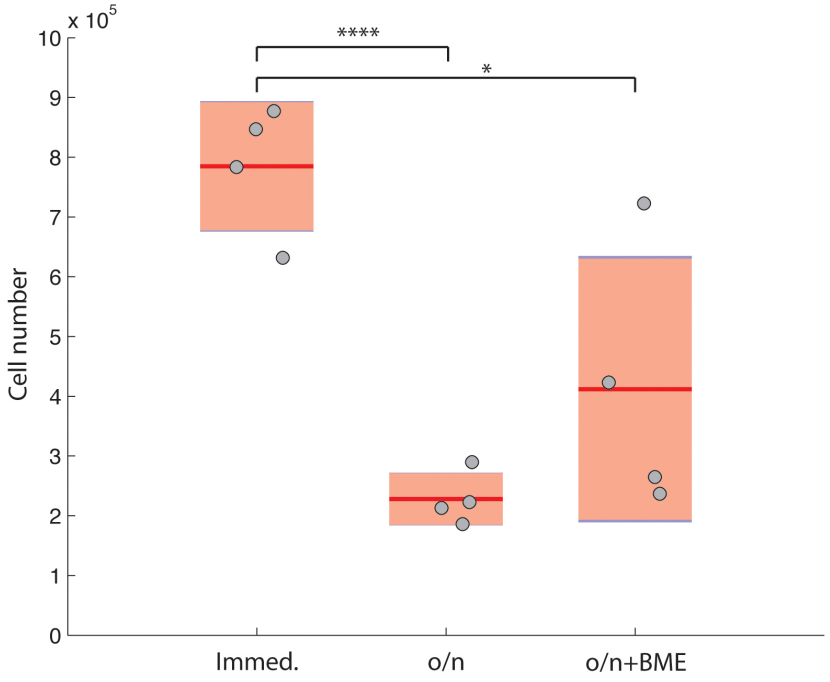


**Figure 5-8 | Comparison of cell number in Col-HA scaffolds.** Cell number was evaluated immediately after loading and following an overnight incubation with and without BME gel**.** Light red bars indicate 95% confidence intervals and blue bars indicate one standard deviation.

Tissue engineers should endeavor to form bone with the marrow spaces found anatomically. For instance, the large marrow spaces of the long bone diaphysis would be inappropriate in the calvarium, which contains smaller marrow spaces. Larger marrow spaces were observed between the Healos® groups implanted immediately (Fig 5-5K and 5-5O), compared with the Healos® groups provided an overnight incubation (Fig. 5-5C and 5-5G). The same trend was found when comparing the darkfield area fractions in Fig. 5-6A. Lower darkfield area fractions corresponded to Healos® samples with larger marrow spaces shown in Fig. 5-5K and 5-5O, although this effect was not significant here, possibly due to low statistical power (n=3). Increased remodeling in samples implanted immediately may stem from a greater hematopoietic fraction, the population responsible for producing bone-remodeling osteoclasts. In other words, an overnight incubation could select for a more homogeneous population of mesencyhmal stem cells. Adherence to tissue culture plastic is a well-known selector of mesencyhmal stem cells from the bone marrow,[191,192] and a second attachment process may purify this population by further removing non-adherent hematopoietic cells. As an indicator of bone resorption, we examined a marker for osteoclast activity using TRAP staining of histological sections from the implants (Fig. 5-9). We did not find differences in TRAP activity corresponding to delivery with or without an overnight incubation period. However it is possible that differences in osteoclast activity were present at an earlier time point and would not be observed by examining osteoclast activity after such a remodeling event.

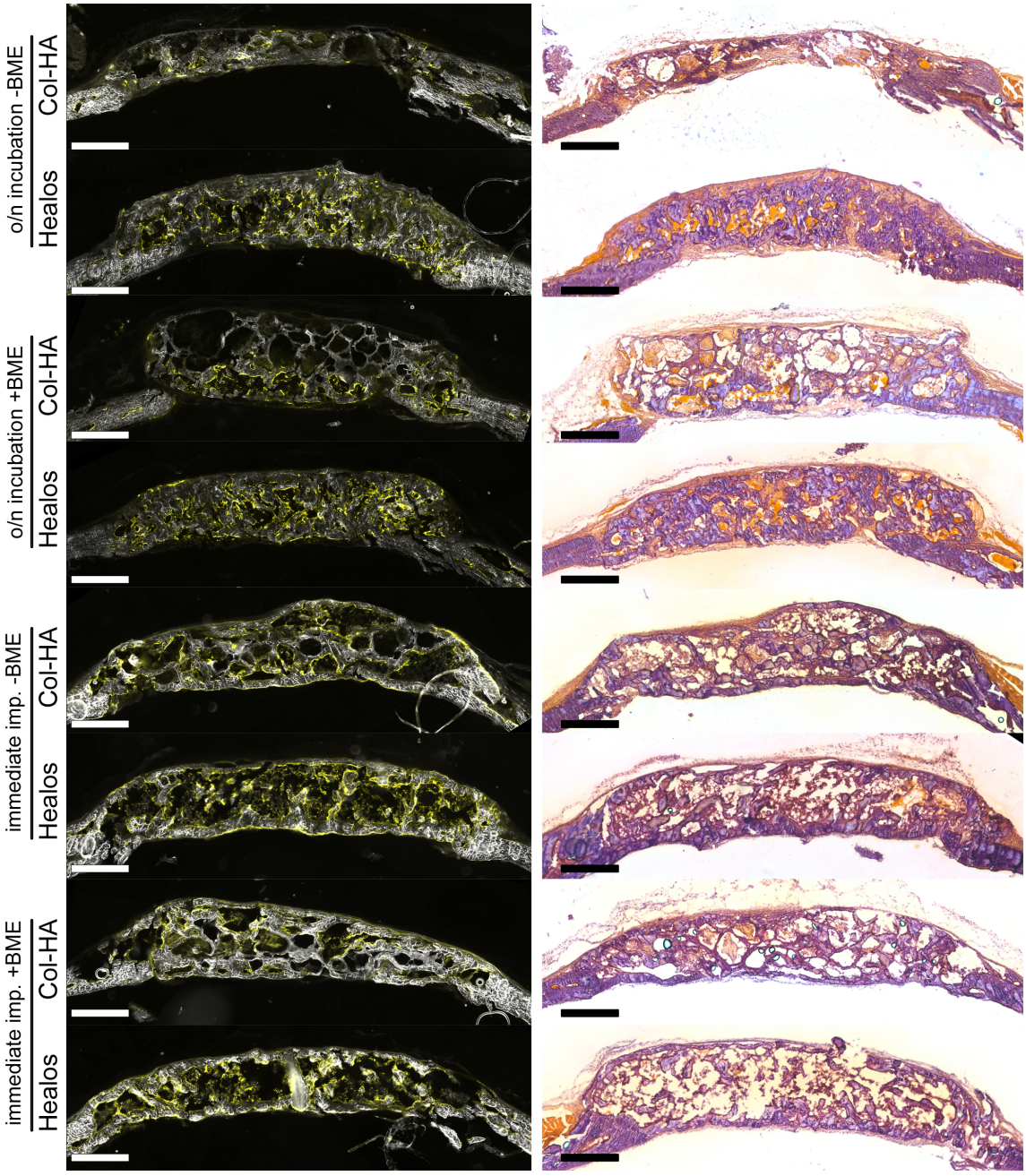


**Figure 5-9 | TRAP and H&E staining of histological sections.** (Left column) TRAP staining (yellow) superimposed on darkfield images of transverse scaffold sections. (Right column) Hematoxylin and eosin staining of histological sections. Scale bars are 500 µm.

An *in vitro* test showed significantly higher loading numbers in Col-HA scaffolds simulating the immediate implantation method compared with overnight incubation (Fig.

5-8). The discrepancy in cell number between immediate implantation versus overnight incubation samples was due to cell loss to the culture dish when medium was added to the scaffold and when the scaffold was removed from the dish, therefore we expect similar results for Healos® scaffolds. It is tempting to speculate that the delivery of a greater number of MSCs in the samples delivered immediately could lead to a more potent hematopoietic niche, resulting in larger marrow spaces in the Healos® groups implanted immediately. The evidence supporting this hypothesis stems from the finding that implanted MSCs create a hematopoietic microenvironment that leads to the establishment of marrow cavities.[191] Krebsbach *et al*. noticed that the delivery of higher numbers of MSCs in a thick gelatin vehicle corresponded to the establishment of larger marrow spaces, even though the hematopoietic fraction was very small.[164] Similarly, Liu *et al.*, using cell sorting to generate a homogeneous population of osteoprogenitors, observed larger marrow spaces with a higher cell loading.[42] MSC number positively correlates with bone formation in sites of bone injury.[153] However, MSCs are also a critical component of the native hematopoietic microenvironment and strongly regulate hematopoietic stem cell function through cell-secreted factors (*e.g.* CXCL12) and cell adhesion proteins (*e.g.* Nestin).[50,193] Further work is needed to examine if the number of seeded MSCs affects the marrow size of a bony implant.

We also investigated if delivering cells to the scaffolds in a complex ECM would enhance *in vivo* bone formation. Several groups have observed beneficial effects of ECM proteins on wound repair and bone formation.[29,88,97,186] ECM proteins can sequester and synergistically amplify signaling factors.[29,185] Furthermore, a two-component system of

collagen-hydroxyapatite is far simpler than the composition of bone.[6] Herein, cells were delivered to scaffolds in a suspension of liquid BME that later gelled upon incubation at 37 °C. The application of BME gel improved cell penetration (Fig. 5-7) in both scaffold types and increased the mean radiopacity of the Col-HA scaffolds (Fig. 5-3N), only when an overnight incubation period was applied. This could be due to BME gel acting to hold cells in place *in vitro*, since without BME gel, cells can be removed during medium addition after initial seeding and scaffold removal from the culture dish. The evidence to support this hypothesis is that cells depend on proteolytic degradation of the surrounding matrix in order to migrate through BME[194]. This would slow cell migration in BME gel compared with an environment where cells do not require matrix degradation to migrate. Similarly, gels typically have a relatively low permeability, (Collagen gel, $k \sim 10^{-13}$-$10^{-12}$ $m^4/Ns$)[195], which could also reduce cell migration. This suggests that improved cell distribution in scaffolds incubated overnight with BME gel may not be due to enhanced migration, but rather improved cell retention in the scaffolds *in vitro*. The reason that this effect was not observed in the samples implanted immediately could be due to the higher number of delivered cells in groups implanted immediately (Fig. 5-8). Alternatively, if the effect of BME application on the cell distribution were small for the immediately seeded groups, this would not be noticed here given the small number of animals per group (n=3).

Some of the Col-HA samples contained modest bone formation (Fig. 5-5E and 5-5A) compared with the Healos samples (Fig. 5-5C and 5-5G), even when both scaffolds were incubated overnight. The Healos scaffolds had a permeability three orders of magnitude

higher than the Col-HA samples used in this study. It has been previously shown by Mitsak *et al*., using polycaprolactone scaffolds and a 3-D printing approach, that increased scaffold permeability led to more bone ingrowth *in vivo*.[196] Future work should evaluate the effect of collagen-HA scaffold permeability on bone formation *in vivo*.

## 5.5 Conclusion

In summary, we evaluated the effect of an *in vitro* attachment period, the use of BME gel as a cell delivery vehicle, and scaffold type on bone formation *in vivo* with culture-expanded mouse BMSCs. Both scaffold types, with or without an overnight attachment period, were osteogenic *in vivo* following three weeks of implantation. Quantitation of the radiographic images revealed that Col-HA scaffolds implanted immediately had a higher mean radiopacity than Col-HA scaffolds incubated overnight. Similarly, Col-HA scaffolds implanted immediately had higher mean area fractions of donor cells and mineralizing surfaces compared with Col-HA scaffolds incubated overnight. Healos groups implanted immediately had higher area fractions of donor cells compared with Healos scaffolds incubated overnight. The addition of BME gel did not exert a strong effect on the metrics examined here when cells were implanted immediately. However, the use of BME gel as a cell suspension, improved the donor cell distribution in the scaffold when an overnight incubation period was applied. When an *in vitro* test of cell delivery was performed using the Col-HA scaffolds, a higher cell loading was found for the immediate implantation method compared with overnight incubation, with or without BME gel. Due to potential cell loss during overnight incubation, immediate implantation following cell seeding may be a preferable method. These results should be useful when

deciding how to deliver cells to a bony defect for optimal cell-based bone tissue engineering.

# 6 Improving the permeability of lyophilized collagen-hydroxyapatite scaffolds for cell-based bone regeneration with a gelatin porogen

## 6.1 Introduction

Cell-based bone tissue engineering has shown encouraging results in animal models[64,65,164,172,197,198] and even in a few human patients[62,63]. This method could supplement or replace autologous bone as a bone grafting material, since progenitor cell harvesting would inflict far less damage to existing bone. However the factors that lead to successful healing of bony defects using cells are still poorly understood, and this approach has lagged behind growth factor based approaches.[66] Currently, high doses of growth factors are required for bone formation and negative side effects have been observed in some patients.[77,199,200] A cell-based approach (or combination of cells and factors) could theoretically sidestep issues of negative side effects and harness the ability of cells to secrete hundreds of different factors in concert with the healing cascade, yet challenges remain. One such challenge is the design of a biomaterial scaffold to deliver cells and support osteogenesis *in vivo*. So far, an ideal scaffold for bone tissue engineering has not been identified,[68] and specific scaffold designs may be required for healing bony defects depending on anatomical location, among other factors.

Collagen-calcium phosphate composite scaffolds are a class of bone-forming biomaterials that are easily remodeled by cell-secreted MMPs, contain ions for mineralization, and have already shown promise in the clinic with bone marrow extract.[201,202] While bone marrow contains an osteoprogenitor population, these cells are quite rare in the bone marrow population (0.001 to 0.01%).[37] Bone marrow osteoprogenitors can be greatly expanded in culture, improving the therapeutic potency when higher numbers of osteoprogenitors are seeded to a site of bone injury.[153] We have developed a collagen-hydroxyapatite (HA) scaffold that is osteogenic in preclinical *in vivo* models of cell-based bone repair with culture-expanded bone marrow osteoprogenitors.[89,92,182] However the cellular morphology of lyophilized collagen-based scaffolds can sometimes result in a relatively low permeability. We previously observed that collagen-HA scaffolds with a permeability of $10^{-12}$ $m^4/Ns$, despite large pores (>100 μm) and a high porosity (>90%), resulted in modest bone formation in a critical-size calvarial defect, owing to limited cellular invasion of the scaffolds (manuscript in preparation). The commercial scaffold used as a control in this experiment (Healos®) had a permeability of $10^{-8}$ $m^4/Ns$ and performed better in this *in vivo* test. Mitsak et al. demonstrated that polycaprolactone scaffolds produced by a 3D printing method with a permeability of $10^{-7}$ $m^4/Ns$ led to greater new bone infiltration *in vivo* than the same material with a permeability of $10^{-8}$ $m^4/Ns$. We therefore hypothesized that collagen-HA scaffolds with greater permeability would lead to better bone formation. Furthermore we investigated the use of a gelatin porogen to further increase the permeability of lyophilized collagen-HA scaffolds.

Since the pore structure of lyophilized collagen scaffolds is created by an ice template, it is difficult to apply a salt leaching technique[203] to improve permeability, owing to the fact that the salt would simply dissolve in the aqueous phase. Furthermore, since collagen denatures above 50 °C[204], in acidic conditions, and in a variety of chemical solvents, a sacrificial porogen phase would have to be removed under gentle temperature, pH, and solvent conditions. Han et al. developed a series of elegant porogen methods that fulfill these requirements, namely gelatin, hyaluronan, and alginate microparticles that can be removed by incubation at 37 °C, hyaluronidase, and EDTA addition, respectively.[205] Inspired by Han et al., we used gelatin microspheres as a nontoxic porogen to increase the permeability of lyophilized collagen-HA scaffolds, obtaining a 4-fold increase in permeability. We then sought to evaluate and compare the *in vivo* performance of improved permeability of scaffolds to that of the lower permeability found in our prior experiment (~$10^{-12}$ $m^4$/Ns) and scaffolds without the gelatin porogen (~$10^{-9}$ $m^4$/Ns). As discussed by Dias et al.,[206] permeability encapsulates a variety of scaffold architectural parameters; such as porosity, pore size, and interconnectivity. Furthermore, permeability is a functional mass transport property that has been correlated to bone formation *in vivo*.[196] Permeability can be implemented as an important quality control measure in the production of lyophilized collagen scaffolds. The effects of collagen-HA scaffold permeability on bone formation have not yet been well defined in the context of *in vivo* outcomes. Identifying reliable predictors of bone formation is a critical step towards consistent and effective cell-based bone regeneration.

## 6.2 Materials & Methods

### 6.2.1 Gelatin microbead fabrication

Gelatin microbeads were fabricated using an oil and water emulsion method.[205] First, type-A gelatin (Fisher) was added to distilled water at a concentration of 10 % (w/v) and autoclaved. Three mL of gelatin solution was added dropwise to 15 mL of 10% Tween 20 (Acros) in extra virgin olive oil at 40 °C with stirring at 700 rpm. The emulsion was held at 40 °C and 700 rpm for 10 minutes followed by reducing the stirring rate to 200 rpm and placing the solution in an ice bath for 30 minutes to gel the microbeads. To remove the olive oil from the gelatin microbeads, the emulsion was added to a centrifuge tube along with cold PBS and spun at 700 rpm for 5 min, removing the oil-water supernatant and repeating five times. Washed gelatin microbeads were kept in sterile PBS at 4 °C until use.

### 6.2.2 Scaffold fabrication and sterilization

Type-I collagen was first derived from rat tail tendons following Rajan et al.[154] A collagen-hydroxyapatite composite was formed by simultaneous self-assembly of collagen fibers in the presence of precipitating hydroxyapatite from a modified simulated body fluid (m-SBF).[188] Briefly, the collagen solution was adjusted to 2.5 mg/mL by a two-fold dilution in sterile ultrapure water at 4 °C. For a 200 mL solution of m-SBF, the following salts were added in the order they appear: 1.08 g NaCl, 0.1428 g $K_2PO_4$, 0.0622 g $MgCl_2$, 2.4 g HEPES, 0.1758 g $CaCl_2$, and 0.294 g $NaHCO_3$. While kept cold, the pH of the solution was adjusted to 7.0 with a sodium hydroxide solution and then transferred to a water bath at 40 °C for 24 hours to allow simultaneous precipitation of hydroxyapatite

and collagen fibrillogenesis. The gel-precipitate was centrifuged at 11,000 g and 4 °C for 12 min. The supernatant was discarded and the pellet was lyophilized (FreeZone 12L, Labconco). The collagen-HA precipitate was reconstituted with water at a concentration of 100 mg/mL and briefly homogenized (Tissuemiser, Fisher) to obtain a uniform slurry. Gelatin microbeads were added to the slurry at a ratio of 1:5, 1:1, and 1:0 collagen-HA:gelatin (w:w). To impart a porous structure, the slurries were frozen from room temperature to -40 °C at a cooling rate of -0.37 °C/min using a program implemented by the freeze dryer. Following drying, the scaffolds containing beads were placed in sterile PBS at 37 °C overnight to remove the gelatin porogen. To covalently crosslink the collagen fibers, scaffolds were immersed in a solution of 20 mg/mL EDC [1-ethyl-3-(3-dimethylaminopropyl) carbodiimide hydrochloride] for 24 hours at 4 °C. The scaffold was then rinsed in a solution of 5% (w/w) glycine in sterile water for an overnight period in order to block unreacted EDC. Crosslinking was followed by three sequential rinses in sterile water for 15 minutes each and a final rinse for three days at 4 °C. Finally, rinsed scaffolds were freeze-dried again, cut to a thickness of ~500 μm and punched into a diameter of 3.5 mm. Scaffolds were terminally sterilized with a 24-hour cycle of ethylene oxide gas (Anprolene AN74i, Anderson Products).

### 6.2.3 Micro computed tomography

Three-dimensional reconstructions of scaffolds were acquired using an Xradia MicroXCT-400. To enhance the contrast of collagen-HA scaffolds, they were soaked in 1% iodine in ethanol overnight and dried before tomography. 1,500 images were acquired at an angle of -91˚ to 91˚ with an exposure time of 10 s, a source power of 3 W, a voltage

of 40 kV, and a 20x objective. Tomography images were reconstructed with XM Reconstructor (Xradia) and viewed with the 3D viewer plugin for the FIJI distribution of NIH ImageJ.[142] Scaffold porosity, pore thickness, wall thickness, and anisotropy were calculated from tomography data using the BoneJ plugin for FIJI.[156]

### 6.2.4 Permeability Measurement

The permeability, k ($m^4$/Ns), of Healos® and Col-HA scaffolds was measured with water and a custom flow cell using the following equation found in reference [159]:

$$k = \frac{\Delta x}{A \cdot M_{B2}} \cdot \frac{2\pi^2 r^4}{(M_{B1}/M_{B2})^2 - 1}$$

where, $\Delta x$ = scaffold length (m), A = scaffold cross-sectional area ($m^2$), $M_{B1}$ = mass flow rate without scaffold (g/s), $M_{B2}$ = mass flow rate with scaffold (g/s), and r = radius of the outlet (m).

### 6.2.5 *In vitro* culture of bone marrow osteoprogenitors

Mouse bone marrow stromal cells (BMSCs) were isolated from the femur and tibia of Col3.6cyan CD1 transgenic mice (Fig. 6-1A). The Col3.6cyan reporter construct activates the production of cyan fluorescent protein when a cell expresses the type I collagen gene. The 3.6 kb fragment of the COL1A1 promoter region, implemented in the Col3.6cyan reporter, can be used as a marker for differentiated osteoblasts.[207] Bone marrow from the femur and tibia of Col3.6cyan transgenic mice was collected by a centrifugation method. First, interlocking filtration column and collection tubes, with the filters removed, were autoclaved. Femur and tibia were placed in the top tube and cells were spun at 3100 g for 2 minutes into the second tube containing 100 uL of 98% PBS, 2% FBS, and 2 mM EDTA (PFE) to prevent clotting. Bone marrow cells were flushed

through a 70 mm cell strainer (BD Biosciences) and re-suspended in α-MEM. Cells were then added to 100 mm culture dishes in warm α-MEM (Gibco) containing 10% fetal bovine serum and 1% penicillin-streptomycin. To allow hematopoietic cells to contribute to the expansion of osteoprogenitor cells, the culture medium was changed 4 days after seeding. On the day of implantation, adherent BMSCs were trypsinized and seeded dropwise onto the top the dry collagen-HA scaffold at a density of $1.0\times10^6$ cells in 15 μL of culture medium. Six cell-seeded scaffolds were implanted for each of three groups, Group N – collagen-HA no beads, Group 1:1 - 1:1 ColHA:Beads, and Group 1:5 – 1:5 ColHA:Beads (Fig. 6-1A).

### 6.2.6 *In vivo* critical-size mouse calvarial defect model

On the day of implantation, NOD *scid* gamma (NSG) immunodeficient host mice were anesthetized with a ketamine (135 mg/kg) – xylazine (15 mg/kg) blend. Two 3.5 mm diameter critical-size calvarial defects were made in the right and left parietal lobe using a bur trephine (RAL #229-030, Benco Dental). Extreme care was taken to prevent damage to the dura mater beneath the calvarium. Cell-seeded scaffolds were placed in each of the two defects per animal. Following closure of the scalp with resorbable sutures, animals were given postoperative analgesic (bupronephrine, 0.08 mg/kg). One day prior to euthanization at three weeks post-implantation, host NSG mice were injected intraperitoneally with calcein to mark surfaces of active mineralization. All procedures used in this study were approved by the UConn Health Center Institutional Animal Care and Use Committee (IACUC).

### 6.2.7 X-Ray, Histology and histomorphometry

After three weeks of implantation, animals were euthanized using $CO_2$ asphyxiation, and the extracted calvarium were fixed in 10% formalin overnight, followed by 30% sucrose solution overnight, while kept cold and in the dark. Radiographs of calvarium were acquired with a digital X-ray system (MX20, Faxitron). The samples were then prepared for histology by trimming the calvaria to the defect regions and embedding each sample in Cryomatrix (Thermo). Six sections were cut from each calvarium using a cryostat (Leica) and tape (Cryofilm Type2C, Section-Lab) to transfer sections to glass slides. All sections were imaged with a 10x objective on a fluorescent microscope (Axio Scan.Z1, Zeiss) equipped with stage automation for high throughput imaging (Zen software, Zeiss).

Bone formation was quantified from radiographic images by selecting a region of interest (ROI) surrounding the implant area, but excluding regions overlapping with host bone, and calculating the mean pixel intensity using FIJI.[142] To quantify the area fraction of donor cells, calcein label, nuclei, and DIC signal from histological sections, an ROI outlining the defect area was manually drawn for each image and saved using FIJI. A threshold was then applied to each channel, and the area fraction of the total defect area was calculated. To process the images as a batch and ensure the same threshold was consistently applied, a macro was written for FIJI that sequentially processed images using their corresponding ROIs. Nuclei embedded in bone were classified as such if they were found within the DIC signal. This was calculated using the 'AND' image processing calculation between the nuclei and DIC channels. Areas where donor cells and mineralization label were in close proximity (indicative of active donor mineralization)

were found by an 8× dilation of each channel followed by the 'AND' operation to find areas of overlap.

### 6.2.8 Statistical analysis

A two-sample independent t-test was used to determine significance between groups. P-values less than 0.05 (both tails) were considered statistically significant and are indicated with an asterisk. P values less than 0.01, 0.001, and 0.0001 were indicated with two, three, and four asterisks, respectively. The complete histomorphometry dataset was organized by a hierarchical clustering algorithm (complete linkage method with Euclidean distance measure) and plotted using the R statistical programming package.[208]

## 6.3 Results

### 6.3.1 Scaffold architecture

To examine the influence of scaffold permeability on bone formation, we fabricated three types of scaffolds; two containing a 1:1 and 1:5 ratio (w:w) of collagen-HA precipitate to gelatin bead porogen (Fig. 6-1E and 6-1F, respectively), and another scaffold without a bead porogen (herein termed N for normal, Fig. 6-1D). The gelatin bead porogen had an average diameter of 25.10±15.97 μm (Fig. 6-1C). Removing the porogen led to samples with an average permeability 4-fold higher than the samples without porogen (Fig. 6-1B and Table 3). Increasing the bead content 5-fold did not further increase the scaffold permeability. Cross-sections of each scaffold type are shown in Fig. 6-1. All the scaffolds had a cellular architecture (Fig. 6-1) when viewed in cross-section. It can be difficult to appreciate the morphology of the collagen-HA scaffolds by SEM alone since the cutting procedure can flatten the structure (Fig. 6-1E). To non-invasively examine the scaffold morphology in three dimensions, we performed x-ray microtomography.

Three-dimensional reconstructions of the scaffolds (Fig. 6-2A through 6-2C) were analyzed to examine the pore morphology of the void space. A sphere-filling algorithm was used to describe the void space according to the size of sphere that fit within its bounds. A higher grayscale value (more white) indicates a larger sphere diameter (Fig. 6-2D through 6-2E). A slight increase in porosity and mean pore size was observed for samples in which the bead porogen was applied (Fig. 6-2G and Table 3). The fraction of pores greater than 90 μm increased in both bead porogen samples (Fig. 6-2G). The scaffold wall thickness remains essentially the same, approximately 5 μm. When comparing the values of structural anisotropy, all scaffolds are randomly organized, with slightly more anisotropy in the bead-loaded samples. Taken together, the bead porogen appeared to increase the fraction of larger pores and the randomness of the scaffold architecture.

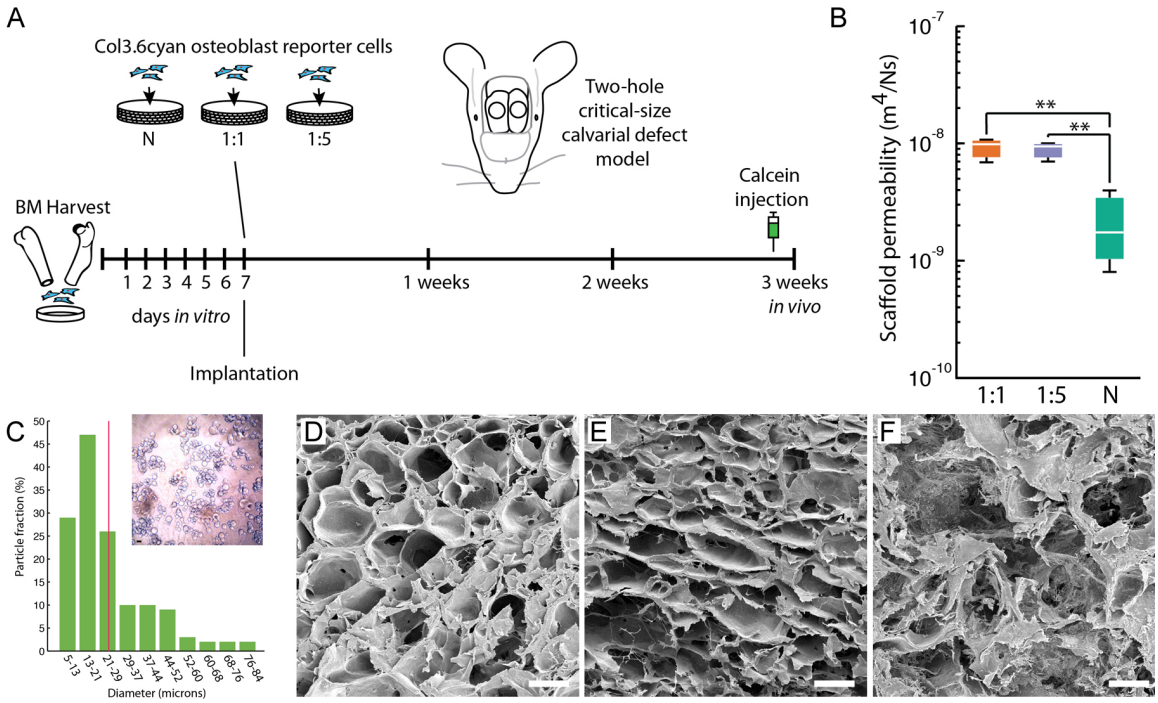


**Figure 6-1 | Experimental design and enhanced scaffold permeability using a gelatin porogen.** (A) Schematic of the *in vivo* experiment. (B) Measurement of scaffold permeability for each of the *in vivo* groups, log scale. (C) Particle size distribution of the gelatin microbead porogen used. (inset) Micrograph of the gelatin microbeads. Electron micrographs of scaffolds fabricated without the gelatin bead porogen, group N (D), and with the porogen, group 1:1 (E) and 1:5, (F). Scale bars in (D)-(F) are 100 µm.

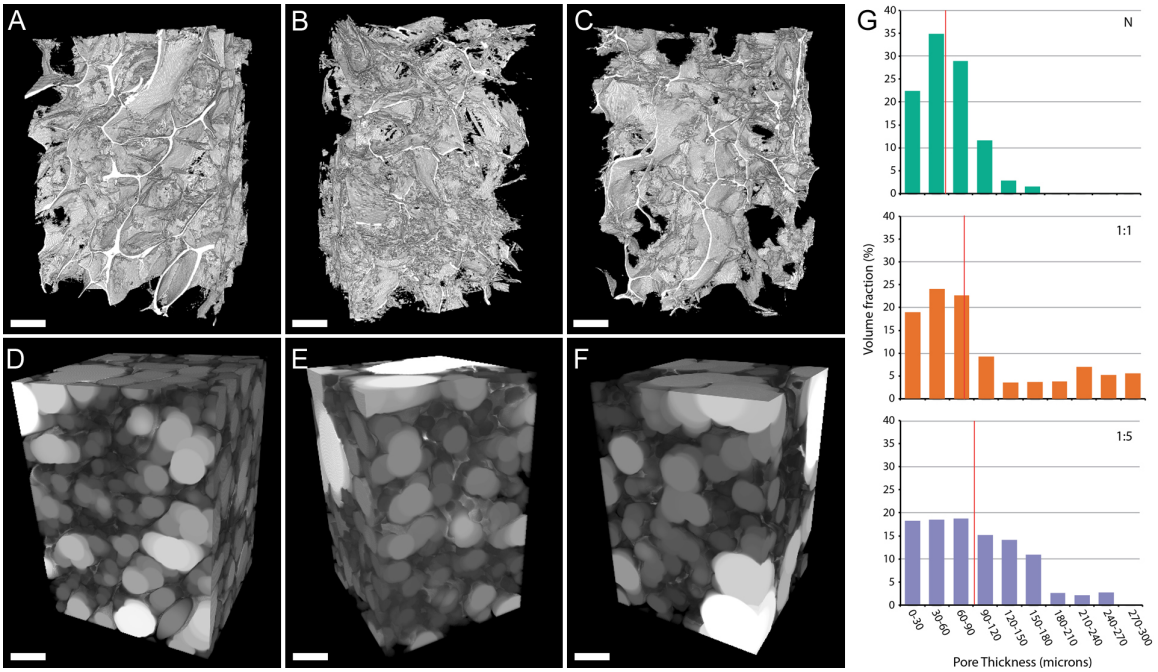


**Figure 6-2| Three-dimensional reconstructions of scaffolds and pore volumes coded according to pore size.** 3D reconstructions from tomography data for the (A) N, (B) 1:1,

and (C) 1:5 scaffolds. All scale bars 100 μm. Color-coded pore volumes of (D) N, (E) 1:1, and (F) 1:5 scaffolds after a sphere-filling algorithm. Pore volumes are shown from the approximately the same perspective as the scaffold volumes above. (G) Pore thickness distributions from the tomography data. Red bar in (G) shows the mean pore thickness.

| Sample | Porosity | Mean Pore Thickness (μm) | Mean Wall thickness (μm) | Mean Permeability ($m^4$/Ns) | Scaffold Anisotropy |
|---|---|---|---|---|---|
| N | 91.81 | 58±32 | 5.91±3.3 | $2.17\pm1.63\times10^{-9}$ | 0.50815 |
| 1:1 | 95.25 | 79±60 | 5.16±2.3 | $9.16\pm2.01\times10^{-9}$ | 0.39975 |
| 1:5 | 93.59 | 91±59 | 4.89±2.1 | $8.8\pm1.59\times10^{-9}$ | 0.44242 |

**Table 3 | 3D architectural parameters from tomography data and scaffold permeability.** The value of the anisotropy parameter tends toward zero for randomly oriented structures and to one for parallel flat plates.

### 6.3.2 Radiographic examination of implants after three weeks *in vivo*

Six scaffolds from each of the three scaffold types (N, 1:1, 1:5) were combined with culture-expanded bone marrow cells and implanted into critical-size calvarial defects of immunodeficient mice. Two of the animals in this study showed signs of disease and were excluded from the quantitative analysis herein based on their health (calvaria from these animals are shown in 6-3F and 6-3I). Three weeks after implantation all mice were euthanized and their calvaria were harvested for examination, first by stereomicroscopy and radiography. When viewed on the stereomicroscope, some implants were very opaque when illuminated from behind, most notably Fig. 6-3A, 6-3E, and 6-3G, insets. Blood vessels were also visible on the surface of the implants in all cases. Movement of the scaffolds following implantation was apparent in several samples (Fig. 6-3A, 6-3B, 6-3C, 6-3E, 6-3F, and 6-3H). When the radiographs were viewed, all samples contained regions of high relative radiopacity, indicative of mineralized tissue. When the photomicrographs were quantitatively compared, the 1:1 group had a significantly higher mean gray value in the defect compared to the N group. To evaluate the status of the

seeded donor cells, and to confirm scaffold mineralization, the calvarial implants were sectioned and viewed with brightfield (Fig. 6-5) and fluorescence (Fig. 6-6) microscopy.

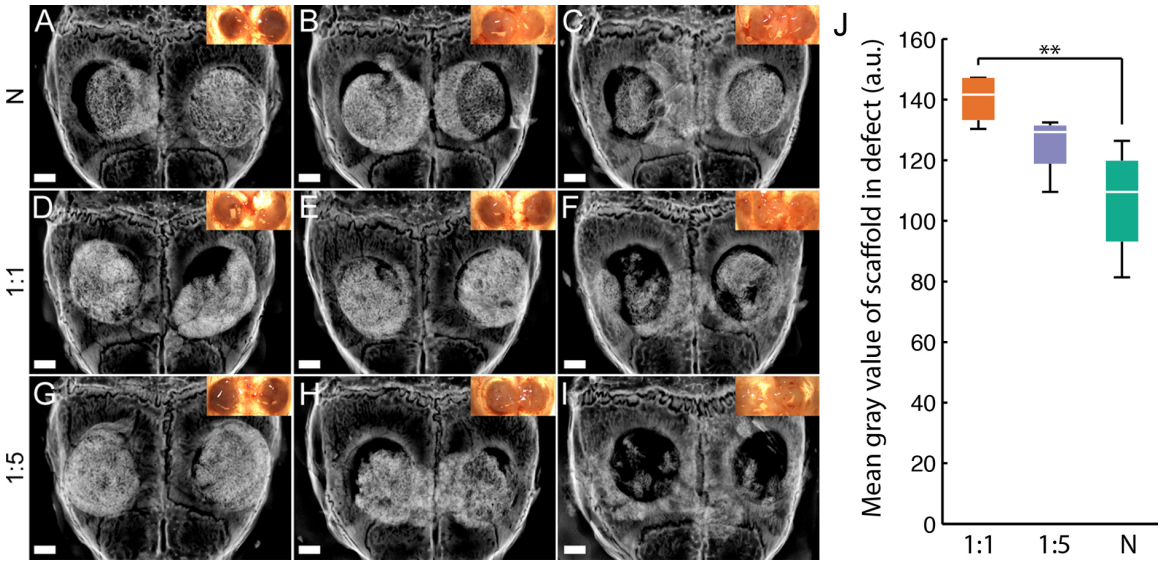


**Figure 6-3 | Radiographs of implants following three weeks *in vivo*.** (A)-(I) X-ray micrographs of calvarial defects filled with collagen-HA scaffolds seeded with culture-expanded BMSCs. Insets are photographs of the defects. All scale bars are 1 mm. (J) Quantitation of radiopacity in the implant region.

### 6.3.3 Histological evaluation of implants after three weeks *in vivo*

Upon examination of histological sections from each group stained with hematoxylin and eosin, it was apparent that the signal observed from the radiographs was due to mineralized tissue (deep purple and red asterisks, Fig. 6-5A, 6-5C, and 6-5E). A layer of matrix and cells was also visible on the top and bottom of the implants, which was in some cases thickened at the margins of the implant (Fig. 6-5A and 6-5E, black arrows). Marrow cells were found in the defect interiors, suggesting the establishment or development of a new marrow niche (Fig. 6-5B and 6-5D, red pound signs). All scaffolds contained a high cell density and the porogen scaffolds were particularly dense with very little unfilled space. Blood vessels could also be seen at the bottom of the defect,

suggesting a vascular contribution from the dura mater (Fig. 6-5F, green arrows). Dense aggregates of red blood cells are visible in center of the sample pictured in Figs. 6-5C and 6-5D (green triangles), potentially remnants of clots that formed within the scaffold.

To evaluate the persistence and activity of donor cells and the intravenous mineralization label, fluorescent images were evaluated (Fig. 6-6). From this perspective, it was clear that donor cells had differentiated into osteoblasts, indicated by expression of the Col3.6cyan reporter gene, which was not active following six days of culture (Fig. 6-4).

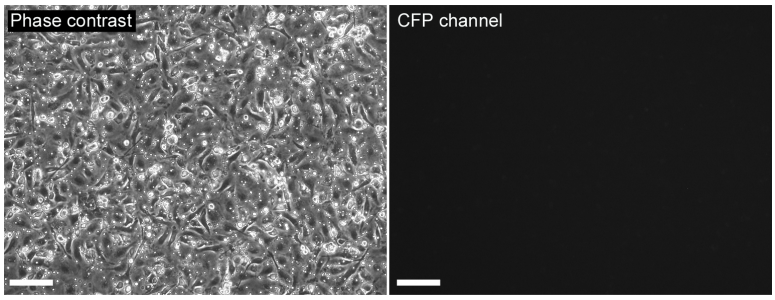


**Figure 6-4 | Col3.6cyan osteoblast reporter is not active following six days of expansion in vitro.** Scale bar is 100 μm.

Donor osteoblast cells (cyan) appeared well distributed throughout the thickness of the scaffolds, as well as the calcein mineralization label given one day prior to euthanization. Several sites of active donor cell mineralization were apparent, indicated by cyan cells in close proximity to the green calcein mineralization label (Fig. 6-6B, 6-6D and 6-6F, yellow arrows). Hoechst staining of cell nuclei (Fig. 6-6, red) showed a high number cells located throughout the defects. Nuclei were present embedded in the mineral phase in several locations, suggesting new bone had formed, rather than misinterpreting the collagen-HA scaffold for new bone. The mineralized implants were integrated to host

bone in some areas (Fig. 6-6, white arrows). Taken together, the histological sections show that samples in each group contained new bone, were actively mineralizing further, and contained a high cell density. Furthermore, donor cells had survived implantation and had differentiated into bone forming osteoblasts that localized to mineralizing surfaces.

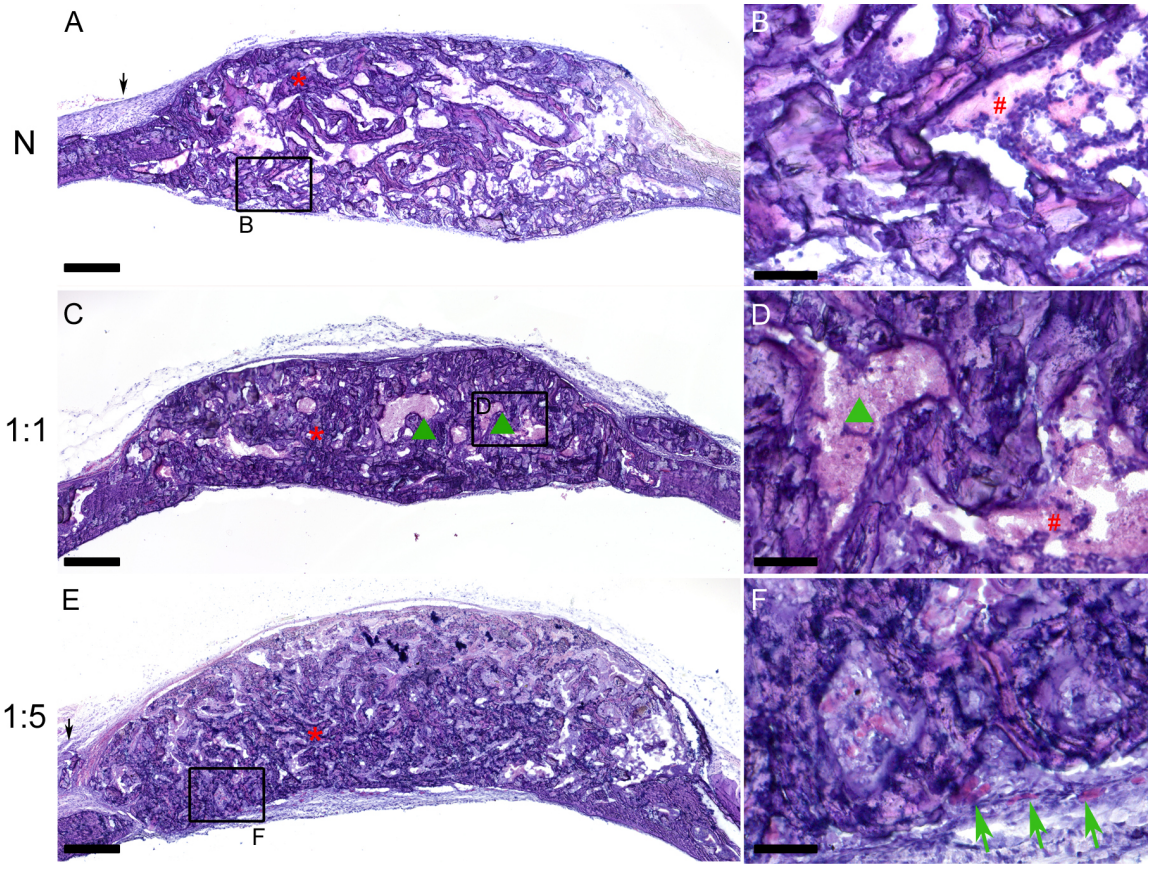


**Figure 6-5 | Histological sections of implants stained with hematoxylin and eosin.** Representative images of implants from each group (A)(C)(E) and higher magnifications (B)(D)(F). Black arrows in (A) and (E) indicate periostieal membrane thickening at defect margins. Red astericks in (A),(C), and (E) mark bone. Green triangles in (C) and (D) show red blood cells and bone marrow cells, red pound signs in (B) and (E). Blood vessels can be seen in (F), green arrows. Scale bars at left are 500 μm and 100 μm at right.

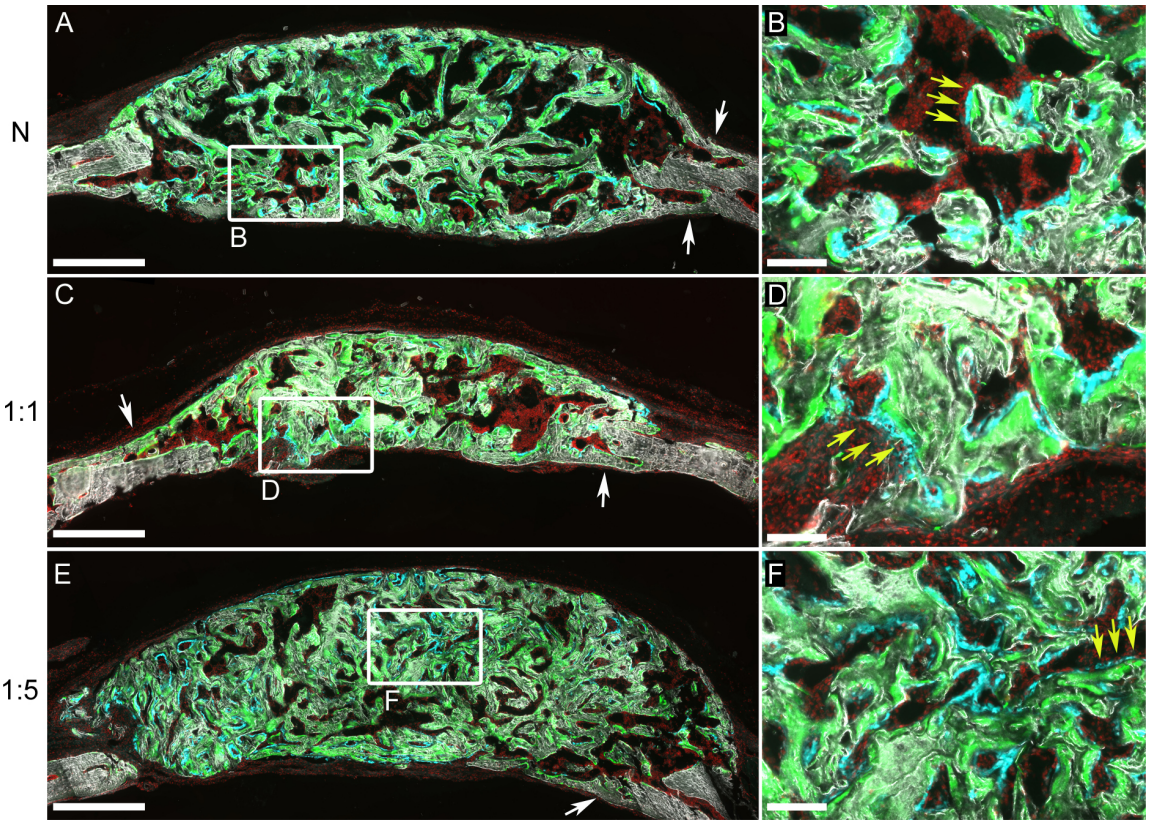


**Figure 6-6 | Fluorescence microscopy of histological sections showing donor cells and mineralization label.** Representative images of histological sections from each group showing donor osteoblast cells (cyan), calcein mineralization label (green), hoescht-labelled nuclei (red), and DIC channel (gray). White arrows in (A), (C), and (E) indicate areas of implant integration with the host bone. Yellow areas in magnified images at right show donor osteoblast cells overlying the calcein mineralization label. Scale bars are 500 μm at left and 100 μm at right.

### 6.3.4 Quantitative histomorphometry of implants after three weeks *in vivo*

To quantitatively compare the osteogenic potential of each group, a histomorphometric analysis of tissue sections was performed. Six metrics were evaluated for each of the replicate serial sections from one of the 18 defects, resulting in a total of 106 images. Four of the metrics were area fractions within the defect area of each of the four channels acquired during fluorescence imaging (DIC.AF-bone and scaffold, HOESCHT.AF-cell nuclei, CALCEIN.AF-mineralization label, and CFP.AF-donor osteoblast cell area fractions). Two additional metrics were calculated to capture the bone forming activity

and a measure of the new bone formed. Since it can be difficult to distinguish scaffold from new bone based on the DIC channel alone, we counted the area fraction of cell nuclei embedded in the DIC signal, indicative of cells trapped in newly formed bone (Fig. 6-7B). This metric was termed the 'area fraction of embedded nuclei' and appears on the plot in Fig. 6-7A as the HOESCT.DIC area fraction (H.D.AF). To estimate the bone forming activity by donor cells, we classified and counted regions where donor osteoblasts were overlying a strong mineralization label (Fig. 6-7E, with and without a red overlay showing a classified mineralization site). This metric was termed 'active mineralization sites' and appears in the plot in Fig. 6-7A as the CALCEIN.CFP area fraction (CAL.CFP.AF).

Following image processing, a hierarchical clustering algorithm was applied to the complete dataset (Fig. 6-7A). Each image (named at right, Fig. 6-7A) was classified according to its similarity to the other images based on the six metrics calculated (named at bottom). The clustered dataset showed four groups at the $2^{nd}$ clade-level that corresponded with the quality of the repair. The top group (clade α) contained images of qualitatively good mineralizing defects with high area fractions of the DIC, nuclei and donor cell signal. Correspondingly, this group had high numbers of embedded nuclei and active bone mineralization sites. A sample image from this group is shown in Fig 6-8A. By contrast, at the bottom of this dataset, the clade δ group contained images of qualitatively poorly mineralized defects with low area fractions of mineralization label, embedded nuclei and donor cells overlying the mineralization label. A representative image from the clade δ group is included in Fig. 6-8B. The intermediate groups (clade γ

and β) contained defects that scored within these bounds. The clustered data suggests that the combination of metrics used here can distinguish between qualitatively good and bad bone repairs in this experiment. Viewing the spread of values for the area fractions of donor cell mineralization, embedded nuclei and donor cells indicates a consistent change across the images analyzed, suggesting these parameters of the six may provide a stronger resolving power to discriminate differences between implant images.

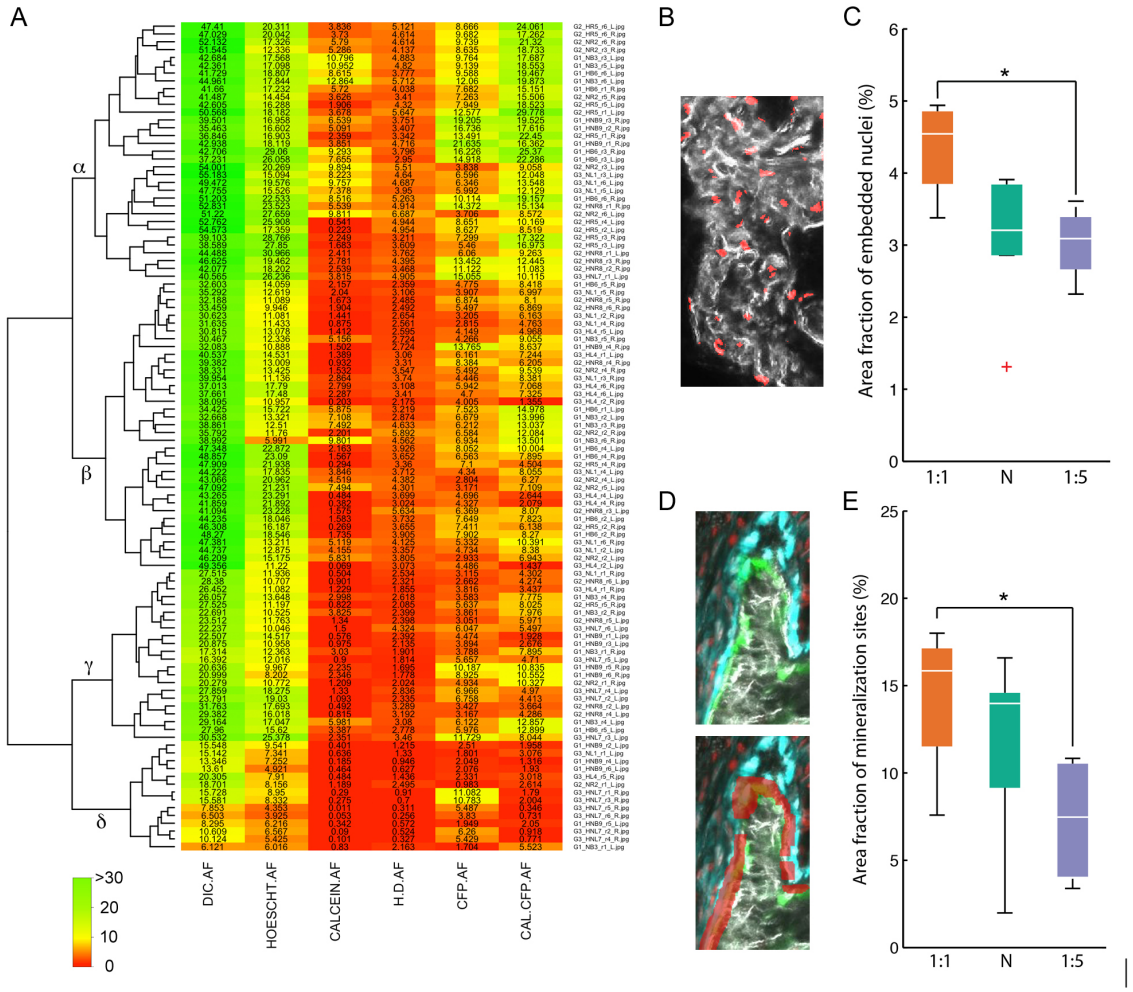


**Figure 6-7 | Quantitative histomorphometry of images acquired by fluoresce microscopy.** (A) Hierarchical clustering of histomorphometry dataset. Rightmost column names each of the 106 images classified according to the similarity of the six analyzed metrics listed on the y-axis. (B) Example image of embedded nuclei classified according the analysis herein. (C) Comparison of the area fraction of embedded nuclei between groups. (D) Example image of a region containing donor cells overlying the green

mineralization label, presented with the classification output as a red overlay in the bottom image. (E) Comparison of the area fraction of mineralization sites between the two groups.

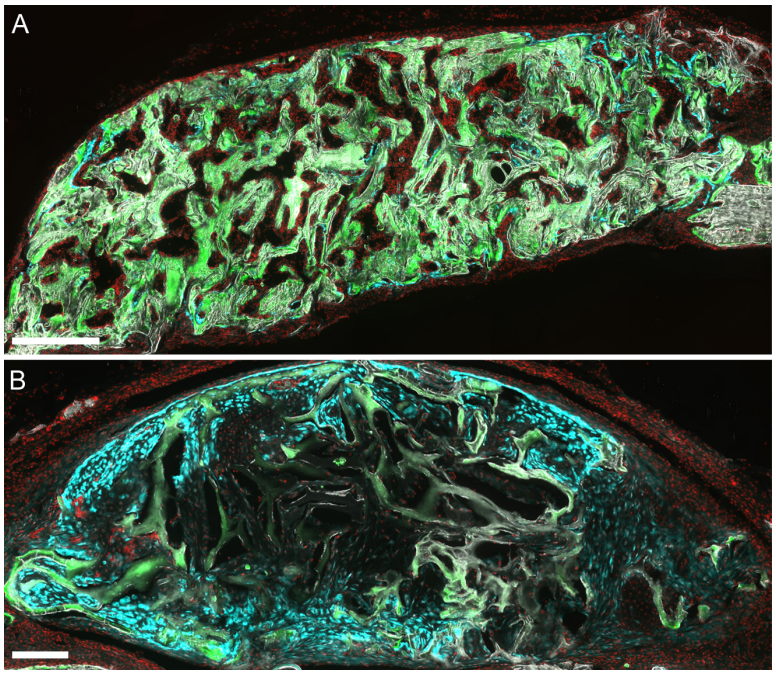


**Figure 6-8 | Representative images from (A) group α (good bone formation) and (B) group δ (poor bone formation) from hierarchical clustering.** Composite image of donor cells (cyan), calcein mineralization label (green), hoescht-labeled nuclei (red), and DIC channel (gray). Scale bars are 200 μm.

When the area fraction of embedded nuclei was compared between each experimental group, the 1:1 samples had the highest mean value, followed by the N and 1:1 group. The 1:1 group had a significantly higher fraction of embedded nuclei than the 1:5 group. While close to reaching significance ($p$=0.0702) at the 95% confidence level, the mean area fraction of embedded nuclei was not significantly different here between the 1:1 and N groups. Comparing the area fraction of mineralization sites, the same trend was observed; the highest mean value was found for the 1:1 group followed by the N and 1:5 groups, respectively. The histomorphometry results suggest that the 1:1 group performed

better than the 1:5 group, however the difference between samples with and without beads was not statistically significant here.

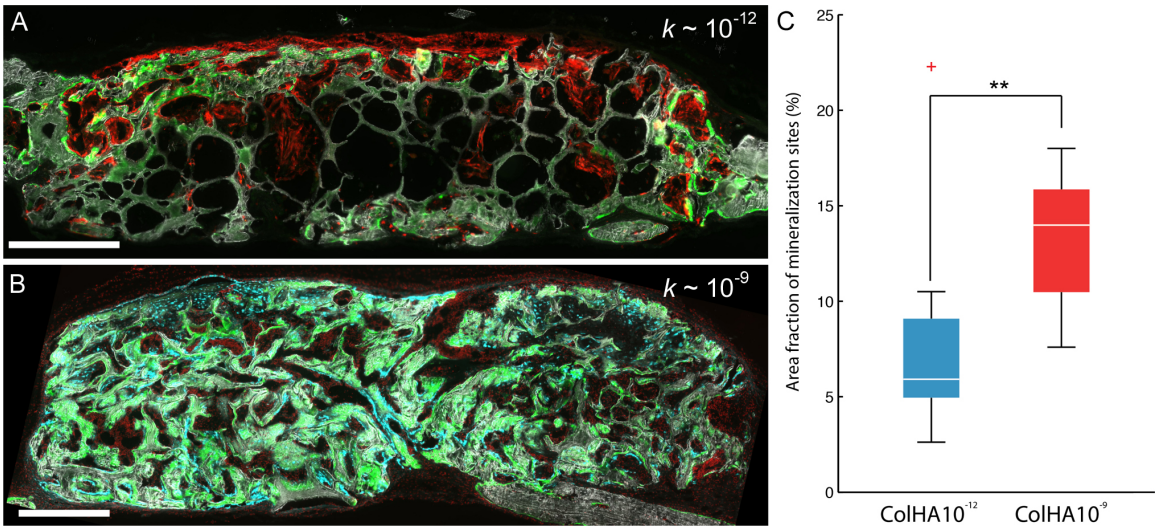


**Figure 6-9 | Comparison of scaffold mineralization of current experiment to historical data.** (A) Representative fluorescence micrograph showing donor cells (red), calcein mineralization label (green), and DIC channel (gray) of scaffold with a permeability of ~$10^{-12}$ $m^4$/Ns following three weeks of implantation in a calvarial defect. (B) Representative fluorescence micrograph showing donor cells (cyan), calcein mineralization label (green), hoescht-labeled nuclei (red), and DIC channel (gray) of scaffold with a permeability of ~$10^{-9}$ $m^4$/Ns following three weeks of implantation in a calvarial defect. All scale bars are 500 μm. (C) Comparison of the area fraction of mineralization sites between the low and high permeability scaffolds.

To help understand the experiment motivating this work, wherein bone formation was more limited and to evaluate a larger difference in scaffold permeability, we compared the area fraction of mineralization sites of samples examined here (Fig. 6-9B) to the historical dataset (Fig. 6-9A). The scaffolds used here have a mean permeability on the order of $10^{-9}$ $m^4$/Ns, resulting in a 1,000-fold increase when compared to those previously tested (~ $10^{-12}$ $m^4$/Ns). When the area fraction of mineralization sites was compared, a significant increase in active mineralization sites was observed for the current experiment

(Fig. 6-9C), further suggesting that a permeability of $10^{-12}$ $m^4/Ns$ is likely too low for optimal bone formation for this class of biomaterials.

## 6.4 Discussion

We wondered if (i) poor scaffold permeability led to suboptimal bone formation in a previous experiment, (ii) if the permeability of collagen-HA scaffolds could be enhanced via a nontoxic method, and (iii) if such a permeability enhancement would improve bone formation *in vivo*. The outcome of the experiment provides evidence to suggest that poor permeability is likely the cause of suboptimal bone formation observed previously (Fig. 6-9). Furthermore, we have shown that it is possible to increase the permeability of collagen-HA scaffolds with a nontoxic gelatin microbead porogen (Fig. 6-1). Increasing the bead loading from a 1:1 to 1:5 ratio of collagen-HA solids to gelatin porogen did not significantly increase scaffold permeability. When collagen-HA scaffolds of different permeability were compared, the quantitative analysis radiographic images suggest that the 1:1 bead loaded group performed better than the N group without beads (Fig. 6-3). However, the 1:5 and N group were not significantly different from each other here. This may be due to the small number of animals examined per group. Alternatively, it is tempting to speculate that the higher bead loading in the 1:5 group led to a mechanically weaker scaffold that compressed under the skin after implantation, reducing the effective scaffold permeability. Further *in vivo* testing should be undertaken to evaluate collagen-HA scaffold permeability above $10^{-9}$ $m^4/Ns$ and to define the optimal range of scaffold permeability for the type of bony defect. For instance, Mitsak et al. observed an improvement in the *in vivo* performance of PCL scaffolds seeded with BMP-7 transduced

human fibroblasts with a permeability of $7\times10^{-8}$ $m^4/Ns$ versus $4\times10^{-7}$ $m^4/Ns$ (5.8-fold difference) when implanted subcutaneously in a mouse model.[196] Additionally, the scaffold cylinder used by Mitsak *et al.* was approximately 3.6-fold larger by volume than evaluated here, which provides a larger range for evaluating cell invasion and bone infiltration. O'Brien et al., found the permeability of lyophilized collagen-GAG scaffold to be on the order of $10^{-11}$ to $10^{-10}$ $m^4/Ns$.[209] Similarly, we observed good bone formation *in vivo* in a calvarial defect model using collagen-HA scaffolds with permeability on the order of $10^{-10}$ $m^4/Ns$ combined with culture expanded mouse bone marrow cells, although these scaffolds were relatively thin (~300 microns).[182] We also found the permeability of the collagen-HA scaffold Healos® to be $\sim10^{-8}$ $m^4/Ns$ and have observed good bone formation *in vivo* using this material.[182] By contrast, collagen-HA scaffolds with a permeability of $\sim10^{-12}$ $m^4/Ns$ led to limited cell invasion and modest bone formation restricted to the scaffold perimeter (Fig. 6-9A). Grimm and Williams found the permeability of trabecular bone to be on the order of $10^{-10}$ to $10^{-9}$ $m^2$ ($10^{-7}$ to $10^{-6}$ $m^4/Ns$).[210] The permeability of human trabecular bone serves as a useful reference, although may not be the definitive optimum for tissue engineering scaffolds. Pannella *et al*. have recommended standardization among permeability measurements and provide a useful table of permeability values for different scaffold materials and measurement techniques.[211] Determination of the maximum collagen-HA scaffold permeability for bone formation *in vivo* should help define the optimal scaffold design for cell-based bone tissue engineering.

Image processing provides a relatively quick and high throughput method to compare the performance of cells and biomaterials *in vivo.* A direct measurement of new bone formation would be useful when comparing the performance of collagen-HA scaffolds. However this is difficult in practice because the biomimetic collagen-HA scaffold sometimes appears similar to bone. The two metrics used here, embedded nuclei and colocalization of donor cells to mineralization label (Fig. 6-7B and 6-7D), provide a useful means to characterize new bone formation following a rule-based methodology despite this difficulty. In the future, collagen-HA scaffolds could be fluorescently stained prior to the experiment so that any scaffold could be easily distinguished from new bone. This approach might be particularly useful in a longer-term scaffold degradation study.

Bone tissue engineering scaffolds are often described by morphological parameters such as porosity, pore size, and interconnectivity. Various efforts have been made to describe the optimal scaffold design based on morphological parameters. Permeability is a physical property of a material that can be used to theoretically model the mass transport within a porous medium. In effect, permeability encapsulates the combined influence of interconnectivity, pore size, porosity, tortuosity, and anisotropy on the mass transport within a porous material. The results of this experiment help to delineate the values of collagen-HA scaffold permeability that will result in success or failure *in vivo*. We have also demonstrated the use of a nontoxic porogen to improve the permeability of lyophilized collagen-HA scaffolds. Identification of the parameters that most strongly influence *in vivo* performance and can be identified prior to implantation will improve the efficacy and consistency of bone tissue engineering scaffolds.

## 6.5 Conclusion

Motivated by the suboptimal *in vivo* performance of a batch of collagen-HA scaffolds, the relationship between collagen-HA scaffold permeability and bone formation *in vivo* was investigated. Three types of scaffolds were fabricated; two scaffolds fabricated using a sacrificial gelatin bead porogen ($k$=9.16±2.01×10$^{-9}$ and 8.8±1.59×10$^{-9}$ m$^4$/Ns) and one scaffold without porogen ($k$=2.17±1.63×10$^{-9}$ m$^4$/Ns). The 1:1 bead-porogen implants had a significantly greater mean radiopacity compared to the normal (N) group following three weeks of implantation in a critical-size calvarial defect model. Quantitative histomorphometry showed higher mean embedded nuclei and active mineralization sites for the 1:1 versus N group, however this was not statistically significant here. Taken together the x-ray and histomorphometry data suggest a 1:1 ratio of collagen-HA solids to porogen, corresponding to a 4-fold increase in permeability, may improve early (<3 weeks) bone formation *in vivo*. Comparing the histomorphometry and permeability data herein to the prior experiment motivating this work, bone formation was significantly improved when scaffold permeability was ~10$^{-9}$ rather than ~10$^{-12}$ m$^4$/Ns. This result provides evidence that low permeability is a likely mechanism behind modest bone formation in the prior study. Furthermore, we have demonstrated the use of a nontoxic method for improving the permeability of lyophilized collagen-HA scaffolds. Permeability is a mass transport parameter that effectively encapsulates morphological parameters such as porosity, pore size, and interconnectivity; and correlates with bone formation *in vivo*. Furthermore, the measurement of scaffold permeability before implantation *in vivo* can be a critical quality control parameter to ensure consistent and effective bone formation with lyophilized scaffolds and osteoprogenitor cells.

# 7 Conclusions and Future Work

## 7.1 Conclusions

### 7.1.1 Development of a live animal imaging platform

Tissue-engineering therapies have shown early success in the clinic, however, the cell–biomaterial interactions that result in successful outcomes are not yet well understood and are difficult to observe. Here we describe a method for visualizing bone formation within a tissue-engineered construct *in vivo*, at a single-cell resolution, and *in situ* in three dimensions using two-photon microscopy. First, two-photon microscopy and histological perspectives were spatially linked using fluorescent reporters for cells in the skeletal lineage. In the process, the tissue microenvironment that precedes a repair-focused study was described. The distribution and organization of type I collagen in the calvarial microenvironment was also described using its second harmonic signal. Second, this platform was used to observe *in vivo*, for the first time, host cells, donor cells, scaffolds, and new bone formation within cell-seeded constructs in a bone defect. We examined constructs during bone repair four and six weeks after implantation. New bone formed on the scaffolds, primarily by donor cells. Host cells formed a new periosteal layer that covered the implant. Scaffold resorption appeared to be site-specific, where areas near the top were removed and deeper areas were completely embedded in new mineral. Visualizing the *in vivo* progression of the cell and scaffold microenvironment should contribute to our understanding of tissue-engineered regeneration and lead to the

development of more streamlined and therapeutically powerful approaches.

### 7.1.2 Consistent bone formation with collagen-hydroxyapatite scaffolds

Osteoprogenitor cells combined with supportive biomaterials represent a promising approach to advance the standard of care for bone grafting procedures. However, this approach faces challenges, including inconsistent bone formation, cell survival in the implant, and appropriate biomaterial degradation. We have developed a collagen-hydroxyapatite (HA) scaffold that supports consistent osteogenesis by donor-derived osteoprogenitors, and degrades faster than a pure hydroxyapatite scaffold. Herein, the material properties are characterized as well as cell attachment, viability, and progenitor distribution *in vitro*. Furthermore, we examined the biological performance *in vivo* in a critical-size mouse calvarial defect. To aid in the evaluation of the in-house collagen–HA scaffold, the *in vivo* performance was compared with a commercial collagen–HA scaffold (Healo®, Depuy). The in-house collagen–HA scaffold supported consistent bone formation by predominantly donor-derived osteoblasts, nearly completely filling a 3.5 mm calvarial defect with bone in all samples (n=5) after three weeks of implantation. In terms of bone formation and donor cell retention at three weeks post implantation, no statistical difference was found between the in-house and commercial scaffold following quantitative histomorphometry. The collagen–HA scaffold presented here is an open and well-defined platform that supports robust bone formation and should facilitate the further development of collagen–hydroxyapatite biomaterials for bone tissue engineering.

### 7.1.3 Optimizing cell delivery to calvarial defects

Cell-based tissue engineering can be used to replace missing or damaged bone, but the optimal methods for delivering therapeutic cells to a bony defect have not yet been established. Using transgenic reporter cells as a donor source, two different collagen-hydroxyapatite scaffolds, and a critical-size calvarial defect model, we investigated the effect of a cell-attachment period prior to implantation, with or without an extracellular matrix-based seeding suspension, on cell engraftment and osteogenesis. When quantitatively compared, the in-house scaffold implanted immediately had a higher mean radiopacity than in-house scaffolds incubated overnight. Both scaffold types implanted immediately had significantly higher area fractions of donor cells, while the in-house collagen scaffolds implanted immediately had higher area fractions of the mineralization label compared with groups incubated overnight. When the cell loading was compared *in vitro* for each delivery method using the in-house scaffold, immediate loading led to higher numbers of delivered cells. Immediate loading may be preferable in order to avoid cell loss during overnight incubation. The use of a secondary ECM carrier improved the distribution of donor cells only when a pre-attachment period was applied. These results improve our understanding of cell delivery to bony defects in the context of *in vivo* outcomes.

### 7.1.4 Examining the permeability of collagen-hydroxyapatite scaffolds

Bone tissue engineering using biomaterial scaffolds and culture-expanded osteoprogenitor cells has been demonstrated in several studies, however is not yet a clinical reality. One challenge is the optimal design of scaffolds for cell delivery, and the

identification of scaffold parameters that can delineate success and failure *in vivo*. Motivated by a previous experiment in which a batch of lyophilized collagen-HA scaffolds displayed modest bone formation *in vivo,* despite having large pores and high porosity, we began to investigate the effect of scaffold permeability on bone formation. Herein we fabricated scaffolds with a permeability of $2.17\pm1.63\times10^{-9}$ $m^4/Ns$ and 4-fold higher using a sacrificial gelatin porogen at a 1:1 and 1:5 weight ratio of solids to porogen. Scaffolds were seeded with mouse bone marrow stromal cells carrying a fluorescent reporter for osteoblast differentiation and implanted into critical-size calvarial defects in immunodeficient mice. Following euthanization three weeks later, bone formation was present in all implants. The porogen scaffold group containing a 1:1 ratio of solids to beads was significantly more radiopaque than the scaffold group without the bead porogen. Quantitative histomorphometry uncovered the same trend between the 1:1 group and scaffolds without the bead porogen found in the radiographic data, however this was not statistically significant here. Taken together, the x-ray and histology suggest that the 1:1 ratio of porogen to scaffold solids, resulting in a 4-fold increase in permeability, may enhance bone formation when compared to scaffolds without porogen. Interestingly, the 1:5 group did not perform as well as the 1:1 group. When the same histomorphometry analysis was applied to the experiment motivating this work, scaffolds with a permeability of $\sim10^{-9}$ $m^4/Ns$ compared with $\sim10^{-12}$ $m^4/Ns$ proved to form significantly more bone after 3 weeks *in vivo*. Scaffold permeability can be a useful quality control measure prior to implantation and this practice should improve the consistency and efficacy of cell-based bone tissue engineering.

## 7.2 Future work

### 7.2.1 Extending the limit of 2-photon imaging depth

This work found a maximum imaging depth of roughly 200 μm in calvarial bone using 2-photon microscopy. Imaging depth by 2-photon microscopy has been increased by others following two different approaches; tissue clearing[212] and serial 2-photon tomography[213]. I have evaluated both of these methods with promising results. Simply put, imaging depth is limited in 2-photon microscopy by light scattering. Tissue clearing is a method that reduces the scattering in tissues by replacing the water (refractive index of 1.33) found within the tissue with a liquid of a similar refractive index to the proteins (~1.5) that make up most of the tissue. Treatment of a calvarium with a 1:2 solution of benzyl alcohol and benzyl benzoate (BABB)[212] yielded transparent bone (Fig. 7-1A), and enabled second harmonic imaging completely through a mouse calvaria (Fig. 7-1B). However this method proved incompatible with transgenic reporters due to degradation of the GFP signal in BABB. By contrast, treatment of calvaria with ClearT2[214] (1:1 (40% PEG 8000 in water):(99% Formamide)), enabled deeper imaging in calvarial bone and retained a strong GFP signal (Fig. 7-1C). Alternatively, tissue samples of an arbitrarily large size can be serially imaged by 2-photon microscopy and later reconstructed.[213] A decalcified long bone of a triple transgenic mouse (OC-YFP, COL1A1-CFP, COL10-mCherry) was imaged by TissueVision, Inc (Cambridge, MA) and reconstructed in three dimensions (Fig. 7-1F and 7-1G). Large-scale three-dimensional reconstructions of bone repairs containing fluorescent reporters should provide researchers with a new perspective and lead to new observations. One example is when Dr. Achint Utreja and I imaged the curved surface of the condyle and reconstructed the tissue in three dimensions; a unique pattern of gene expression was found that could be only appreciated

from this perspective (Fig. 7-1E). Tissue clearing, serial 2-photon tomography, and far-red dyes (longer wavelength light is scattered less) should enable large-scale three-dimensional reconstructions of biological samples. Automated image acquisition and new image processing algorithms, when applied to large-scale three-dimensional datasets, should deepen our understanding of bone biology, repair, and bone tissue engineering.

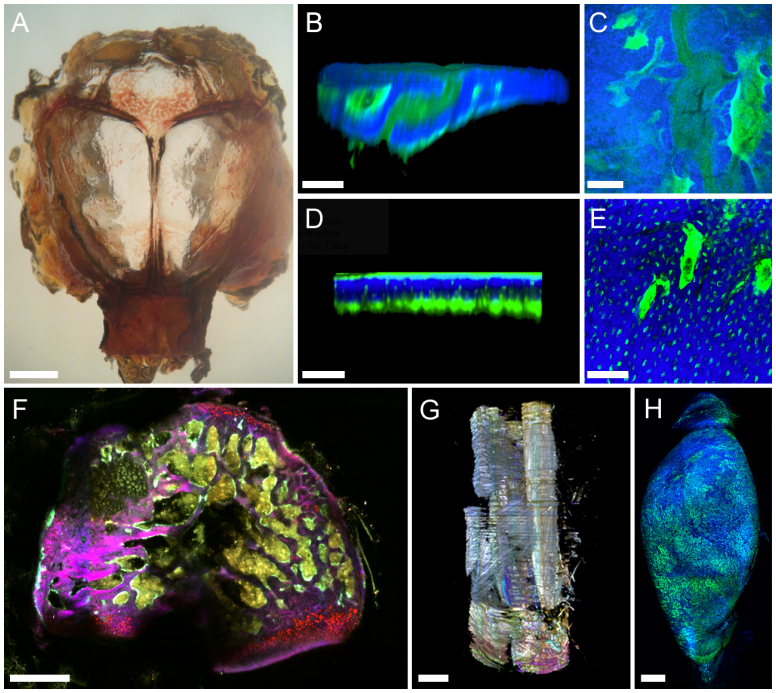


**Figure 7-1 | Extending the reach of 2-photon microscopy. (A)** Mouse calvarium cleared with BABB. Scale bar is 2 mm **(B)** Side view of 3D reconstruction of BABB cleared calvarium, viewed along the suture line. Second harmonic signal (blue) and col2.3eGFP signal (green). Scale bar is 200 µm. **(C)** Top view of (B). Scale bar is 200 µm. **(D)** Side view of 3D reconstruction of ClearT2 cleared calvarium, showing cross section of parietal lobe. Scale bar is 200 µm. **(E)** Top view of (D) showing col2.3eGFP osteocytes (green) and second harmonic (blue). Scale bar is 100 µm **(F)** Single slice of mouse long bone imaged by serial 2-photon tomography. (OC-YFP, COL1A1-CFP, COL10-mCherry, cutoff filters used: Red-(560nm)-Green-(500 nm)-Blue. Scale bar is 500 µm **(G)** Large-scale 3D reconstruction of mouse long bone picture in (F) using serial 2-photon tomography. Scale bar is 1 mm. **(H)** Top view of mouse condylar cartilage. Scale bar is 200 µm.

### 7.2.2 Optimization of scaffold permeability for bone formation *in vivo*

Scaffold permeability can be an important factor influencing bone formation *in vivo* and should be used as a quality control parameter to ensure successful outcomes. Further optimization of the fabrication process along with more sensitive permeability measurements will help to ensure scaffolds are produced consistently and with the desired physical properties. Since different bone defects may require scaffolds with a different permeability, or a permeability gradient within the bulk material, further work on control and optimization of scaffold permeability in the context of *in vivo* outcomes should prove useful. Pannella *et al.* discuss the different methods that can be used to measure permeability and calls for standardization among measurement practices. Only when the scaffold structure is optimized and a rigorous quality control process in place can additional modifications (such as growth factor addition) be confidently examined in experiments with greater statistical power (>10 animals per group).

### 7.2.3 Evaluation of long term functional properties of tissue engineered bone

The relatively short time scale of healing evaluated here (~ 3 weeks) can provide a rapid assessment of scaffold performance. Building on lessons learned in the short-term model, a long-term model evaluating the functional properties of new bone by mechanical testing is required in the future to define the quality of the regenerated bone. I have examined the performance of the Col-HA scaffolds in a long bone model of bone repair after eight weeks of implantation as a preliminary experiment in two animals (Fig. 7-2). An increase in radiopacity was observed over the eight-week implantation period, suggesting scaffold mineralization. These results suggest the Col-HA scaffolds are capable of bridging murine long bone defects, however mechanical testing is need to evaluate how well the

repaired bone is to an untreated control and/or an autologous bone. This data would provide a detailed progress report on the success of a cell-based approach compared with other methods and provide required preliminary data for the larger animal models needed before scaling up to human bone.

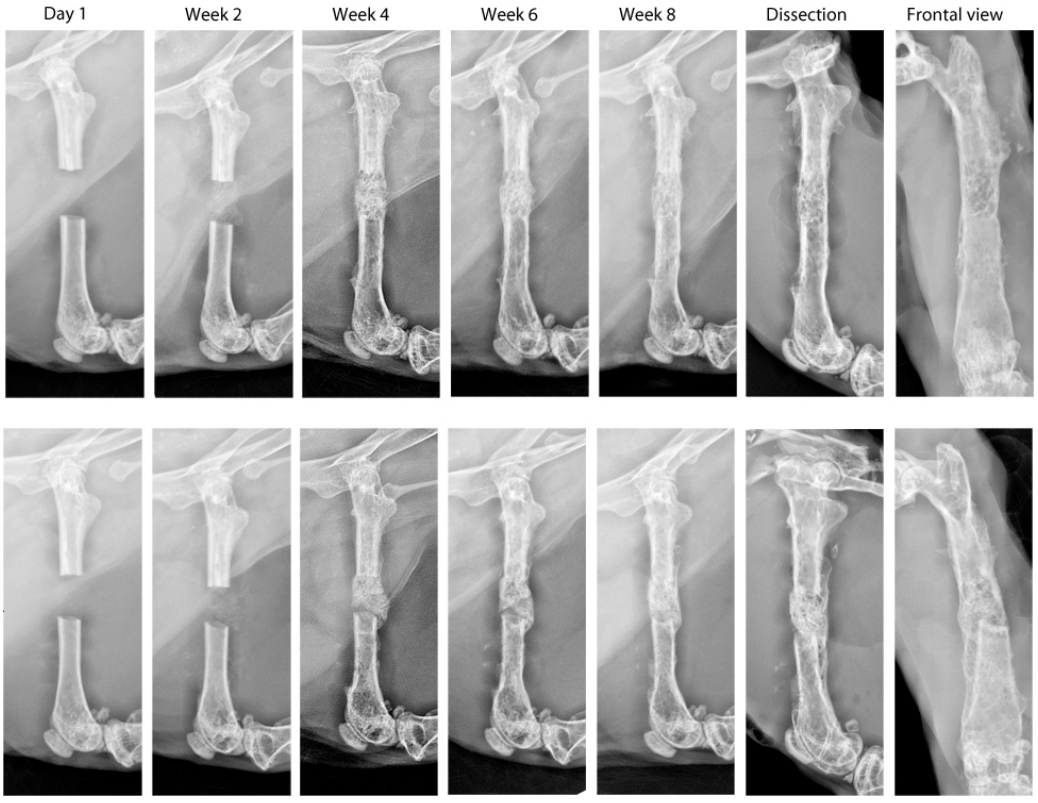


**Figure 7-2 | Radiographic progression of two long bone defects filled with collagen-HA scaffolds and culture expanded BMSCs.**

### 7.2.4 Covalent linking of growth factors to collagen-HA scaffolds using fibronectin fragments

Growth factors such as BMP-2 are potent stimulators of bone formation[69], however the supraphysiological doses required can lead to negative side effects in human patients.[77,199,200] Alternatively, growth factor dose can be reduced by delivering factors along with synergistic signaling moieties found in the ECM, such as fibronectin

fragments.[29] Furthermore, since type I collagen contains fibronectin binding sites[151], fibronectin fragments could be used to covalently link growth factors to the collagen-HA scaffold, preventing bolus release upon implantation and leveraging synergistic signaling between fibronectin and BMP-2. Fibronectin contains binding sites that strongly bind to a variety of growth factors,[185] broadening the possible candidates of factors that could be delivered. This approach could also be combined with cell-delivery to examine if this would further lower the growth factor doses required and/or enhance bone formation *in vivo* beyond cell or factor delivery alone.

## 7.3 Closing remarks

Bone tissue engineering promises to improve the quality of life of many patients suffering from bone injury or injuries that fail to heal. This dissertation has described new methods and progress towards a more complete understanding of bone tissue engineering using osteoprogenitor cells. Only with a deep understanding of the cellular and materials basis underlying the successful healing of bony defects will bone tissue engineering make clinical advances. Given the tremendous progress that has been made in the past decade by an ever-growing community of scientists, the future of bone tissue engineering seems bright.

# 8 References


1. Wolff, J. The Classic: On the Inner Architecture of Bones and its Importance for Bone Growth. *Clinical Orthopaedics and Related Research®* **468,** 1056–1065 (2010).
2. Bonewald, L. F. in *Primer on the Metabolic Bone Diseases and Disorders of Mineral Metabolism* (ed. MD, C. J. R.) 34–41 (John Wiley & Sons, Inc., 2013). at <http://onlinelibrary.wiley.com/doi/10.1002/9781118453926.ch4/summary>
3. Weiner, S. & Wagner, H. D. THE MATERIAL BONE: Structure-Mechanical Function Relations. *Annual Review of Materials Science* **28,** 271–298 (1998).
4. Taylor, D., Hazenberg, J. G. & Lee, T. C. Living with cracks: damage and repair in human bone. *Nature materials* **6,** 263–268 (2007).
5. Meyers, M. A., Chen, P.-Y., Lin, A. Y.-M. & Seki, Y. Biological materials: Structure and mechanical properties. *Progress in Materials Science* **53,** 1–206 (2008).
6. Boskey, A. L. & Robey, P. G. in *Primer on the Metabolic Bone Diseases and Disorders of Mineral Metabolism* 49–58 (John Wiley & Sons, 2013).
7. Pate, F. D. Bone Chemistry and Paleodiet. *Journal of Archaeological Method and Theory* **1,** 161–209 (1994).
8. Elliott, J. C., Mackie, P. E. & Young, R. A. Monoclinic hydroxyapatite. *Science* **180,** 1055 (1973).
9. Elliott, J. C. Monoclinic space group of hydroxyapatite. *Nature* **230,** 72 (1971).
10. KAY, M. I., YOUNG, R. A. & POSNER, A. S. Crystal Structure of Hydroxyapatite. *Nature* **204,** 1050–1052 (1964).
11. Ma, G. & Liu, X. Y. Hydroxyapatite: Hexagonal or Monoclinic? *Crystal Growth and Design* **9,** 2991–2994 (2009).
12. Shoulders, M. D. & Raines, R. T. Collagen Structure and Stability. *Annual Review of Biochemistry* **78,** 929–958 (2009).
13. Ferreira, A. M., Gentile, P., Chiono, V. & Ciardelli, G. Collagen for bone tissue regeneration. *Acta Biomater* **8,** 3191–3200 (2012).
14. Kadler, K. E., Holmes, D. F., Trotter, J. A. & Chapman, J. A. Collagen fibril formation. *Biochemical Journal* **316,** 1 (1996).
15. Eyre, D. R., Paz, M. A. & Gallop, P. M. Cross-linking in collagen and elastin. *Annual review of biochemistry* **53,** 717–748 (1984).
16. Bozec, L., van der Heijden, G. & Horton, M. Collagen Fibrils: Nanoscale Ropes. *Biophysical Journal* **92,** 70–75 (2007).
17. Orgel, J. P., Irving, T. C., Miller, A. & Wess, T. J. Microfibrillar structure of type I collagen in situ. *Proceedings of the National Academy of Sciences* **103,** 9001–9005 (2006).
18. Bella, J., Eaton, M., Brodsky, B. & Berman, H. M. Crystal and molecular structure of a collagen-like peptide at 1.9 A resolution. *Science* **266,** 75–81 (1994).
19. Frantz, C., Stewart, K. M. & Weaver, V. M. The extracellular matrix at a glance. *J Cell Sci* **123,** 4195–4200 (2010).
20. Rodgers, K. D., Sasaki, T., Aszodi, A. & Jacenko, O. Reduced perlecan in mice results in chondrodysplasia resembling Schwartz–Jampel syndrome. *Hum. Mol. Genet.* **16,** 515–528 (2007).
21. Viljoen, D. & Beighton, P. Schwartz-Jampel syndrome (chondrodystrophic myotonia). *Journal of medical genetics* **29,** 58–62 (1992).

22. Xu, T. *et al.* Targeted disruption of the biglycan gene leads to an osteoporosis-like phenotype in mice. *Nature Genetics* **20,** 78 (1998).
23. Danielson, K. G. *et al.* Targeted Disruption of Decorin Leads to Abnormal Collagen Fibril Morphology and Skin Fragility. *J Cell Biol* **136,** 729–743 (1997).
24. Anderson, H. C. *et al.* Impaired Calcification Around Matrix Vesicles of Growth Plate and Bone in Alkaline Phosphatase-Deficient Mice. *The American Journal of Pathology* **164,** 841–847 (2004).
25. Lane, T. F. & Sage, E. H. The biology of SPARC, a protein that modulates cell-matrix interactions. *FASEB J* **8,** 163–173 (1994).
26. Brekken, R. A. & Sage, E. H. SPARC, a matricellular protein: at the crossroads of cell–matrix communication: [Matrix Biology (2000) 569–580]. *Matrix Biology* **19,** 815–827 (2001).
27. Ruoslahti, E. & Pierschbacher, M. D. New perspectives in cell adhesion: RGD and integrins. *Science* **238,** 491–497 (1987).
28. Wijelath, E. S. *et al.* Heparin-II Domain of Fibronectin Is a Vascular Endothelial Growth Factor-Binding Domain Enhancement of VEGF Biological Activity by a Singular Growth Factor/Matrix Protein Synergism. *Circulation research* **99,** 853–860 (2006).
29. Martino, M. M. *et al.* Engineering the growth factor microenvironment with fibronectin domains to promote wound and bone tissue healing. *Science translational medicine* **3,** 100ra89–100ra89 (2011).
30. Vermeer, C. Gamma-carboxyglutamate-containing proteins and the vitamin K-dependent carboxylase. *Biochem. J.* **266,** 625–636 (1990).
31. Kalajzic, Z. *et al.* Directing the expression of a green fluorescent protein transgene in differentiated osteoblasts: comparison between rat type I collagen and rat osteocalcin promoters. *Bone* **31,** 654–660 (2002).
32. Ducy, P. *et al.* Increased bone formation in osteocalcin-deficient mice. (1996). at <http://deepblue.lib.umich.edu/handle/2027.42/62730>
33. Murshed, M. Extracellular matrix mineralization is regulated locally; different roles of two gla-containing proteins. *The Journal of Cell Biology* **165,** 625–630 (2004).
34. Schinke, T. *et al.* The Serum Protein α2-HS Glycoprotein/Fetuin Inhibits Apatite Formation in Vitro and in Mineralizing Calvaria Cells A POSSIBLE ROLE IN MINERALIZATION AND CALCIUM HOMEOSTASIS. *J. Biol. Chem.* **271,** 20789–20796 (1996).
35. Price, P. A., Toroian, D. & Lim, J. E. Mineralization by Inhibitor Exclusion: THE CALCIFICATION OF COLLAGEN WITH FETUIN. *Journal of Biological Chemistry* **284,** 17092–17101 (2009).
36. Karsenty, G. & Ferron, M. The contribution of bone to whole-organism physiology. *Nature* **481,** 314–320 (2012).
37. Pittenger, M. F. Multilineage Potential of Adult Human Mesenchymal Stem Cells. *Science* **284,** 143–147 (1999).
38. Shi, S. & Gronthos, S. Perivascular niche of postnatal mesenchymal stem cells in human bone marrow and dental pulp. *J. Bone Miner. Res.* **18,** 696–704 (2003).
39. Tsigkou, O. *et al.* Engineered vascularized bone grafts. *Proceedings of the National Academy of Sciences* **107,** 3311 (2010).

40. Simmons, P. J. & Torok-Storb, B. Identification of stromal cell precursors in human bone marrow by a novel monoclonal antibody, STRO-1. *Blood* **78,** 55–62 (1991).
41. Grcevic, D. *et al.* In vivo Fate Mapping Identifies Mesenchymal Progenitor Cells. *Stem Cells* **30,** 187–196 (2012).
42. Liu, Y. *et al.* Isolation of murine bone marrow derived mesenchymal stem cells using Twist2 Cre transgenic mice. *Bone* **47,** 916–925 (2010).
43. Kalajzic, I. *et al.* Use of type I collagen green fluorescent protein transgenes to identify subpopulations of cells at different stages of the osteoblast lineage. *Journal of Bone and Mineral Research* **17,** 15–25 (2002).
44. De Gorter, D. J. J. & ten Dijke, P. in *Primer on the Metabolic Bone Diseases and Disorders of Mineral Metabolism* (ed. MD, C. J. R.) 15–24 (John Wiley & Sons, Inc., 2013). at <http://onlinelibrary.wiley.com/doi/10.1002/9781118453926.ch2/summary>
45. Komori, T. *et al.* Targeted Disruption of< i> Cbfa1</i> Results in a Complete Lack of Bone Formation owing to Maturational Arrest of Osteoblasts. *Cell* **89,** 755–764 (1997).
46. Otto, F. *et al.* Cbfa1, a Candidate Gene for Cleidocranial Dysplasia Syndrome, Is Essential for Osteoblast Differentiation and Bone Development. *Cell* **89,** 765–771 (1997).
47. Burger, E. H. & Klein-Nulend, J. Mechanotransduction in bone—role of the lacuno-canalicular network. *FASEB J* **13,** S101–S112 (1999).
48. Thi, M., Suadicani, S., Schaffler, M., Weinbaum, S. & Spray, D. Polarized mechanotransduction in osteocytes: role of αVβ3 integrin on the cell processes (1180.9). *FASEB J* **28,** 1180.9 (2014).
49. Bonewald, L. F. The amazing osteocyte. *J Bone Miner Res* **26,** 229–238 (2011).
50. Wang, L. D. & Wagers, A. J. Dynamic niches in the origination and differentiation of haematopoietic stem cells. *Nature Reviews Molecular Cell Biology* **12,** 643–655 (2011).
51. Ross, F. P. & Teitelbaum, S. L. αvβ3 and macrophage colony-stimulating factor: partners in osteoclast biology. *Immunological Reviews* **208,** 88–105 (2005).
52. Teitelbaum, S. L. & Ross, F. P. Genetic regulation of osteoclast development and function. *Nat Rev Genet* **4,** 638–649 (2003).
53. Boyle, W. J., Simonet, W. S. & Lacey, D. L. Osteoclast differentiation and activation. *Nature* **423,** 337–342 (2003).
54. Baron, R. & Kneissel, M. WNT signaling in bone homeostasis and disease: from human mutations to treatments. *Nature Medicine* **19,** 179–192 (2013).
55. Zuscik, M. J. in *Primer on the Metabolic Bone Diseases and Disorders of Mineral Metabolism* (ed. MD, C. J. R.) 90–98 (John Wiley & Sons, Inc., 2013). at <http://onlinelibrary.wiley.com/doi/10.1002/9781118453926.ch11/summary>
56. Marsell, R. & Einhorn, T. A. The biology of fracture healing. *Injury* **42,** 551–555 (2011).
57. Reddi, A. & Huggins, C. B. Influence of geometry of transplanted tooth and bone on transformation of fibroblasts. *Experimental Biology and Medicine* **143,** 634 (1973).
58. Thompson, Z., Miclau, T., Hu, D. & Helms, J. A. A model for intramembranous ossification during fracture healing. *Journal of orthopaedic research* **20,** 1091–1098 (2002).

59. Cho, T. J., Gerstenfeld, L. C. & Einhorn, T. A. Differential temporal expression of members of the transforming growth factor $\\beta$ superfamily during murine fracture healing. *Journal of Bone and Mineral Research* **17,** 513–520 (2002).
60. Park, D. *et al.* Endogenous Bone Marrow MSCs Are Dynamic, Fate-Restricted Participants in Bone Maintenance and Regeneration. *Cell Stem Cell* **10,** 259–272 (2012).
61. Ushiku, C., Adams, D. J., Jiang, X., Wang, L. & Rowe, D. W. Long bone fracture repair in mice harboring GFP reporters for cells within the osteoblastic lineage. *J. Orthop. Res.* **28,** 1338–1347 (2010).
62. Quarto, R. *et al.* Repair of large bone defects with the use of autologous bone marrow stromal cells. *New England Journal of Medicine* **344,** 385–386 (2001).
63. Marcacci, M. *et al.* Stem Cells Associated with Macroporous Bioceramics for Long Bone Repair: 6- to 7-Year Outcome of a Pilot Clinical Study. *Tissue Engineering* **13,** 947–955 (2007).
64. Cowan, C. M. *et al.* Adipose-derived adult stromal cells heal critical-size mouse calvarial defects. *Nature Biotechnology* **22,** 560–567 (2004).
65. Petite, H. *et al.* Tissue-engineered bone regeneration. *Nat Biotech* **18,** 959–963 (2000).
66. Reichert, J. C. *et al.* A Tissue Engineering Solution for Segmental Defect Regeneration in Load-Bearing Long Bones. *Sci Transl Med* **4,** 141ra93–141ra93 (2012).
67. Virk, M. S. *et al.* 'Same Day' Ex-vivo Regional Gene Therapy: A Novel Strategy to Enhance Bone Repair. *Molecular Therapy* **19,** 960–968 (2011).
68. Szpalski, C., Wetterau, M., Barr, J. & Warren, S. M. Bone Tissue Engineering: Current Strategies and Techniques—Part I: Scaffolds. *Tissue Engineering Part B: Reviews* **18,** 246–257 (2012).
69. Urist, M. R. Bone: formation by autoinduction. *Science* **150,** 893 (1965).
70. Wozney, J. M. Overview of bone morphogenetic proteins. *Spine* **27,** S2–S8 (2002).
71. INFUSEBoneGraft.com. at <https://www.infusebonegraft.com/trauma_index.html>
72. BioMimetic Therapeutics | BMTI | PDGF | platelet-derived growth factor | Products | Augment Overview. at <http://www.biomimetics.com/AugmentOverview.htm>
73. Caplan, A. I. Adult mesenchymal stem cells for tissue engineering versus regenerative medicine. *Journal of Cellular Physiology* **213,** 341–347 (2007).
74. Kume, S. *et al.* Advanced Glycation End-Products Attenuate Human Mesenchymal Stem Cells and Prevent Cognate Differentiation Into Adipose Tissue, Cartilage, and Bone. *Journal of Bone and Mineral Research* **20,** 1647–1658 (2005).
75. Cheng, S. L. *et al.* In vitro and in vivo induction of bone formation using a recombinant adenoviral vector carrying the human BMP-2 gene. *Calcified tissue international* **68,** 87–94 (2001).
76. Bishop, G. B. & Einhorn, T. A. Current and future clinical applications of bone morphogenetic proteins in orthopaedic trauma surgery. *International Orthopaedics* **31,** 721–727 (2007).
77. Carragee, E. J., Hurwitz, E. L. & Weiner, B. K. A critical review of recombinant human bone morphogenetic protein-2 trials in spinal surgery: emerging safety concerns and lessons learned. *The Spine Journal* **11,** 471–491 (2011).

78. Hadjiargyrou, M. Transcriptional Profiling of Bone Regeneration. INSIGHT INTO THE MOLECULAR COMPLEXITY OF WOUND REPAIR. *Journal of Biological Chemistry* **277,** 30177–30182 (2002).
79. Grimes, R., Jepsen, K. J., Fitch, J. L., Einhorn, T. A. & Gerstenfeld, L. C. The transcriptome of fracture healing defines mechanisms of coordination of skeletal and vascular development during endochondral bone formation. *J. Bone Miner. Res.* **26,** 2597–2609 (2011).
80. Fischbach, M. A., Bluestone, J. A. & Lim, W. A. Cell-Based Therapeutics: The Next Pillar of Medicine. *Sci Transl Med* **5,** 179ps7–179ps7 (2013).
81. Bianco, P. *et al.* The meaning, the sense and the significance: translating the science of mesenchymal stem cells into medicine. *Nature Medicine* **19,** 35–42 (2013).
82. Hare JM, F. J. Comparison of allogeneic vs autologous bone marrow–derived mesenchymal stem cells delivered by transendocardial injection in patients with ischemic cardiomyopathy: The poseidon randomized trial. *JAMA* **308,** 2369–2379 (2012).
83. Szpalski, C., Barbaro, M., Sagebin, F. & Warren, S. M. Bone Tissue Engineering: Current Strategies and Techniques—Part II: Cell Types. *Tissue Engineering Part B: Reviews* **18,** 258–269 (2012).
84. Wosczyna, M. N., Biswas, A. A., Cogswell, C. A. & Goldhamer, D. J. Multipotent progenitors resident in the skeletal muscle interstitium exhibit robust BMP-dependent osteogenic activity and mediate heterotopic ossification. *Journal of Bone and Mineral Research* **27,** 1004–1017 (2012).
85. Macchiarini, P. *et al.* Clinical transplantation of a tissue-engineered airway. *The Lancet* **372,** 2023–2030 (2008).
86. Atala, A., Bauer, S. B., Soker, S., Yoo, J. J. & Retik, A. B. Tissue-engineered autologous bladders for patients needing cystoplasty. *The Lancet* **367,** 1241–1246 (2006).
87. Jungebluth, P. *et al.* Tracheobronchial transplantation with a stem-cell-seeded bioartificial nanocomposite: a proof-of-concept study. *The Lancet* (2011). doi:10.1016/S0140-6736(11)61715-7
88. Zeitouni, S. *et al.* Human Mesenchymal Stem Cell-Derived Matrices for Enhanced Osteoregeneration. *Science Translational Medicine* **4,** 132ra55–132ra55 (2012).
89. Yu, X. *et al.* Controlling the structural organization of regenerated bone by tailoring tissue engineering scaffold architecture. *Journal of Materials Chemistry* **22,** 9721 (2012).
90. Pashuck, E. T. & Stevens, M. M. Designing Regenerative Biomaterial Therapies for the Clinic. *Science Translational Medicine* **4,** 160sr4–160sr4 (2012).
91. Qu, H., Xia, Z., Knecht, D. & Wei, M. Synthesis of Dense Collagen/Apatite Composites Using a Biomimetic Method. *Journal of the American Ceramic Society* **91,** 3211–3215 (2008).
92. Yu, X. *et al.* The effect of fresh bone marrow cells on reconstruction of mouse calvarial defect combined with calvarial osteoprogenitor cells and collagen–apatite scaffold. *Journal of Tissue Engineering and Regenerative Medicine* **7,** 974–983 (2013).

93. Page-McCaw, A., Ewald, A. J. & Werb, Z. Matrix metalloproteinases and the regulation of tissue remodelling. *Nature Reviews Molecular Cell Biology* **8,** 221–233 (2007).
94. Boonrungsiman, S. *et al.* The role of intracellular calcium phosphate in osteoblast-mediated bone apatite formation. *Proceedings of the National Academy of Sciences* **109,** 14170–14175 (2012).
95. Chai, Y. C., Roberts, S. J., Schrooten, J. & Luyten, F. P. Probing the Osteoinductive Effect of Calcium Phosphate by Using an In Vitro Biomimetic Model. *Tissue Engineering Part A* **17,** 1083–1097 (2011).
96. Calve, S., Odelberg, S. J. & Simon, H. G. A transitional extracellular matrix instructs cell behavior during muscle regeneration. *Developmental biology* **344,** 259–271 (2010).
97. Lin, H., Yang, G., Tan, J. & Tuan, R. S. Influence of decellularized matrix derived from human mesenchymal stem cells on their proliferation, migration and multi-lineage differentiation potential. *Biomaterials* **33,** 4480–4489 (2012).
98. Schoof, H., Apel, J., Heschel, I. & Rau, G. Control of pore structure and size in freeze-dried collagen sponges. *Journal of Biomedical Materials Research* **58,** 352–357 (2001).
99. Waschkies, T., Oberacker, R. & Hoffmann, M. J. Control of Lamellae Spacing During Freeze Casting of Ceramics Using Double-Side Cooling as a Novel Processing Route. *Journal of the American Ceramic Society* **92,** S79–S84 (2009).
100. Holtmaat, A. *et al.* Long-term, high-resolution imaging in the mouse neocortex through a chronic cranial window. *Nat Protoc* **4,** 1128–1144 (2009).
101. Mostany, R. & Portera-Cailliau, C. Absence of Large-Scale Dendritic Plasticity of Layer 5 Pyramidal Neurons in Peri-Infarct Cortex. *The Journal of Neuroscience* **31,** 1734 (2011).
102. Khanna, K. M., McNamara, J. T. & Lefrancois, L. In Situ Imaging of the Endogenous CD8 T Cell Response to Infection. *Science* **318,** 116–120 (2007).
103. Zinselmeyer, B. H. *et al.* in *Methods in Enzymology* **461,** 349–378 (Elsevier, 2009).
104. Celli, S., Albert, M. L. & Bousso, P. Visualizing the innate and adaptive immune responses underlying allograft rejection by two-photon microscopy. *Nature Medicine* **17,** 744–749 (2011).
105. Cahalan, M. D., Parker, I., Wei, S. H. & Miller, M. J. Two-photon tissue imaging: seeing the immune system in a fresh light. *Nature reviews. Immunology* **2,** 872 (2002).
106. Lo Celso, C. *et al.* Live-animal tracking of individual haematopoietic stem/progenitor cells in their niche. *Nature* **457,** 92–96 (2009).
107. Göppert-Mayer, M. Über elementarakte mit zwei quantensprüngen. *Annalen der Physik* **401,** 273–294 (1931).
108. Masters, B. R. English translations of and translator's notes on Maria Goeppert-Mayer's theory of two-quantum processes. *Handbook of Biomedical Nonlinear Optical Microscopy* 42–84 (2008).
109. Denk, W., Strickler, J. H. & Webb, W. W. Two-photon laser scanning fluorescence microscopy. *Science* **248,** 73 (1990).
110. Zipfel, W. R., Williams, R. M. & Webb, W. W. Nonlinear magic: multiphoton microscopy in the biosciences. *Nat Biotech* **21,** 1369–1377 (2003).

111. Denk, W. & Svoboda, K. Photon upmanship: why multiphoton imaging is more than a gimmick. *Neuron* **18,** 351–357 (1997).
112. Schroeder, T. Imaging stem-cell-driven regeneration in mammals. *Nature* **453,** 345–351 (2008).
113. Williams, R. M., Zipfel, W. R. & Webb, W. W. Interpreting second-harmonic generation images of collagen I fibrils. *Biophysical journal* **88,** 1377–1386 (2005).
114. Brown, E. *et al.* Dynamic imaging of collagen and its modulation in tumors in vivo using second-harmonic generation. *Nat Med* **9,** 796–800 (2003).
115. Campagnola, P. J., Clark, H. A., Mohler, W. A., Lewis, A. & Loew, L. M. Second-harmonic imaging microscopy of living cells. *Journal of biomedical Optics* **6,** 277 (2001).
116. Chen, X., Nadiarynkh, O., Plotnikov, S. & Campagnola, P. J. Second harmonic generation microscopy for quantitative analysis of collagen fibrillar structure. *Nature Protocols* **7,** 654–669 (2012).
117. Cox, G. *et al.* 3-dimensional imaging of collagen using second harmonic generation. *Journal of structural biology* **141,** 53–62 (2003).
118. Franken, P. A., Hill, A. E., Peters, C. W. & Weinreich, G. Generation of optical harmonics. *Physical Review Letters* **7,** 118–119 (1961).
119. Fine, S. & Hansen, W. P. Optical Second Harmonic Generation in Biological Systems. *Appl. Opt.* **10,** 2350–2353 (1971).
120. Zeugolis, D. I. *et al.* Electro-spinning of pure collagen nano-fibres – Just an expensive way to make gelatin? *Biomaterials* **29,** 2293–2305 (2008).
121. Fields, G. B. The collagen triple-helix: correlation of conformation with biological activities. *Connective Tissue Research* **31,** 235–243 (1995).
122. Ott, H. C. *et al.* Regeneration and orthotopic transplantation of a bioartificial lung. *Nat Med* **16,** 927–933 (2010).
123. Vogel, G. Mending the Youngest Hearts. *Science* **333,** 1088–1089 (2011).
124. Petersen, T. H. *et al.* Tissue-Engineered Lungs for in Vivo Implantation. *Science* **329,** 538–541 (2010).
125. Griffith, L. G. Tissue Engineering--Current Challenges and Expanding Opportunities. *Science* **295,** 1009–1014 (2002).
126. Muschler, G. F., Raut, V. P., Patterson, T. E., Wenke, J. C. & Hollinger, J. O. The Design and Use of Animal Models for Translational Research in Bone Tissue Engineering and Regenerative Medicine. *Tissue Engineering Part B: Reviews* **16,** 123–145 (2010).
127. Beckman, M. Play-by-play imaging rewrites cells' rules. *Science* **300,** 76 (2003).
128. Mostany, R. & Portera-Cailliau, C. A Craniotomy Surgery Procedure for Chronic Brain Imaging. *JoVE* (2008). doi:10.3791/680
129. Mostany, R. & Portera-Cailliau, C. A method for 2-photon imaging of blood flow in the neocortex through a cranial window. *Journal of visualized experiments: JoVE* (2008). at <http://www.ncbi.nlm.nih.gov/pmc/articles/PMC2582841/>
130. Seung, H. S. Neuroscience: Towards functional connectomics. *Nature* **471,** 170–172 (2011).
131. Hickman, H. D., Bennink, J. R. & Yewdell, J. W. Caught in the Act: Intravital Multiphoton Microscopy of Host-Pathogen Interactions. *Cell Host & Microbe* **5,** 13–21 (2009).

132. Cahalan, M. D. & Parker, I. Imaging the choreography of lymphocyte trafficking and the immune response. *Current Opinion in Immunology* **18,** 476–482 (2006).
133. Li, W. *et al.* Intravital 2-photon imaging of leukocyte trafficking in beating heart. *Journal of Clinical Investigation* **122,** 2499–2508 (2012).
134. Lo Celso, C., Lin, C. P. & Scadden, D. T. In vivo imaging of transplanted hematopoietic stem and progenitor cells in mouse calvarium bone marrow. *Nat. Protocols* **6,** 1–14 (2011).
135. Williams, R. M., Zipfel, W. R. & Webb, W. W. Interpreting second-harmonic generation images of collagen I fibrils. *Biophysical journal* **88,** 1377–1386 (2005).
136. Prasad, P. N. & Williams, D. J. *Introduction to nonlinear optical effects in molecules and polymers*. (Wiley New York etc., 1991).
137. Martini, J. *et al.* Two-photon laser scanning microscopy on native cartilage and collagen-membranes for tissue-engineering. in *Proceedings of SPIE* **6089,** 60891N (2006).
138. Aghaloo, T. *et al.* The effect of NELL1 and bone morphogenetic protein-2 on calvarial bone regeneration. *Journal of Oral and Maxillofacial Surgery* **68,** 300–308 (2010).
139. Xu, X., Yang, Z., Liu, Q. & Wang, Y. In vivo Fluorescence Imaging of Muscle Cell Regeneration by Transplanted EGFP-labeled Myoblasts. *Molecular Therapy* **18,** 835–842 (2010).
140. Yin, D. *et al.* Determination of the Fate and Contribution of Ex Vivo Expanded Human Bone Marrow Stem and Progenitor Cells for Bone Formation by 2.3ColGFP. *Molecular Therapy* **17,** 1967–1978 (2009).
141. Schmid, B., Schindelin, J., Cardona, A., Longair, M. & Heisenberg, M. Software A high-level 3D visualization API for Java and ImageJ. (2010).
142. Schindelin, J. *et al.* Fiji: an open-source platform for biological-image analysis. *Nature Methods* **9,** 676–682 (2012).
143. Advanced Weka Segmentation. at <http://fiji.sc/wiki/index.php/Advanced_Weka_Segmentation>
144. Hildebrand, T. & Rüegsegger, P. A new method for the model-independent assessment of thickness in three-dimensional images. *Journal of Microscopy* **185,** 67–75 (1997).
145. Kalajzic, Z. *et al.* Use of an alpha-smooth muscle actin GFP reporter to identify an osteoprogenitor population. *Bone* **43,** 501–510 (2008).
146. Blitterswijk, C. A. van & Thomsen, P. *Tissue engineering*. (Academic Press, 2008).
147. Aaron, J. E. Periosteal Sharpey's fibers: a novel bone matrix regulatory system? *Frontiers in Endocrinology* **3,** (2012).
148. Bruder, S. P., Fink, D. J. & Caplan, A. I. Mesenchymal stem cells in bone development, bone repair, and skeletal regenaration therapy. *Journal of Cellular Biochemistry* **56,** 283–294 (1994).
149. Pilcher, B. K. *et al.* The activity of collagenase-1 is required for keratinocyte migration on a type I collagen matrix. *The Journal of cell biology* **137,** 1445–1457 (1997).

150. Tang, J., Germain, R. N. & Cui, M. Superpenetration optical microscopy by iterative multiphoton adaptive compensation technique. *PNAS* **109,** 8434–8439 (2012).
151. Di Lullo, G. A. Mapping the Ligand-binding Sites and Disease-associated Mutations on the Most Abundant Protein in the Human, Type I Collagen. *Journal of Biological Chemistry* **277,** 4223–4231 (2001).
152. Davis, G. E., Bayless, K. J., Davis, M. J. & Meininger, G. A. Regulation of tissue injury responses by the exposure of matricryptic sites within extracellular matrix molecules. *The American journal of pathology* **156,** 1489–1498 (2000).
153. Hernigou, P. H., Poignard, A., Beaujean, F. & Rouard, H. Percutaneous autologous bone-marrow grafting for nonunions | Influence of the number and concentration of progenitor cells. *The Journal of Bone & Joint Surgery* **87,** 1430–1437 (2005).
154. Rajan, N., Habermehl, J., Coté, M.-F., Doillon, C. J. & Mantovani, D. Preparation of ready-to-use, storable and reconstituted type I collagen from rat tail tendon for tissue engineering applications. *Nat Protoc* **1,** 2753–2758 (2007).
155. Metscher, B. D. MicroCT for developmental biology: A versatile tool for high-contrast 3D imaging at histological resolutions. *Developmental Dynamics* **238,** 632–640 (2009).
156. Doube, M. *et al.* BoneJ: Free and extensible bone image analysis in ImageJ. *Bone* (2010).
157. Bolte, S. & Cordelieres, F. P. A guided tour into subcellular colocalization analysis in light microscopy. *Journal of microscopy* **224,** 213–232 (2006).
158. O'Brien, F. J., Harley, B. A., Yannas, I. V. & Gibson, L. Influence of freezing rate on pore structure in freeze-dried collagen-GAG scaffolds. *Biomaterials* **25,** 1077–1086 (2004).
159. Kemppainen, J. M. & Hollister, S. J. Differential effects of designed scaffold permeability on chondrogenesis by chondrocytes and bone marrow stromal cells. *Biomaterials* **31,** 279–287 (2010).
160. Rehman, I. & Bonfield, W. Characterization of hydroxyapatite and carbonated apatite by photo acoustic FTIR spectroscopy. *Journal of Materials Science: Materials in Medicine* **8,** 1–4 (1997).
161. Chang, M. C. & Tanaka, J. FT-IR study for hydroxyapatite/collagen nanocomposite cross-linked by glutaraldehyde. *Biomaterials* **23,** 4811–4818 (2002).
162. Villa, M. M., Wang, L., Huang, J., Rowe, D. W. & Wei, M. Visualizing Osteogenesis In Vivo Within a Cell–Scaffold Construct for Bone Tissue Engineering Using Two-Photon Microscopy. *Tissue Engineering Part C: Methods* **19,** 839–849 (2013).
163. Holy, C. E., Cheng, C., Davies, J. E. & Shoichet, M. S. Optimizing the sterilization of PLGA scaffolds for use in tissue engineering. *Biomaterials* **22,** 25–31 (2001).
164. Krebsbach, P. H., Mankani, M. H., Satomura, K., Kuznetsov, S. A. & Robey, P. G. Repair of craniotomy defects using bone marrow stromal cells. *Transplantation* **66,** 1272–1278 (1998).
165. Bruder, S. P., Kraus, K. H., Goldberg, V. M. & Kadiyala, S. The Effect of Implants Loaded with Autologous Mesenchymal Stem Cells on the Healing of

Canine Segmental Bone Defects. *The Journal of Bone & Joint Surgery* **80,** 985–96 (1998).
166. Davis, G. E. Affinity of integrins for damaged extracellular matrix: α<sub>v β<sub>3 binds to denatured collagen type I through RGD sites. *Biochemical and biophysical research communications* **182,** 1025–1031 (1992).
167. Parks, W. C. Matrix metalloproteinases in repair. *Wound Repair and Regeneration* **7,** 423–432 (1999).
168. Werb, Z. & Gordon, Sa. Secretion of a specific collagenase by stimulated macrophages. *The Journal of experimental medicine* **142,** 346–360 (1975).
169. Van Amerongen, M. J., Harmsen, M. C., Petersen, A. H., Kors, G. & van Luyn, M. J. A. The enzymatic degradation of scaffolds and their replacement by vascularized extracellular matrix in the murine myocardium. *Biomaterials* **27,** 2247–2257 (2006).
170. English, K. & Wood, K. J. Mesenchymal Stromal Cells in Transplantation Rejection and Tolerance. *Cold Spring Harb Perspect Med* **3,** (2013).
171. Auletta, J. J., Deans, R. J. & Bartholomew, A. M. Emerging roles for multipotent, bone marrow–derived stromal cells in host defense. *Blood* **119,** 1801–1809 (2012).
172. Bruder, S. P. *et al.* Bone regeneration by implantation of purified, culture-expanded human mesenchymal stem cells. *Journal of Orthopaedic Research* **16,** 155–162 (1998).
173. Impens, S., Chen, Y., Mullens, S., Luyten, F. & Schrooten, J. Controlled Cell-Seeding Methodologies: A First Step Toward Clinically Relevant Bone Tissue Engineering Strategies. *Tissue Engineering Part C: Methods* **16,** 1575–1583 (2010).
174. Wiedmann-Al-Ahmad, M., Gutwald, R., Lauer, G., Hübner, U. & Schmelzeisen, R. How to optimize seeding and culturing of human osteoblast-like cells on various biomaterials. *Biomaterials* **23,** 3319–3328 (2002).
175. Papadimitropoulos, A. *et al.* A collagen network phase improves cell seeding of open-pore structure scaffolds under perfusion. *Journal of Tissue Engineering and Regenerative Medicine* (2011). at <http://onlinelibrary.wiley.com/doi/10.1002/term.506/full>
176. Grayson, W. L. *et al.* Effects of Initial Seeding Density and Fluid Perfusion Rate on Formation of Tissue-Engineered Bone. *Tissue Engineering Part A* **14,** 1809–1820 (2008).
177. Grayson, W. L. *et al.* Engineering anatomically shaped human bone grafts. *Proceedings of the National Academy of Sciences* **107,** 3299 (2010).
178. Grayson, W. L. *et al.* Optimizing the medium perfusion rate in bone tissue engineering bioreactors. *Biotechnology and Bioengineering* **108,** 1159–1170 (2011).
179. Sikavitsas, V. I., Dolder, J., Bancroft, G. N., Jansen, J. A. & Mikos, A. G. Influence of the in vitro culture period on the in vivo performance of cell/titanium bone tissue-engineered constructs using a rat cranial critical size defect model. *Journal of Biomedical Materials Research Part A* **67,** 944–951 (2003).
180. Kuhn, L. T. *et al.* Developmental-Like Bone Regeneration by Human Embryonic Stem Cell-Derived Mesenchymal Cells. *Tissue Engineering Part A* **20,** 365–377 (2014).
181. Harburger, D. S. & Calderwood, D. A. Integrin signalling at a glance. *Journal of Cell Science* **122,** 1472–1472 (2009).

182. Villa, M. M., Wang, L., Huang, J., Rowe, D. W. & Wei, M. Bone tissue engineering with a collagen–hydroxyapatite scaffold and culture expanded bone marrow stromal cells. *J. Biomed. Mater. Res.* n/a–n/a (2014). doi:10.1002/jbm.b.33225
183. Hynes, R. O. The extracellular matrix: not just pretty fibrils. *Science* **326,** 1216–1219 (2009).
184. Martino, M. M., Briquez, P. S., Ranga, A., Lutolf, M. P. & Hubbell, J. A. Heparin-binding domain of fibrin(ogen) binds growth factors and promotes tissue repair when incorporated within a synthetic matrix. *Proceedings of the National Academy of Sciences* **110,** 4563–4568 (2013).
185. Martino, M. M. & Hubbell, J. A. The 12th–14th type III repeats of fibronectin function as a highly promiscuous growth factor-binding domain. *The FASEB Journal* **24,** 4711–4721 (2010).
186. Datta, N., Holtorf, H. L., Sikavitsas, V. I., Jansen, J. A. & Mikos, A. G. Effect of bone extracellular matrix synthesized in vitro on the osteoblastic differentiation of marrow stromal cells. *Biomaterials* **26,** 971–977 (2005).
187. Hughes, C. S., Postovit, L. M. & Lajoie, G. A. Matrigel: A complex protein mixture required for optimal growth of cell culture. *PROTEOMICS* **10,** 1886–1890 (2010).
188. Qu, H. & Wei, M. The effect of temperature and initial pH on biomimetic apatite coating. *J. Biomed. Mater. Res.* **87B,** 204–212 (2008).
189. Strecker, S., Fu, Y., Liu, Y. & Maye, P. Generation and characterization of Osterix-Cherry reporter mice. *Genesis* **51,** 246–258 (2013).
190. Madisen, L. *et al.* A robust and high-throughput Cre reporting and characterization system for the whole mouse brain. *Nat Neurosci* **13,** 133–140 (2010).
191. Friedenstein, A. J., Chailakhyan, R. K., Latsinik, N. V., Panasyuk, A. F. & Keiliss-Borok, I. V. Stromal cells responsible for transferring the microenvironment of the hemopoietic tissues. Cloning in vitro and retransplantation in vivo. *Transplantation* **17,** 331–340 (1974).
192. Dominici, M. *et al.* Minimal criteria for defining multipotent mesenchymal stromal cells. The International Society for Cellular Therapy position statement. *Cytotherapy* **8,** 315–317 (2006).
193. Muguruma, Y. Reconstitution of the functional human hematopoietic microenvironment derived from human mesenchymal stem cells in the murine bone marrow compartment. *Blood* **107,** 1878–1887 (2006).
194. Zaman, M. H. *et al.* Migration of tumor cells in 3D matrices is governed by matrix stiffness along with cell-matrix adhesion and proteolysis. *PNAS* **103,** 10889–10894 (2006).
195. Ramanujan, S. *et al.* Diffusion and Convection in Collagen Gels: Implications for Transport in the Tumor Interstitium. *Biophysical Journal* **83,** 1650–1660 (2002).
196. Mitsak, A. G., Kemppainen, J. M., Harris, M. T. & Hollister, S. J. Effect of Polycaprolactone Scaffold Permeability on Bone Regeneration *In Vivo*. *Tissue Engineering Part A* **17,** 1831–1839 (2011).
197. Kadiyala, S., Jaiswal, N. & Bruder, S. P. Culture-expanded, bone marrow-derived mesenchymal stem cells can regenerate a critical-sized segmental bone defect. *Tissue engineering* **3,** 173–185 (1997).

198. Lutolf, M. P. *et al.* Repair of bone defects using synthetic mimetics of collagenous extracellular matrices. *Nature Biotechnology* **21,** 513–518 (2003).
199. Wong, D. A., Kumar, A., Jatana, S., Ghiselli, G. & Wong, K. Neurologic impairment from ectopic bone in the lumbar canal: a potential complication of off-label PLIF/TLIF use of bone morphogenetic protein-2 (BMP-2). *Spine J* **8,** 1011–1018 (2008).
200. Robin, B. N. *et al.* Cytokine-mediated inflammatory reaction following posterior cervical decompression and fusion associated with recombinant human bone morphogenetic protein-2: a case study. *Spine* **35,** E1350–1354 (2010).
201. Home | HEALOS® for Dental. at <http://www.healosfordental.com/>
202. Collagraft. at <http://catalog.zimmer.com/content/zpc/products/300/315/320.html>
203. Schwarz, K. & Epple, M. Hierarchically structured polyglycolide – a biomaterial mimicking natural bone. *Macromol. Rapid Commun.* **19,** 613–617 (1998).
204. Haly, A. R. & Snaith, J. W. Calorimetry of rat tail tendon collagen before and after denaturation: the heat of fusion of its absorbed water. *Biopolymers* **10,** 1681–1699 (1971).
205. Han, L.-H., Lai, J. H., Yu, S. & Yang, F. Dynamic tissue engineering scaffolds with stimuli-responsive macroporosity formation. *Biomaterials* **34,** 4251–4258 (2013).
206. Dias, M. R., Fernandes, P. R., Guedes, J. M. & Hollister, S. J. Permeability analysis of scaffolds for bone tissue engineering. *Journal of Biomechanics* **45,** 938–944 (2012).
207. Kalajzic, I. *et al.* Use of type I collagen green fluorescent protein transgenes to identify subpopulations of cells at different stages of the osteoblast lineage. *Journal of Bone and Mineral Research* **17,** 15–25 (2002).
208. R Core Team. *R: A language and environment for statistical computing*. (R Foundation for Statistical Computing, 2013). at <http://www.R-project.org/>
209. O'Brien, F. J. *et al.* The effect of pore size on permeability and cell attachment in collagen scaffolds for tissue engineering. *Technology and Health Care* **15,** 3–17 (2007).
210. Grimm, M. J. & Williams, J. L. Measurements of permeability in human calcaneal trabecular bone. *Journal of biomechanics* **30,** 743–745 (1997).
211. Pennella, F. *et al.* A Survey of Methods for the Evaluation of Tissue Engineering Scaffold Permeability. *Annals of Biomedical Engineering* **41,** 2027–2041 (2013).
212. Parra, S. G., Chia, T. H., Zinter, J. P. & Levene, M. J. Multiphoton microscopy of cleared mouse organs. *Journal of Biomedical Optics* **15,** 036017 (2010).
213. Ragan, T. *et al.* Serial two-photon tomography for automated ex vivo mouse brain imaging. *Nature Methods* **9,** 255–258 (2012).
214. Kuwajima, T. *et al.* ClearT: a detergent- and solvent-free clearing method for neuronal and non-neuronal tissue. *Development* **140,** 1364–1368 (2013).

# 9 List of Published Articles

1. Villa, M.M., Wang, L., Huang, J.P., Rowe, D.W., Wei, M., Visualizing Osteogenesis In Vivo within a Cell-Scaffold Construct for Bone Tissue Engineering using 2-Photon Microscopy, *Tissue Engineering: Part C* **19**, 821-899 (2013).
2. Xia, Z., Villa, M.M., Wei, M., A biomimetic collagen–apatite scaffold with a multi-level lamellar structure for bone tissue engineering. *Journal of Materials Chemistry B* **2** (14), 1998-2007 (2014).
3. Villa, M.M., Wang, L., Huang, J.P., Rowe, D.W., Wei, M., Bone tissue engineering with a collagen-hydroxyapatite scaffold and culture expanded bone marrow stromal cells. *Journal of Biomedical Materials Research Part B: Applied Biomaterials* (2014)
4. Villa, M.M., Wang, L., Rowe, D.W., Wei, M., The effect of a cell-attachment period and an extracellular matrix cell carrier on bone tissue engineering *in vivo* with collagen-hydroxyapatite scaffolds, *submitted*
5. Villa, M.M., Wang, L., Rowe, D.W., Wei, M., Improving the permeability of lyophilized collagen-hydroxyapatite scaffolds with gelatin microspheres, *in prep.*

# 10 List of Presented Abstracts

1. Villa, M.M., Huang, J.P., Wang, L., Rowe, D.W., and Wei, M., Healing Murine Calvarial Defects with Bone Marrow Stromal Cells and Collagen-Hydroxyapatite Scaffolds, Biomaterials & Tissue Engineering Gordon Research Conference, Holderness, NH, USA, 2013.
2. Villa, M.M., Wang, L., Rowe, D.W., and Wei, M., 2-Photon Microscopy for Live Animal Imaging of Bone Regeneration, The XIIth Congress of the International Society of Bone Morphometry, Minneapolis, MN, USA, Oral presentation, 2012.
3. Villa, M.M., Wang, L., Rowe, D.W., and Wei, M., 4D Live-animal microscopy for bone regeneration studies using a mouse calvarial model, World Biomaterials Congress, Chengdu, China, Oral presentation, 2012.
4. Villa, M.M., and Wei, M., Unidirectional freeze casting of collagen-hydroxyapatite scaffolds for bone regeneration, Materials Research Society Fall Meeting, 2011 Best student poster award.

# 11 List of Figures

# 12 List of Tables

# 13 List of Abbreviations

| | |
|---|---|
| AF | Area fraction |
| AP | Alkaline phosphatase |
| BABB | Benzyl alcohol and benzyl benzoate |
| BME | Basement membrane extract |
| BMP-2 | Bone morphogenetic protein-2 |
| BMSCs | Bone marrow stromal cells |
| CFP | Cyan fluorescent protein |
| Col2.3 | 2.3 kB portion of COL1A1 promoter region |
| Col3.6 | 3.6 kB portion of COL1A1 promoter region |
| CSE | Cell seeding efficiency |
| DIC | Differential interference contrast |
| EDC | [1-ethyl-3-(3-dimethylaminopropyl) carbodiimide hydrochloride] |
| EDM | Euclidean distance map |
| EDTA | Ethylenediaminetetraacetic acid |
| EMD | Emerald fluorescent protein |
| FESEM | Field emission scanning electron microscope |
| FIJI | Fiji is just ImageJ |
| FT-IR | Fourier transform infrared spectroscopy |
| GAG | Glycosaminoglycan |
| GFP | Green fluorescent protein |
| HA | Hydroxyapatite |
| HESC | Human embryonic stem cell |
| HSC | Hematopoietic stem cell |
| IPSC | Induced pluripotent stem cell |
| MAR | Mineral apposition rate |
| MEM | Minimum essential media |
| MGP | Matrix gla protein |
| MMP-1 | Matrix metalloproteinase-1/Collagenase |
| MSC | Mesencyhmal stem cell |
| NCP | Non-collagenous protein |
| NSG | Nod scid gamma |
| PBS | Phosphate buffered saline |
| RBC | Red blood cell |
| ROI | Region of interest |
| SLRPs | Small leucine-rich proteoglycans |
| SMAA | Smooth muscle alpha actin, gene |
| WEKA | Waikato Environment for Knowledge Analysis |
| XRD | X-ray diffraction |
| YFP | Yellow fluorescent protein |